Supplementary data/materials for the article:

"Alkali-silica reaction products and cracks: X-ray micro-tomography-based analysis of their spatial-temporal evolution at a mesoscale"

by

Mahdieh Shakoorioskooie[a,b,c,♦], Michele Griffa[a,♦], Andreas Leemann[a], Robert Zboray[b], Pietro Lura[a,c]

[a] *Concrete and Asphalt Laboratory, Empa, Swiss Federal Laboratories for Materials Science and Technology, CH-8600 Dübendorf, Switzerland*

[b] *Center for X-ray Analytics, Empa, Swiss Federal Laboratories for Materials Science and Technology, CH-8600 Dübendorf, Switzerland*

[c] *Institute for Building Materials (IfB), ETH Zürich, CH-8093 Zürich, Switzerland*

S1. Materials characterizations

S1.1 ASR-reactive aggregates: chemical and mineralogical characterizations

Table T 1 provides the chemical composition of both the U and the P aggregates, as obtained by X-ray fluorescence (XRF) analysis, which was performed on sintered powder according to the standard DIN EN 196-2 [1]. The aggregate powder was obtained by grinding one kg of aggregates in the sieve size range 0 – 4 mm with a planetary ball-milling machine.The size range < 63 µm was used for analysis.

Table T 1 shows that silica (SiO_2) is the predominant chemical species of both types of aggregates. The other minerals had similar content in both types of aggregates.

♦ Corresponding authors.
E-Mail addresses: mahdieh.shakoorioskooie@empa.ch; michele.griffa@empa.ch

Table T 1: Chemical composition obtained by X-ray fluorescence (XRF) analysis performed according to the DIN EN 196-2:2013 standard. ♥ LOI: Loss on Ignition. † TC: Total Carbon content, measured according to the ISO 10694 standard [2]. *‡ TOC: Total Organic Carbon content. ♠ TIC: Total Inorganic Carbon content, obtained as the difference between the TC and TOC values. ♦ CO_2: total CO_2 content obtained from the TC value.*

Chemical species	**Uri ("U")**	**Praz ("P")**
	Content (mass-%)	Content (mass-%)
SiO_2	64.3	67.98
Al_2O_3	8.79	7.16
CaO	8.66	8.86
Fe_2O_3	2.02	1.38
MgO	2.06	1.91
K_2O	2.1	2.17
TiO_2	0.346	0.201
Cr_2O_3	0.006	0.005
MnO	0.048	0.03
P_2O_5	0.079	0.064
Na_2O	1.65	1.37
SO_3	0.39	0.09
LOI♥	9.45	8.68
Total	**99.89**	**99.9**
TC†	2.14	2.15
TOC‡	0.18	0.05
TIC♠	1.96	2.1
CO_2♦	7.18	7.7

Mineralogical information about each aggregate type was obtained by powder X-ray diffraction (PXRD) analysis, which was performed by using Cu-Kα X-rays and a Bragg-Brentano geometrical configuration. The scattering angle (2θ) range covered by the X-ray detector was $[7°; 70°]$. The measurement was performed with a Malvern Panalytical X'Pert Pro MPD diffractometer. The analysis of the PXRD pattern indicated that both the P and the U aggregates consist of about 50 mass-% quartz. The feldspars (with Na content > K content) in these aggregates differs slightly, 25 mass-% in U and 16 mass-% in P. Carbonates (with more calcite than dolomite) are about 14 mass-% in U and 20 mass-% in P aggregates. The remaining mineral phases are layer silicates such as clinochlore, muscovite and biotite. Nevertheless, the differences in the mineralogical compositions are almost negligible.

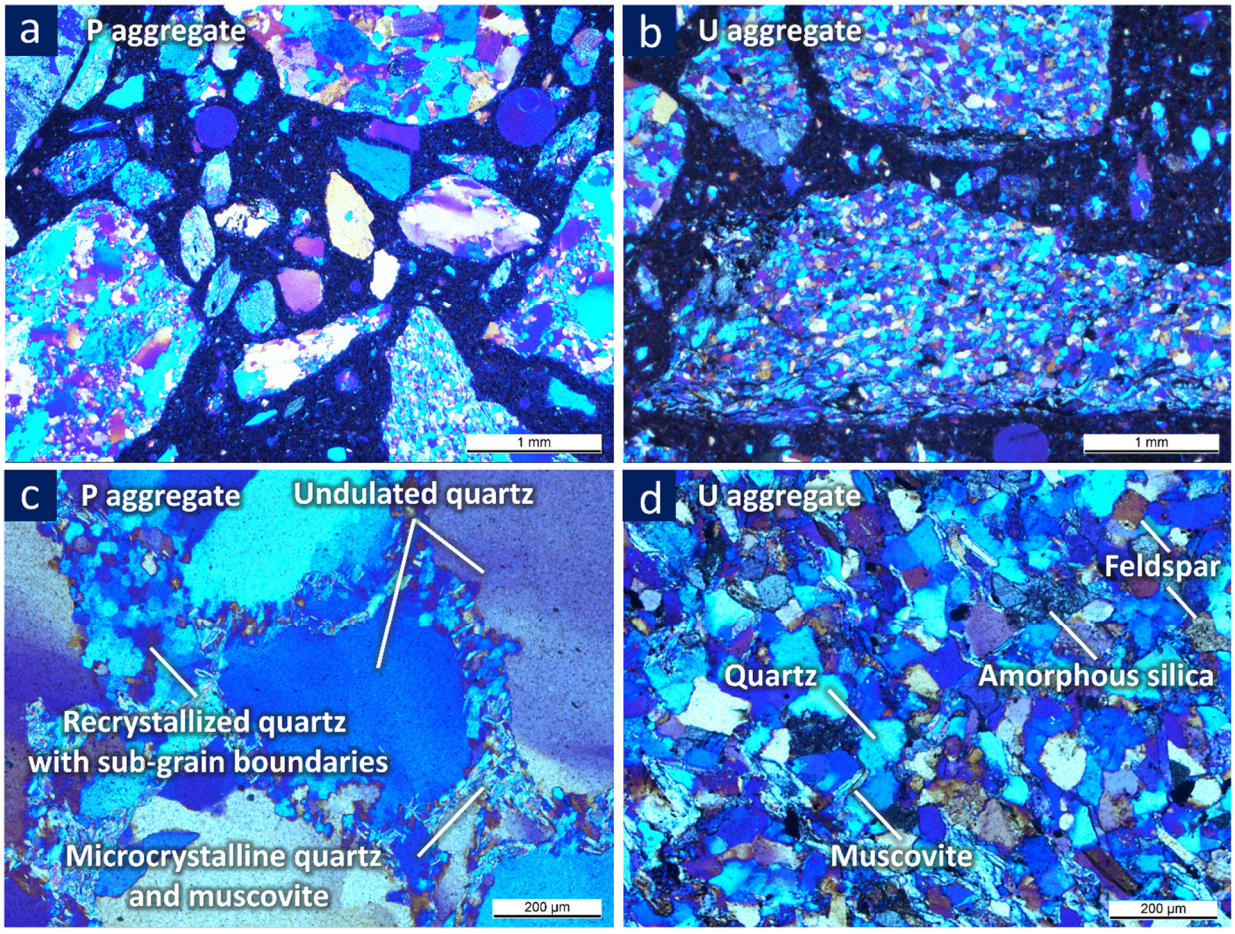

Figure S 1. Examples of mineral textures of both aggregate types, characterized by optical microscopy performed with cross-polarized light (CP-OM): (a) and (c) thin-section image from the concrete containing P aggregates at lower and higher magnifications, respectively; (b) and (d) the same for U aggregates.

Regardless of relatively similar compositions, there are major differences between the distributions of the minerals (texture) of the two aggregates (Figure S 1). The P aggregates (Figure S 1 (a) and (c)) are characterized by elongated, highly undulated quartz grains presumably created by tectonic processes [3]. They are metamorphic rocks (granitic) of alluvial origin, mainly consisting of gneiss and quartzite. A bimodal grain size distribution was observed, consisting of a fine grained matrix of micro-crystalline quartz and muscovite and coarse, highly undulated quartz grains (Figure S 1 (c)). The matrix consisted of a mixture of mica and micro-crystallized quartz. The U aggregates, on the other hand, were identified as sedimentary aggregates consisting of several equi-sized quartz grains (Figure S 1 (b)).

Reactive aggregates are usually categorized in two main groups: the first one consists of stressed crystalline minerals (e.g., quartz), characterized by a rather slow reactivity and the second group involves amorphous minerals, characterized by relatively fast ASR [4]. The P aggregates can be considered as slow-reacting aggregates, while the U aggregates, as sedimentary rocks, can be regarded as fast-reacting aggregates [4].

S1.2 ASR products: chemical and morphological characterizations by SEM-EDX analysis

A FEI Quanta 650 environmental scanning electron microscope, by Thermo Fisher Scientific, equipped with an EDX detector (Thermo Noran Ultra Dry 60 mm^2) and the Pathfinder X-Ray Microanalysis software (also by Thermo Fisher Scientific), all available at Empa's Electron Microscopy Center (https://www.empa.ch/web/s299/info), were used for SEM and EDX analysis. The electron beam acceleration voltage for both the SEM and the EDX measurements was set to 20 kV.

Figure S 2 (a) to (d) shows the EDX analysis results in the form of ternary diagrams. There, Na_2O_{eq} indicates the sum of atomic percentages of existing alkalis in each system. For the reference specimens, the alkali are only Na and K alkalis, while Cs is included in the doped specimens. Each point in such ternary diagrams refers to a small region occupied by ASR products, either crystalline regions located well inside the aggregate volume or amorphous regions at the aggregate boundaries or inside cracks through the cement paste.

In all ternary diagrams the composition of the ASR products was almost identical regardless of the Cs addition and of the aggregate type. This result indicates that Cs replaced part of other alkalis in the products. The only subtle difference between the diagrams is a slight shift towards higher silica in the Cs-doped specimens. This could be related to the higher rate of SiO_2 dissolution in presence of Cs^+ ions, already reported in [5].

Figure S 3 (a) shows the products' composition, in terms of alkali-to-silicon molar ratio and calcium-to-silicon molar ratio, at different time points during the ASR acceleration and for Cs-doped specimens. At any time, each molar ratio spanned approximately the same respective range. Such range was similar to what already reported in the literature [5]. No significant difference in such molar ratios was observed when comparing products formed in specimens with or without Cs-doping (Figure S 3 (b)). Finally, in the presence of Cs-doping, the contribution of the Cs^+ ions to the ASR products remained almost the same at different ages (Figure S 3 (c)).

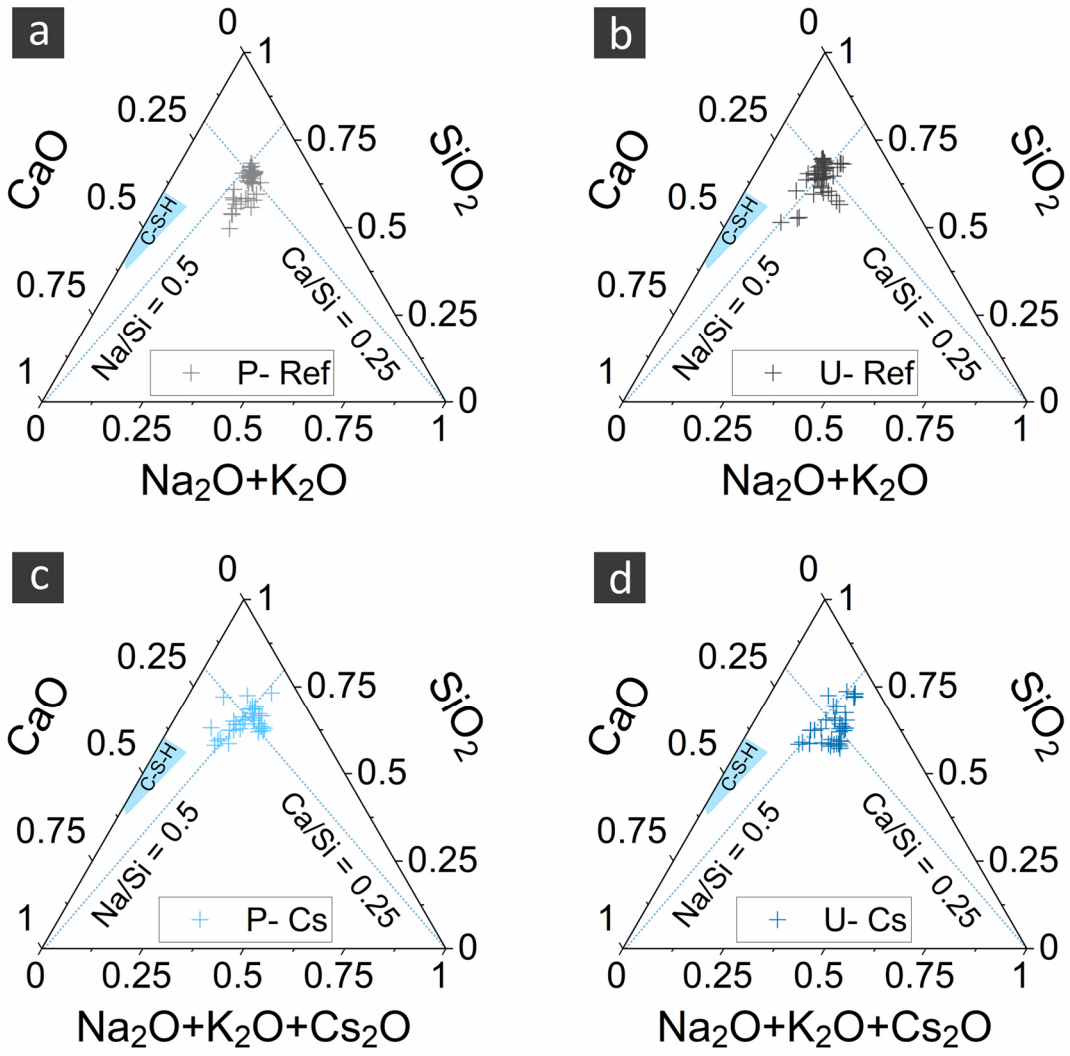

Figure S 2. energy-dispersive X-ray spectroscopy (EDX) analysis results presented in the form of ternary diagrams for the composition of ASR products at more than forty points from both crystalline (inside of the aggregates) and amorphous (boundary regions of aggregates and in the cement paste) products for the (a) P-Ref, (b) U-Ref, (c) P-Cs and (d) U-Cs specimens, respectively.

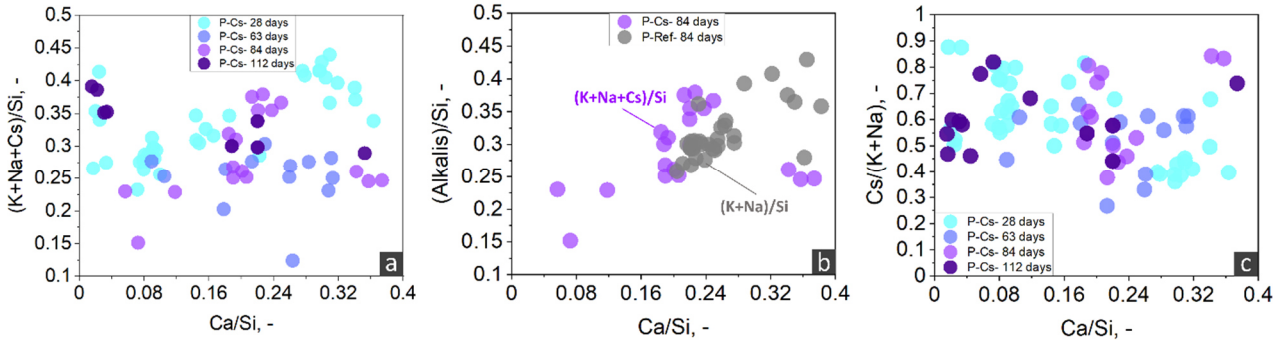

Figure S 3. Evolution of the chemical composition of ASR products formed in the specimens with and without Cs-doping: Example of EDX analysis results. (a) Evolution of the composition of the products in P-Cs specimens, in terms of alkali-to-silicon molar ratio and calcium-to-silicon molar ratio. (b) Corresponding data as in (a) but at one time point only (84 days) and comparing ASR products formed in P-Cs and P-Ref specimens. (c) Evolution of the molar ratio of Cs^+ to the other alkali ions in the ASR products found in P-Cs specimens. In each scatter plot, each point refers to a location inside a products region.

The SEM-BSE micrographs for distinct specimens at distinct time points, both without and with Cs-doping, exemplifies the advantages brought by the Cs-doping. In its absence, ASR products inside cracks could be recognized mainly based upon some characteristic morphological features, namely a plate-like texture. The BSE contrast between products and the aggregates or cement paste material phases is too small for an easy and always unequivocal detection of the products. See Figure S 4 and Figure S 5.

On the contrary, in the presence of Cs-doping, BSE contrast suffices for unequivocally detecting products and opens up the possibility to observe characteristic spatial-temporal distribution patterns, e.g., the prevalence of products in regions close to the aggregate boundaries, at earlier ages, followed by their appearance closer to the center of the aggregates only at later ages (see Figure S 5).

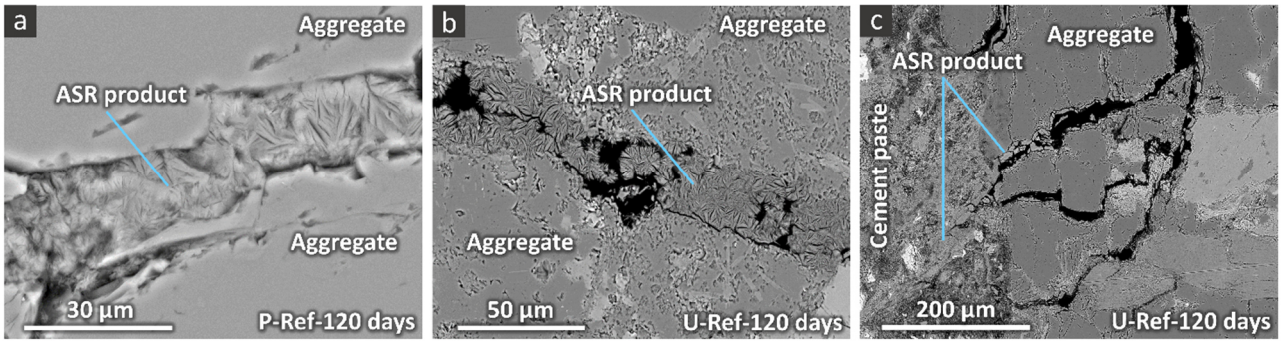

Figure S 4. Examples of SEM-BSE micrographs from reference specimens showing the formation of ASR products inside aggregates and cement paste: (a) P-Ref and (b) U-Ref specimens, products

within aggregates; (c) a wider view showcasing ASR damage in a U-Ref specimen, both inside aggregates and through the cement paste.

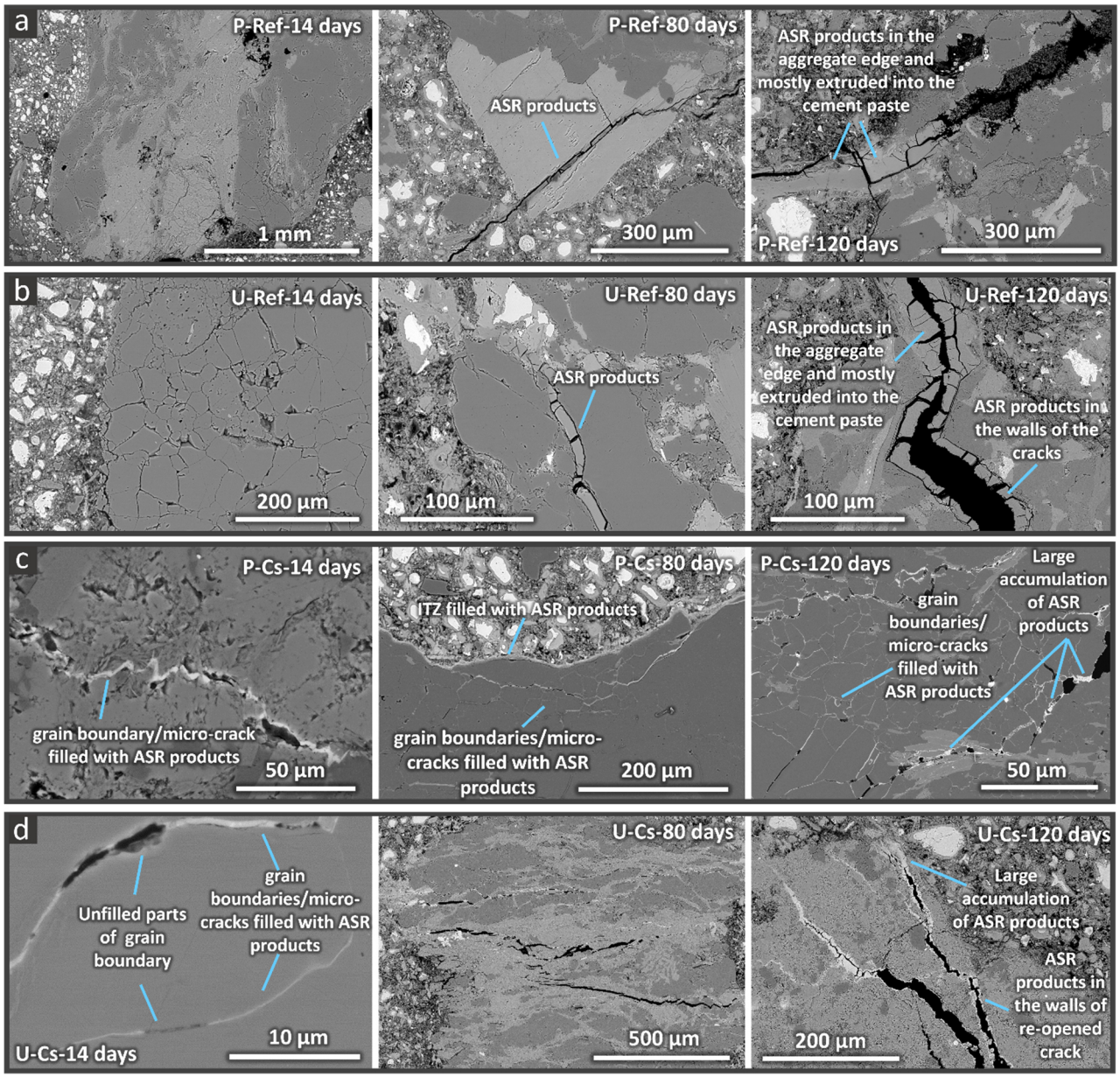

Figure S 5. SEM-BSE micrographs providing examples of the distribution of ASR products and cracks in the specimens with and without Cs, cast with P and U aggregates. For every specimen type, the micrographs were acquired at 14, 80 and 120 days. Each column refers to a distinct specimen type. SEM-BSE micrographs for (a) P-Ref, (b) U-Ref, (c) P-Cs and (d) U-Cs specimens, respectively.

S2. Time-lapse X-ray micro-tomography (XMT)

S2.1 Experimental settings

XMT was performed using an EasyTomo XL-Ultra tomograph (RX Solutions, Chavanod, France). Such tomograph consists of a micro-focus, direct transmission X-ray source and a flat panel X-ray detector. the used X-ray source was a Hamamatsu L10801, which is a reflection-based source. The emitted X-ray beam geometry is a cone one, with a 30° opening angle. The X-ray detector (by Varian) consists of a 2D array of amorphous Si pixels (1920 × 1536), each with physical size p = 127 μm, covered with a thin layer of CsI (scintillator for the X-ray photons). The X-ray source voltage and current were set to 90 kV and 150 μA, respectively. Thus, the corresponding X-ray photon energy range covered up to 90 keV. In such range, Compton scattering and photoelectric absorption are the two most probable physical processes of interaction between X-ray photons and atoms. That implies that the tomogram's voxel value is a proxy variable of the X-ray attenuation coefficient μ (units of length^{-1}). μ is proportional to (1) a power of the local, effective atomic number Z_{eff} and to (2) the local mass density ρ. Thus, within the mentioned X-ray photon energy, larger voxel values are associated with denser portions of the specimen.

The specimen-to-source distance (d_{Ss}) was 113.63 mm and the source-to-detector distance (d_{Sd}) was 410.16 mm. The geometrical magnification achieved in the 2D raw projections (so-called “radio-graphs”) thus was $M = {}^{d_{Sd}}/_{d_{Ss}} = 3.6$. The resulting effective voxel size for the final tomograms was $\tilde{p} = {}^{p}/_{M} \cong 35$ μm. It should be noted that this is not the actual spatial resolution of the tomograms, as 3D images. Their actual (effective) spatial resolution is of the order of double the values of $\tilde{p}$ (upper bound), because of convolutions of multiple point spread functions of different components of the image formation process, e.g., blurring by the X-ray source finite size.

XMT was conducted only for the middle region along the longitudinal (Z) direction of each specimen (see Figure S 16 (e) below), covering a volume of interest (VOI) of 40×40×45 mm^3 (original specimen size = 40×40×160 mm^3). The rotation axis of the specimen stage was approximately parallel to the specimens' longitudinal direction. For each tomography, 3600 radiographs were acquired over 360° of specimen rotation. Each acquired radiograph was the results of pixel-wise averaging of 10 radio-graphs at the same rotation angle. Each single radiograph for the averaging was obtained by exposing the X-ray detector for 227 ms to the X-ray beam. The tomographic reconstruction was carried out using a GPU-optimized cone beam filtered back-projection algorithm [6] provided by RX Solutions (XACT software, Ver. 1.1). Each tomogram, as a 3D image, was saved as a stack of 2D 16 bit un-signed integer TIFF images. Each 2D image, called "tomographic slice", is a 2D digital cross-section of the volume "tomographically" reconstructed and, in our case, it was approximately orthogonal to the longitudinal direction of the specimen. The slices were equidistant from each other, i.e., the voxels were isotropic, with inter-slice distance equal to the voxel size $\tilde{p}$. Selected region of interest (ROI) slices from the tomogram of the P-Ref specimen are illustrated in Figure S 6, in order to provide some examples for the appearance of the ASR cracks and products in the absence of Cs-doping.

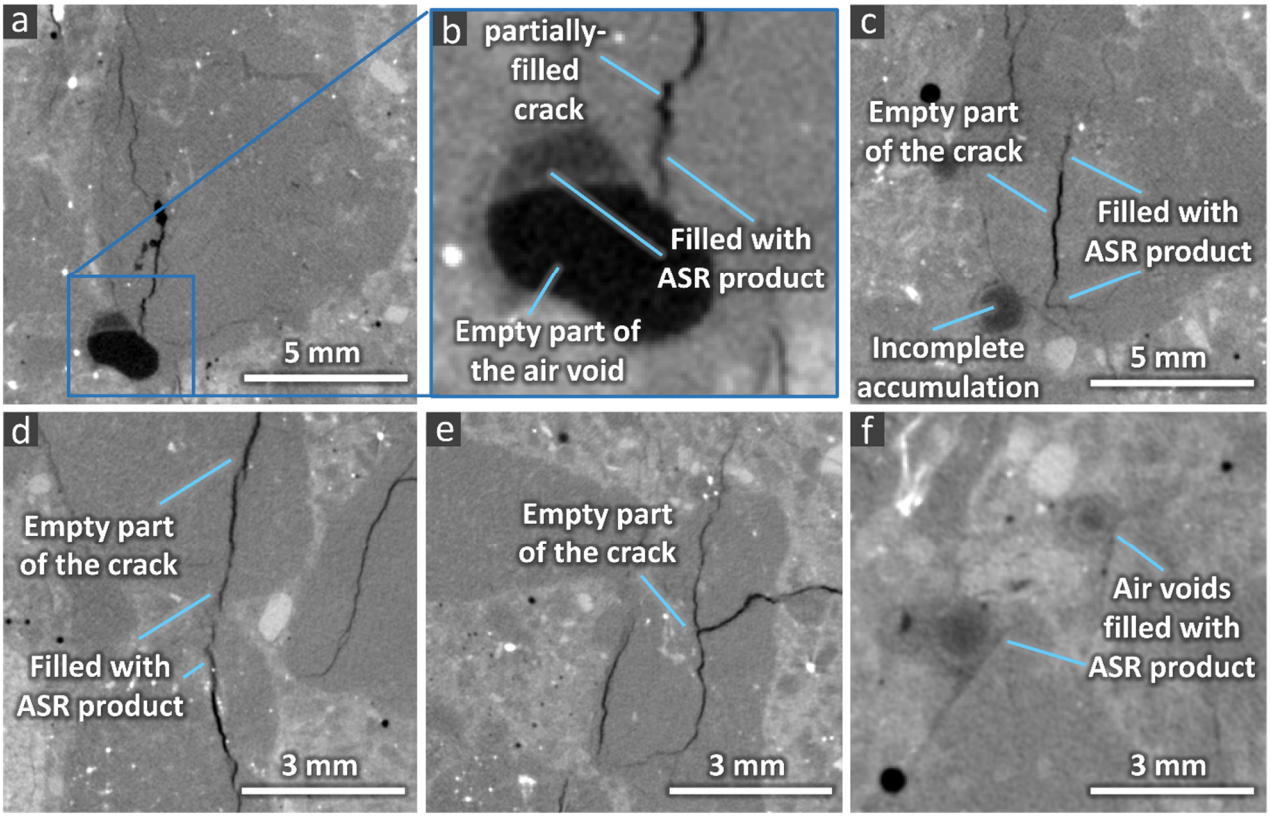

Figure S 6. 2D ROI examples selected from slices in the tomogram of the P-Ref specimen, showing the ASR-induced cracks and air voids filled with ASR products.

S2.2 X-ray attenuation contrast of ASR products doped with alkalis

In order to assess the degree of X-ray attenuation contrast by the ASR products, when "labelled" by alkali ions, X-ray tomography was performed only at the end of a preliminary ASR acceleration experimental campaign. Such campaign involved only specimens cast with Praz aggregates. Distinct specimens were cast by adding to their mix sources of distinct alkalis, specifically Na, K, Rb and Cs. The compound supplying each alkali element was added to the specimen mix in an amount depending on its atomic number. The specimens were cast and underwent ASR acceleration according to the Swiss standard SIA 2042 [7], developed for assessing the degree of ASR-induced expansion in concrete. The specimens (prisms with size of 70 × 70 × 280 mm^3) were subjected to different boundary conditions compared with those used for the time-lapse X-ray tomography campaign. They were stored in a climatic chamber at 100% relative humidity (RH) and at 60 °C, for a total of 168 days. They were cast with mix design identical to that of the X-ray tomography specimens. At 112 days of ASR acceleration time, smaller specimens were cut out, with sizes of 20×20×40 mm^3 and by using a diamond saw, to perform X-ray tomography and assess which alkali doping led to the highest X-ray attenuation contrast for the ASR products compared with the other material phases.

Figure S 7 shows, for each batch of specimens cast with a source of an alkali type, a region of interest (ROI) on a 2D digital cross-section from a corresponding X-ray tomogram of one of the cut specimens. The X-ray tomograms were performed with the same settings as for the time-lapse tomography campaign. For each "tomographed" specimen, the ROI shown in Figure S 7 contains air voids filled with ASR products. At 20 weeks of the implemented ASR acceleration, air void-filling by ASR products was a recurrent feature. It could be exploited for benchmarking and comparing X-ray attenuation contrast levels for the "labelled" ASR products. Figure S 7 (a) and (b) show no significant contrast enhancement obtained by using Na- and K-doping. Rb-doping (Figure S 7 (c)) already allowed visualizing more clearly the ASR products. However, only Cs-doping (Figure S 7 (d)) allowed achieving extremely high X-ray attenuation contrast levels, needed not only to make the products recognizable by a human observer but also to make them identifiable by a segmentation algorithm.

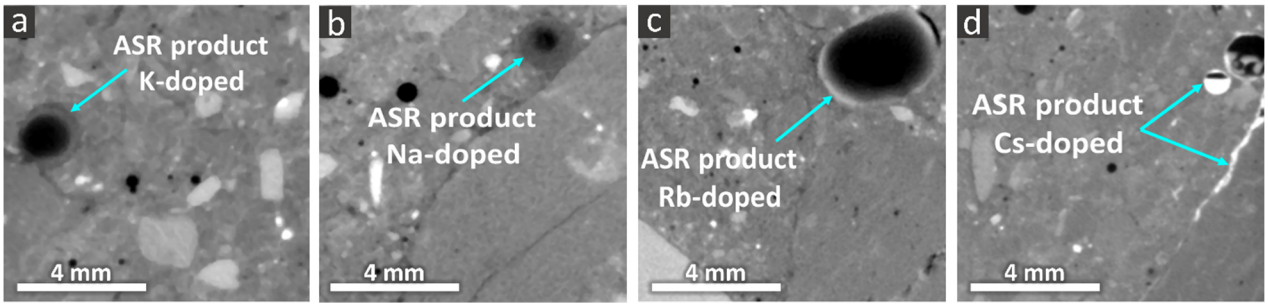

Figure S 7. Examples of regions of interest (ROI) from tomograms of 4 distinct specimens cast with distinct alkali-doping. Each ROI was selected on a 2D digital cross-section from the tomogram of a corresponding specimen. The common feature of each chosen ROI is the presence of air voids. At the late (20 weeks) stage of the used ASR acceleration, air voids were typically partially or almost completely filled with ASR products. The tomograms are ordered from left to right based upon the increasing atomic number of the alkali element (Na, K, Rb and Cs, respectively). ASR products "labelled" by Cs^+ ions increased their X-ray attenuation to a level above that of any other material phase in the specimens, except for some high density/high atomic number minerals in the cement paste. Thus, Cs-labelled ASR products were characterized by the highest X-ray attenuation contrast in our tomograms.

S3. Image processing and analysis of the time-lapse X-ray tomograms

In the following, we indicate with $I(\vec{x}_j, t_i)$ the value of a voxel at position $\vec{x}_j$ in the tomogram at the time point t_i in the series, with $i = 0, 1, \ldots, 11$. The index $j = 1, \ldots N$ just enumerates the voxels in which the volume is discretized, N being the total number of voxels.

S3.1 Image enhancement

For each specimen and at each time point t_i in the time series, the X-ray tomogram was firstly subjected to an edge-preserving noise-reduction processing step, with the goal of smoothing it without significant blurring of edges, e.g., boundaries between distinct material phases. We used a type of anisotropic diffusion filter [8] implemented in Beat Münch's Xlib library of plugins [9] for Fiji/ImageJ [10]. The name of the used plugin is "Anisotropic diffusion". The whole Xlib library can be installed in Fiji/ImageJ by adding its URL (https://sites.imagej.net/Xlib/) to the list of ImageJ plugins repositories for the automatic update of the libraries of plugins. See https://imagej.net/Update_Sites for instructions on how to add plugins repositories to the list for the automatic update.

The following values of the parameters of the "Anisotropic diffusion" plugin were used for noise-filtering each tomogram, independently of the specimen and time point:

- "Anisotropic diffusion method" = "Tschumperle - Deriche"
- "Max # of complete iterations" = 20
- "Time step" = 10
- "Smoothing number per iteration" = 2
- "A1 diffusion limiter" = 0.5
- "A2 diffusion limiter" = 0.7
- "A3 diffusion limiter" = 0.9
- "Edge threshold" = 5
- "Constrain in case of overflow" = true

S3.2 Correction for specimen misalignments

Distinct time-lapse tomograms of the same specimen almost always exhibit specimen misalignment. This means that a reference point on the specimen surface, e.g., a corner, may be not located at the same position of a common and fixed frame of reference in two successive tomograms.

We designed and implemented the tomographic measurements in order to minimize upfront such misalignment. The same specimen holder was always used. Each specimen was positioned with a corner always at the same position on that holder. The holder itself was custom designed and manufactured in order to ease such positioning. Despite all these measures, misalignment was still unavoidable. That occurred and typically occurs because of limitations in the precision with which the same exact specimen can be mounted on the tomograph's specimen/rotation stage at the successive measurement time points. It occurs also because the specimen stage itself can be moved to a nominal position only with a certain accuracy, which, for the tomograph we used, is at the scale of tens of microns. For these reasons, we additionally exploited rigid body registration to further reduce the misalignments between the time-lapse tomograms.

An image registration algorithm typically searches for the optimal vector field, $\vec{T}(\vec{x})$, mapping the positions ($\vec{x}$) of the voxels of a reference image to those ($\vec{x}' = \vec{T}(\vec{x})$) of a second image (called hereafter "deformed image") of the same specimen but after a change. The inverse of such mapping, $\vec{T}^{-1}$, allows for modifying the deformed image such that it becomes approximately aligned with the reference once [11].

In the case of rigid body registration, the set of possible mappings $\vec{T}$ is parametrized as the sum of a rigid translation and a rotation, $\vec{x}' = \vec{T}_{RG}(\vec{x}) = \boldsymbol{R}\vec{x} + \vec{a}$, with $\boldsymbol{R}$ being a 3×3, real-valued and orthogonal matrix with determinant = 1 ($\boldsymbol{R} \in$ to the Lie group $\boldsymbol{SO_3}$), a "rotation matrix", and $\vec{a} \in \mathbb{R}^3$ being a translation vector. In our case, the fixed reference image was always the tomogram at the first time point, $\{I(\vec{x}_j, t_0)\}_{j=1,\dots,N}$, while the deformed image was the tomogram at a successive time point, $\{I(\vec{x}_j, t_i)\}_{j=1,\dots,N}$, $\forall\, i = 1, \dots 11$. The tomogram obtained as output of the rigid body registration is indicated by $\{I_{RB}(\vec{x}_j, t_i)\}_{j=1,\dots,N}$, $\forall\, i = 1, \dots 11$. Such 3D image registration was carried out using the Python application programming interface (API) of the SimpleElastix image registration library [12]. SimpleElastix is an extension of the Elastix C++ image registration library. The latter is based upon the Insight Segmentation and Registration Toolkit (ITK) library [13]. SimpleElastix integrates Elastix with SimpleITK, the latter being a set of bindings to the ITK library offered in several programming languages [12].

The 3D rigid body registration used a multi-resolution scheme [14], [15] and an image similarity metric based on the mutual information of the two populations of voxel values [14], [15], one population corresponding to the reference tomogram at time t_0, the second to the deformed specimen's tomogram, at time t_i. The parameter text file for the 3D rigid body registration included the following settings:

(FixedInternalImagePixelType "short")

(FixedImageDimension 3)

(MovingInternalImagePixelType "short")

(MovingImageDimension 3)

(Registration "MultiResolutionRegistration")

(Interpolator "LinearInterpolator")

(ResampleInterpolator "FinalBSplineInterpolator")

(Resampler "DefaultResampler")

(FixedImagePyramid "FixedRecursiveImagePyramid")

(MovingImagePyramid "MovingRecursiveImagePyramid")

(Optimizer "AdaptiveStochasticGradientDescent")

```
(Transform "EulerTransform")
(Metric "AdvancedMattesMutualInformation")
(AutomaticScalesEstimation "true")
(AutomaticTransformInitialization "true")
(HowToCombineTransforms "Compose")
(NumberOfHistogramBins 64)
(ErodeMask "false")
(NumberOfResolutions 5)
(MaximumNumberOfIterations 1000)
(NumberOfSpatialSamples 20000)
(ImageSampler "RandomCoordinate")
(NewSamplesEveryIteration "true")
(BSplineInterpolationOrder 1)
(FinalBSplineInterpolationOrder 3)
(DefaultPixelValue 0)
(WriteResultImage "true")
(ResultImagePixelType "short")
(ResultImageFormat "mhd")
```

The following is the content of the Python script used to perform the 3D rigid body registration:

```
import SimpleITK as sitk
elastixImageFilter = sitk.SimpleElastix()
elastixImageFilter.LogToConsoleOn()
outDir = "path to output directory"
fixImage = "path to fixed/reference image"
movImage = " path to moving/deformed image "
elastixImageFilter.SetOutputDirectory(outDir)
elastixImageFilter.SetFixedImage(sitk.ReadImage(fixImage))
elastixImageFilter.SetMovingImage(sitk.ReadImage(movImage))
parameterMapVector = sitk.VectorOfParameterMap()
parameterMapVector.append(elastixImageFilter.ReadParameterFile("path to text parameter file"))
elastixImageFilter.SetOutputDirectory(outDir)
```

```
elastixImageFilter.Execute()
elastixImageFilter.GetParameterMap()
transformParameterMap = elastixImageFilter.GetTransformParameterMap()
transformix = sitk.SimpleTransformix()
transformix.SetOutputDirectory(outDir)
transformix.LogToConsoleOn()
transformix.SetTransformParameterMap(elastixImageFilter.GetTransformParameterMap())
transformix.ComputeDeformationFieldOn()
transformix.SetMovingImage(sitk.ReadImage(movImage))
transformix.Execute()
transformix.GetComputeDeformationField()
resultFloatImage2 = transformix.GetResultImage()
sitk.WriteImage(resultFloatImage2,'Result_image.tif')
elastixImageFilter.SetOutputDirectory(outDir)
```

S3.3 Empty crack segmentation

To achieve the segmentation of empty cracks, we used a customized approach. By empty cracks, we mean here cracks with either no ASR products at all or in a very small amount not sufficient to offset the crack voxel value above the typical values for empty regions.

The approach exploited the fact that ASR cracks were, for the tomogram at time t_i, a new feature, compared with the tomogram at t_0. If cracks could appear in the hypothetical absence of any volumetric deformation of the specimen, the difference between the tomogram at t_0 and the tomogram at t_i should give as a result a tomogram where every voxel has value close to 0, except where changes appeared, i.e., where cracking occurred. Segmentation of crack voxels would then be feasible by selecting the voxels in such difference image with values in a certain interval (thresholding). Since cracking is actually a consequence of specimen deformation, the simple difference mentioned above is not useful. Regions at time t_i, not containing cracks, thus unchanged, were not exactly located at the same positions as at t_0. Such regions have, in the difference tomogram, voxel value very different from zero. We addressed this limitation by performing 3D, non-rigid image registration between the output of the processing step described in S3.2 above, at t_i, $\forall\, i = 1, \ldots, 11$, and the tomogram at t_0.

We performed such non-rigid registration in two successive steps. The first step consisted of global affine registration, to compensate for bulk and coarse volumetric changes [16]. The output tomogram of such step was the input for the second step. The latter consisted of non-affine registration, to try to

compensate for spatially heterogeneous deformations [11], [17]. The finally registered tomogram was then subtracted from the tomogram at t_0. This difference tomogram was then segmented by voxel value thresholding.

The details of all these steps are described in the following sub-sections.

3D, global affine registration

The output tomograms of the 3D rigid body registration described in S3.2, $\left\{I_{RB}(\vec{x}_j, t_i)\right\}_{j=1,\ldots,N}$, $\forall\, i = 1, \ldots 11$, were subjected to 3D, global affine registration in order to compensate for the bulk specimen deformation due to ASR. Each $\left\{I_{RB}(\vec{x}_j, t_i)\right\}_{j=1,\ldots,N}$, $\forall\, i = 1, \ldots, 11$, was registered against the reference tomogram $\left\{I(\vec{x}_j, t_0)\right\}_{j=1,\ldots,N}$. The affine mapping vector field, $\vec{x}' = \vec{T}_{AFF}(\vec{x})$, was modelled as the combination of a rotation, a shear transformation, isotropic scaling and a translation:

$$\vec{x}' = \vec{T}_{AFF}(\vec{x}) = (\boldsymbol{S} \cdot \boldsymbol{L} \cdot \boldsymbol{R} \cdot \vec{x}) + \vec{a} \qquad \text{(ES1)}$$

where

$$\boldsymbol{S} = \begin{pmatrix} 1 & S_{12} & S_{13} \\ S_{21} & 1 & S_{23} \\ S_{31} & S_{32} & 1 \end{pmatrix} \qquad \text{(ES2)},$$

$$\boldsymbol{L} = \begin{pmatrix} L_1 & 0 & 0 \\ 0 & L_2 & 0 \\ 0 & 0 & L_3 \end{pmatrix} \qquad \text{(ES3)}$$

and

$$\boldsymbol{R} = \boldsymbol{R}_z(\alpha)\boldsymbol{R}_y(\beta)\boldsymbol{R}_x(\gamma) \begin{pmatrix} cos\,\alpha & -sin\,\alpha & 0 \\ sin\,\alpha & cos\,\alpha & 0 \\ 0 & 0 & 1 \end{pmatrix} \begin{pmatrix} cos\,\beta & 0 & sin\,\beta \\ 0 & 1 & 0 \\ -sin\,\beta & 0 & cos\,\beta \end{pmatrix} \begin{pmatrix} 1 & 0 & 0 \\ 0 & cos\,\gamma & -sin\,\gamma \\ 0 & sin\,\gamma & cos\,\gamma \end{pmatrix} \qquad \text{(ES4)}$$

are 3×3, real-valued matrices with elements independent of $\vec{x}$ (global affine transformation) representing the shear, scaling and rotation transformations, respectively. Equation (ES4) defines an intrinsic rotation whose Euler angles are α, β, γ around the intrinsic Z, Y and X axes, respectively. The term $\vec{a}$ in Eq. (ES1) stands for the translation vector. Since the input to this global affine registration step was a tomogram already rigidly registered against the reference tomogram, the matrix $\boldsymbol{R}$ and the vector $\vec{t}$ in Eq. (ES1) were essentially estimated as the identity matrix and the null vector, respectively, from the affine registration procedure.

We indicate with $\{I_{AFF}(\vec{x}_j, t_i)\}_{j=1,\dots,N}$, $\forall\, i = 1, \dots, 11$, the tomogram obtained as output of this global affine registration. The algorithmic implementation was done also in this case by using the Python API of SimpleElastix. As for the rigid body registration, the image similarity metric was based on the mutual information of the two voxel populations. A multi-resolution scheme was also used. The parameter text file for the 3D affine registration included the following settings:

(FixedInternalImagePixelType "short")

(FixedImageDimension 3)

(MovingInternalImagePixelType "short")

(MovingImageDimension 3)

(Registration "MultiResolutionRegistration")

(Interpolator "BSplineInterpolator")

(ResampleInterpolator "FinalBSplineInterpolator")

(Resampler "DefaultResampler")

(FixedImagePyramid "FixedRecursiveImagePyramid")

(MovingImagePyramid "MovingRecursiveImagePyramid")

(Optimizer "AdaptiveStochasticGradientDescent")

(Transform "AffineTransform")

(Metric "AdvancedMattesMutualInformation")

(AutomaticScalesEstimation "true")

(AutomaticTransformInitialization "true")

(HowToCombineTransforms "Compose")

(NumberOfHistogramBins 64)

(ErodeMask "false")

(NumberOfResolutions 4)

(MaximumNumberOfIterations 1000)

(NumberOfSpatialSamples 20000)

(ImageSampler "RandomCoordinate")

(NewSamplesEveryIteration "true")

(BSplineInterpolationOrder 1)

(FinalBSplineInterpolationOrder 3)

(DefaultPixelValue 0)

(WriteResultImage "false")

(ResultImagePixelType "short")

(ResultImageFormat "mhd")

The Python script used to perform the 3D global affine registration was the following:

```
import SimpleITK as sitk
elastixImageFilter = sitk.SimpleElastix()
elastixImageFilter.LogToConsoleOn()
outDir = "path to output directory"
fixImage = "path to fixed/reference image"
movImage = "path to moving/deformed image"
elastixImageFilter.SetOutputDirectory(outDir)
elastixImageFilter.SetFixedImage(sitk.ReadImage(fixImage))
elastixImageFilter.SetMovingImage(sitk.ReadImage(movImage))
parameterMapVector = sitk.VectorOfParameterMap()
parameterMapVector.append(elastixImageFilter.ReadParameterFile("path to text parameter file"))
elastixImageFilter.SetParameterMap(parameterMapVector)
elastixImageFilter.SetOutputDirectory(outDir)
elastixImageFilter.Execute()
elastixImageFilter.GetParameterMap()
transformParameterMap = elastixImageFilter.GetTransformParameterMap()
transformix = sitk.SimpleTransformix()
transformix.SetOutputDirectory(outDir)
transformix.LogToConsoleOn()
transformix.SetTransformParameterMap(elastixImageFilter.GetTransformParameterMap())
transformix.ComputeDeformationFieldOn()
transformix.ComputeDeterminantOfSpatialJacobianOn()
transformix.SetMovingImage(sitk.ReadImage(movImage))
transformix.Execute()
transformix.GetComputeDeformationField()
transformix.GetComputeDeterminantOfSpatialJacobian()
resultFloatImage2 = transformix.GetResultImage()
sitk.WriteImage(resultFloatImage2,'Result_U0-3_Local_Affine_1-17.tif')
```

elastixImageFilter.SetOutputDirectory(outDir)

3D, non-affine registration

The tomograms $\{I_{AFF}(\vec{x}_j, t_i)\}_{j=1,\dots,N}$, $\forall\, i = 1, \dots, 11$, were registered against $\{I(\vec{x}_j, t_0)\}_{j=1,\dots,N}$ according to a non-affine transformation model, $\vec{x}' = \vec{T}_{N-AFF}(\vec{x})$, parametrized by using a cubic B-spline expansion [15], [18]. Such registration allows compensating for spatially varying deformations, thus for the part of the ASR-induced deformations being spatially heterogeneous, e.g., highly localized. The output of such registration was the set of tomograms $\{\tilde{I}(\vec{x}_j, t_i)\}_{j=1,\dots,N}$, $\forall\, i = 1, \dots, 11$.

The Python API of SimpleElastix was used to program also this type of registration, still using a multi-resolution scheme and an image similarity metric based upon the mutual information of the two voxel populations. The parameter text file for the 3D affine registration included the following settings:

(FixedImageDimension 3)

(MovingImageDimension 3)

(FixedInternalImagePixelType "short")

(MovingInternalImagePixelType "short")

(Registration "MultiMetricMultiResolutionRegistration")

(FixedImagePyramid "FixedSmoothingImagePyramid")

(MovingImagePyramid "MovingSmoothingImagePyramid")

(Interpolator "BSplineInterpolator")

(Metric "AdvancedMattesMutualInformation" "TransformBendingEnergyPenalty" "TransformRigidityPenalty")

(Metric0Weight 1)

(Metric1Weight 0.1)

(Metric2Weight 0.4)

(UseLinearityCondition "true")

(UseJacobianPreconditioning "false")

(Optimizer "AdaptiveStochasticGradientDescent")

(ResampleInterpolator "FinalBSplineInterpolator")

(Resampler "DefaultResampler")

(Transform "BSplineTransform")

(ErodeMask "false")

(AutomaticScalesEstimation "true")

(AutomaticTransformInitialization "true")

(AutomaticTransformInitializationMethod "Origins")

(NumberOfResolutions 3)

(FinalGridSpacingInVoxels 64.0)

(MaximumNumberOfIterations 700)

(HowToCombineTransforms "Compose")

(UseFastAndLowMemoryVersion "true")

(NumberOfHistogramBins 64)

(FixedKernelBSplineOrder 3)

(MovingKernelBSplineOrder 3)

(ImageSampler "RandomCoordinate")

(UseRandomSampleRegion "false")

(NumberOfSpatialSamples 10000)

(NewSamplesEveryIteration "true")

(CheckNumberOfSamples "true")

(MaximumNumberOfSamplingAttempts 5)

(BSplineInterpolationOrder 1)

(FinalBSplineInterpolationOrder 3)

(DefaultPixelValue 0)

(SP_a 2000.0)

(SP_A 50.0)

(SP_alpha 0.6)

(GetJacobian "false")

(WriteTransformParametersEachIteration "false")

(WriteResultImage "true")

(CompressResultImage "false")

(WriteResultImageAfterEachResolution "false")

(ShowExactMetricValue "false")

(ResultImagePixelType "short")

(ResultImageFormat "mhd")

The Python script for such 3D non-affine registration was the following:

```
import SimpleITK as sitk
elastixImageFilter = sitk.SimpleElastix()
elastixImageFilter.LogToConsoleOn()
outDir = "path to output directory"
fixImage = "path to fixed/reference image"
movImage = "path to moving/deformed image"
elastixImageFilter.SetOutputDirectory(outDir)
elastixImageFilter.SetFixedImage(sitk.ReadImage(fixImage))
elastixImageFilter.SetMovingImage(sitk.ReadImage(movImage))
parameterMapVector = sitk.VectorOfParameterMap()
parameterMapVector.append(elastixImageFilter.ReadParameterFile("path to text parameter file"))
elastixImageFilter.SetParameterMap(parameterMapVector)
elastixImageFilter.SetOutputDirectory(outDir)
elastixImageFilter.Execute()
elastixImageFilter.GetParameterMap()
transformParameterMap = elastixImageFilter.GetTransformParameterMap()
transformix = sitk.SimpleTransformix()
transformix.SetOutputDirectory(outDir)
transformix.LogToConsoleOn()
transformix.SetTransformParameterMap(elastixImageFilter.GetTransformParameterMap())
transformix.ComputeDeformationFieldOn()
transformix.ComputeSpatialJacobianOn()
transformix.ComputeDeterminantOfSpatialJacobianOn()
transformix.SetMovingImage(sitk.ReadImage(movImage))
transformix.Execute()
transformix.GetComputeDeformationField()
transformix.GetComputeSpatialJacobian()
transformix.GetComputeDeterminantOfSpatialJacobian()
resultFloatImage2 = transformix.GetResultImage()
sitk.WriteImage(resultFloatImage2,'Result_U0-3_BS_1-16.tif')
elastixImageFilter.SetOutputDirectory(outDir)
```

Final empty crack segmentation

Each tomogram $\{\tilde{I}(\vec{x}_j, t_i)\}_{j=1,\dots,N}$, $\forall\, i = 1, \dots, 11$ (Figure S 8 (b)), is a version of the original one, $\{I(\vec{x}_j, t_i)\}_{j=1,\dots,N}$, but deformed as such both the misalignment due to the specimen repositioning at each measurement time point t_i and the deformations induced by ASR are compensated for. Thus, each of them approximately matches the reference tomogram, except at locations where the ASR cracks appeared between the reference time t_0 and time t_i. As mentioned above, we used the voxel-wise difference between $\{I(\vec{x}_j, t_0)\}_{j=1,\dots,N}$ and $\{\tilde{I}(\vec{x}_j, t_i)\}_{j=1,\dots,N}$ as a 3D spatial map of a (sort of) "likelihood" for the voxel to be inside a (empty or filled by a small amount of ASR products) crack (Figure S 8 (c)).

This approach is a relatively well-stablished method in quantitative medical diagnosis based on time-lapse X-ray or Magnetic Resonance (MRI) imaging. It is usually named as "Temporal Subtraction (TS)" [19]–[21]. By the choice of a "likelihood" range, made by the image analyst, that 3D scalar field of likelihood was converted into a binary one (also called a binary tomogram), coded using 8-bit unsigned integer numbers and a value of 0 for a voxel outside a crack and of 255 otherwise.

Due to noise and partial volume effects in $\{I(\vec{x}_j, t_0)\}_{j=1,\dots,N}$ and $\{\tilde{I}(\vec{x}_j, t_i)\}_{j=1,\dots,N}$, each of such binary tomogram for ASR-related cracks still contained artefacts, in the form of small and rather spherical sets of connected voxels ("clusters") which did not actually fall within newly formed cracks. These clusters were algorithmically selected by computing, for each set of connected voxels in the binary tomogram, a feature variable SD:

$$SD = \frac{S_{sphere}}{S_{\partial\Omega}} \qquad \text{(ES5)}$$

where S_{sphere} is the surface area of a sphere with volume equal to the total volume of the voxel set and $S_{\partial\Omega}$ is its actual boundary surface ($\partial\Omega$) area. SD measures the "sphericity degree" of the voxel cluster [22]. Clusters with SD values close to 1 are highly spherical. Clusters corresponding to the actual cracks had SD values much smaller than 1. That should be expected, since cracks are 3D objects with high shape anisotropy. All the clusters with $SD > 0.4$ were selected and excluded from the previous binary tomogram, obtaining a new one called in what follows as $\{\tilde{I}^B_{ASR\ crack}(\vec{x}_j, t_i)\}_{j=1,\dots,N}$. This binary tomogram acted as the final spatial map of the voxels identified as belonging to (empty) ASR crack volume newly formed at time t_i compared with time t_0. In order to be able to compute the total volume of cracks, including what already existed in the tomogram at t_0, thus not due to ASR, an additional crack segmentation workflow, consisting of the following steps, was implemented.

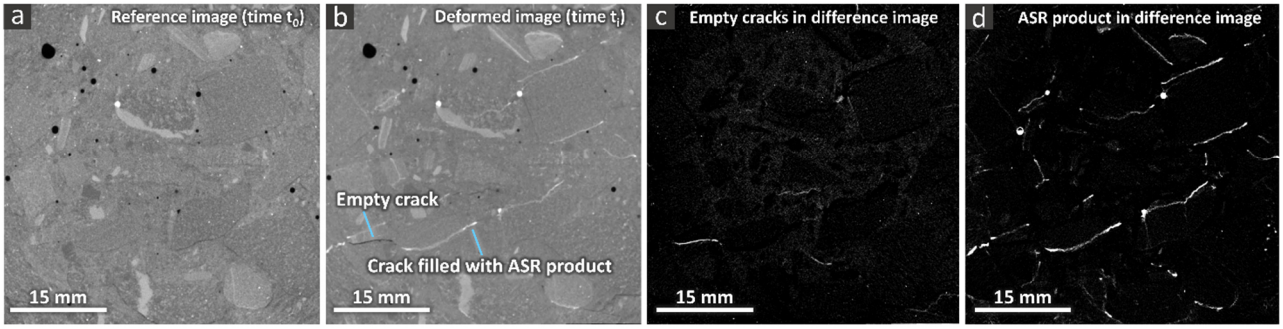

Figure S 8. Example tomographic slices for the U-Cs specimen, showing the reference and deformed tomograms, (a) and (b), along with the results of the temporal subtractions (STs) for obtaining the empty cracks and cracks and air voids filled with ASR products. (a): a slice from the reference tomogram at the first time point, t_0; (b) slice at the same exact position as that in (a) but from tomogram at about 195 days, after the full chain of registrations; results of the two distinct TSs, showing the empty cracks in (c) and the segmented pore space filled with ASR products in (d), respectively. See Section S3.4 for details about the segmentation of ASR products inside cracks.

A black top-hat (BTH) transform was applied to $\{I(\vec{x}_j, t_0)\}_{j=1,\ldots,N}$. It is a mathematical morphology operator acting on binary as well as grey-level images. When applied to grey-level images (like our tomograms), it produces a new grey-level image as output, with pixel/voxel value having the meaning of likelihood that a certain object's area/volume includes, in the input image, that pixel/voxel. The object has a specific shape and must have on average lower pixel/voxel value than in its surroundings. Thus, such transform allows mapping out regions (1) containing local minima and (2) being specifically shaped [23]. By thresholding the transform's output, it is possible to obtain a binary image segmenting the chosen type of objects out of the original image. The predefined shape of the object is determined by choosing the structuring element (SE) of the morphological operation used in the transform (a morphological opening). As SE, a 3D thin disk, with size of $S_{BTH} = 3$ voxels was used. Such choice was motivated by the fact that empty cracks are (1) 3D regions with high shape anisotropy (i.e., high aspect ratios), in addition to (2) containing local minima of the original grey-level image. The actual software implementation of such transform was based on the module "Edit New Label Field" (in the Segmentation tab) of Avizo 3D, an image processing software suite by Thermo Fisher Scientific.

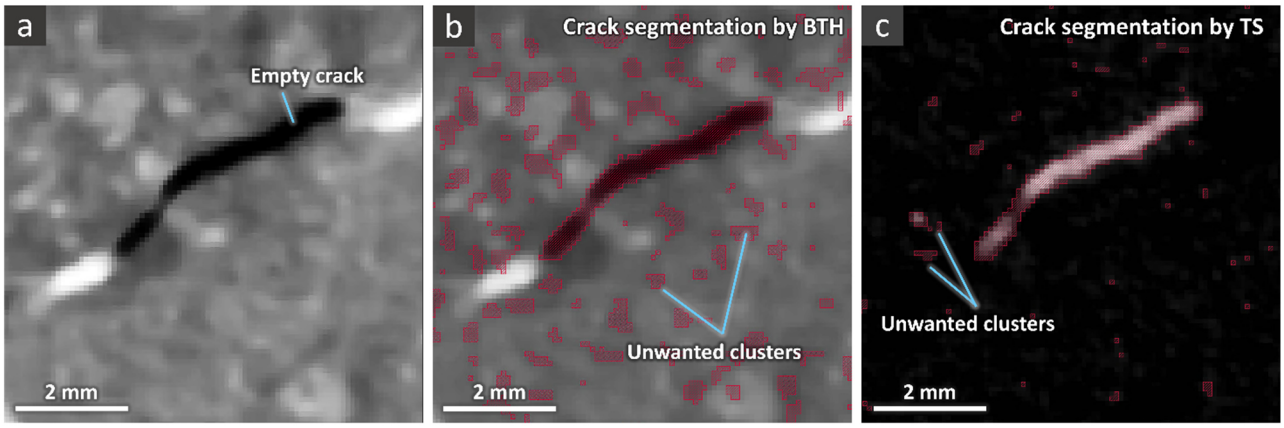

Figure S 9. Comparison of empty crack segmentation results obtained by the "black top-hat (BTH) transform + thresholding" and by the "temporal subtraction (TS) + thresholding" procedures. (a): example ROI selected from one slice of the U-Cs specimen's tomogram at a certain time t_i, containing a partially empty crack; (b) the binary tomogram of empty cracks obtained from the BTH segmentation, superimposed on top of the same image as in (a) and rendered in semi-transparent red color;; (c) binary tomogram of empty cracks obtained from the TS segmentation, superimposed on top of the subtraction image ($\{I(\vec{x}_j, t_0)\}_{j=1,\dots,N}$-$\{\tilde{I}(\vec{x}_j, t_i)\}_{j=1,\dots,N}$). The comparison of (c) and (b) shows that the empty crack segmentation based upon the TS-based approached was less affected by artefacts and errors.

The result of the sequence BTH transform → thresholding was a binary tomogram, which was subjected to the same sphericity-based filtering described above, to exclude cluster voxels not belonging to actual cracks. In comparison with the binary tomograms obtained by the registration → temporal subtraction → thresholding procedure, those produced by the BTH transform → thresholding contained by far much more artefacts due to noise and partial volume effect. See Figure S9 for a comparison. Due to this reason, we used the BTH empty crack segmentation procedure only at t_0.

The resulting binary tomogram, called $\{I^B_{crack}(\vec{x}_j, t_0)\}_{j=1,\dots,N}$, was then Boolean-added, by a Boolean OR operator, to each $\{\tilde{I}^B_{ASR\ crack}(\vec{x}_j, t_i)\}_{j=1,\dots,N}$, $\forall\ i = 1, \dots, 11$, to obtain at each t_i a binary tomogram of total crack volume (called $\{I^B_{crack}(\vec{x}_j, t_i)\}_{j=1,\dots,N}$), independently of whether generated by ASR or pre-existing it.

We remind again that the latter binary tomograms provide an identifying (or label) map of voxels contained in empty crack regions. The adjective "empty" is used not with absolute meaning. It rather means that such segmented crack regions either contained no ASR products at all or contained them in low enough volume fraction and/or with low enough concentration of bound Cs^+ ions such that their X-ray attenuation was extremely small, similar to that of empty air. Crack regions containing ASR

products in large enough volume fraction and with large enough Cs concentration were characterized by voxel values very larger compared with the surrounding, as shown in Figure 5 of the article and in Figure S7 (d) above. Thus, they were segmented according with the procedure described in the following section S3.4 and generically defined as "ASR products regions".

Remarks and segmentation results validation

The chosen and implemented ASR crack segmentation workflow has both advantages and disadvantages compared with any other workflow not relying on non-rigid registration followed by subtraction. The tomogram $\{\tilde{I}(\vec{x}_j, t_i)\}_{j=1,\dots,N}$, $\forall\, i = 1, \dots, 11$, output after the B-spline-based registration, does not contain any more the same exact cracks as in the tomogram after rigid-body registration, $\{I_{RB}(\vec{x}_j, t_i)\}_{j=1,\dots,N}$, $\forall\, i = 1, \dots, 11$. That is an intrinsic consequence of the non-rigid registration itself. Our TS workflow cannot return exactly the same results, especially the orientation of the cracks, as any other crack segmentation workflow using as input only $\{I_{RB}(\vec{x}_j, t_i)\}_{j=1,\dots,N}$, $\forall\, i = 1, \dots, 11$. However, this limitation does not necessarily imply that this workflow produces less reliable results. A segmentation workflow which uses $\{I_{RB}(\vec{x}_j, t_i)\}_{j=1,\dots,N}$ as the only data and information source for segmentation can also perform worse due to, e.g., image noise and partial volume effects. Since any segmentation approach has a limited degree of reliability, which is, by itself, difficult to assess because a ground truth segmentation result is not available [24], what is important is to understand the differences in errors made by distinct segmentation approaches.

To assess such differences, we performed a test analysis to understand the advantages and disadvantages of the TS-based segmentation of empty cracks. For such analysis, we implemented the crack segmentation workflow based upon the BTH (already used only for segmenting the ASR-pre-existing cracks in the tomogram at t_0) for segmenting both ASR-induced and pre-existing cracks in a tomogram at t_i, $\{I_{RB}(\vec{x}_j, t_i)\}_{j=1,\dots,N}$. We considered such alternative workflow as a reference segmentation, since it uses as information for the segmentation only the voxel values of the tomogram to be segmented. The latter is a typical feature of the most frequently used segmentation algorithms/workflows. The results of crack segmentation based on the BTH-based approach were then compared with the segmentation results obtained with the TS-based one. There are two important features associated with the quality of the crack segmentation: the volume fraction of segmented cracks (empty crack volume *per* unit volume of specimen); second, their shape/orientation. Therefore, the comparisons were carried out under two distinct conditions to evaluate both features: (1) segmenting the cracks using both methods applied to exactly the same (non-affinely registered) tomogram; (2) segmenting the cracks by applying the BTH approach to the non-registered tomogram (at time t_i) and using the TS approach for the same tomogram but after non-affine registration. Using the first test

allows to quantify the volume fraction of the segmented crack in the exact same tomogram using both techniques. The second test is mainly useful both for evaluating the volume fraction of the segmented cracks and also their overall shape/orientation change (due to the non-affine registration).

Figure S 10 shows two distinct examples of the segmentation results for the U-Cs specimen at t_{11}= 250 days and regarding the first evaluation procedure. It is observed that the TS technique resulted in a more accurate segmentation, especially in the case of finer cracks, compared to the one obtained by the BTH-based technique. The TS-based approached led to an empty crack volume fraction 25 ± 1.5 % larger than that obtained by the BTH-based approach. This means a remarkable improvement of the segmentation results because, as shown in the two examples of Figure S 10, the BTH-based approach systematically "missed" some crack regions. Furthermore, the overall TS-based segmentation was carried out faster and was easier to implement. The human intervention in the TS segmentation is also less than the one of the BTH.

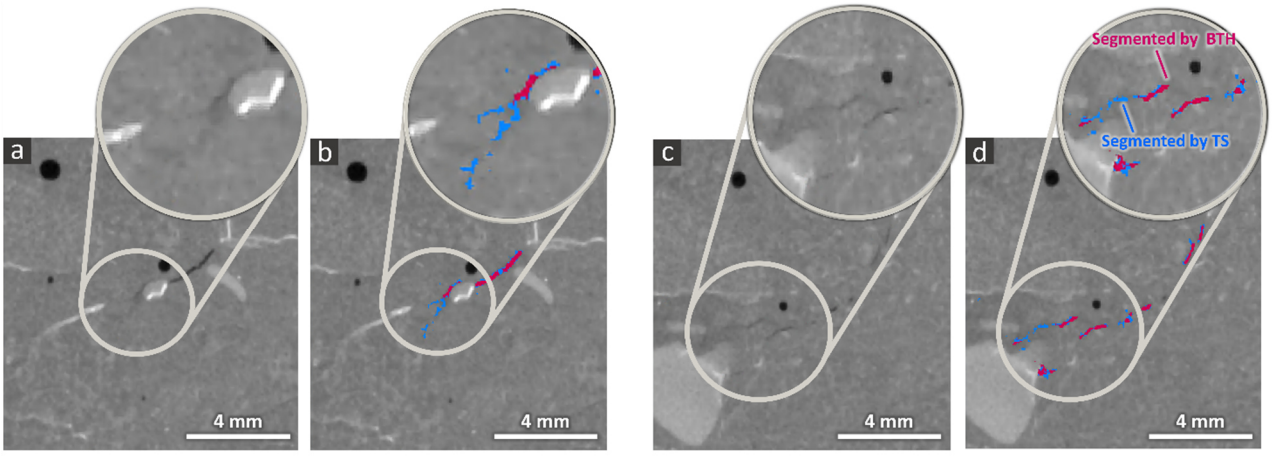

Figure S 10. Two distinct examples of segmentation results from two different regions of the U-Cs specimen's (non-affinely registered) tomogram at 250 days, obtained by the BTH-based and the TS-based approaches. (a) and (c): two slices from two distinct regions of the tomograms, with, highlighted, some cracks. (b) and (d): comparison of the binary tomograms of the empty cracks obtained with the two distinct approaches. For each region, each binary tomogram is superimposed on top of the grey-level tomogram. The binary tomogram obtained by the TS method-based approach is colored in blue, whereas the one obtained by the BTH-based approach is colored in pink.

Figure S 11 shows some results for some small volumes of interest (VOIs) of the tomogram of the U-Cs specimen and at the time point t_{11}= 250 days. Our TS approach segmented crack volumes which were displaced compared with those produced by the reference segmentation based upon the BTH approach, the latter using only $\{I_{RB}(\vec{x}_j, t_i)\}_{j=1,\ldots,N}$. However, no significant changes in orientation,

shape and sizes were observed. This suggests that the mapping vector field $\vec{x}' = \vec{T}_{N-AFF}(\vec{x})$ represented by the B-spline expansion acted locally, in the crack region, mainly as a translation vector. The translation was typically at the scale of a few voxels. The volume of the segmented cracks, in the chosen VOIs, showed only a subtle difference of 0.7 ± 0.05 % when obtained by the TS-based approach rather than the BTH-based one.

Such degree of translation in the segmented cracks, compared with where they were actually located, did not have significant negative impact on the analysis. That is because our targets did not require determining quantitatively the absolute positions of the crack regions. On the contrary, we aimed at both tracking qualitatively the crack network's spatial-temporal evolution and quantifying some of their features, such as size, volume, shape and orientation. However, the TS workflow may not be useful in applications where the exact spatial position of the cracks needs to be preserved and retrieved.

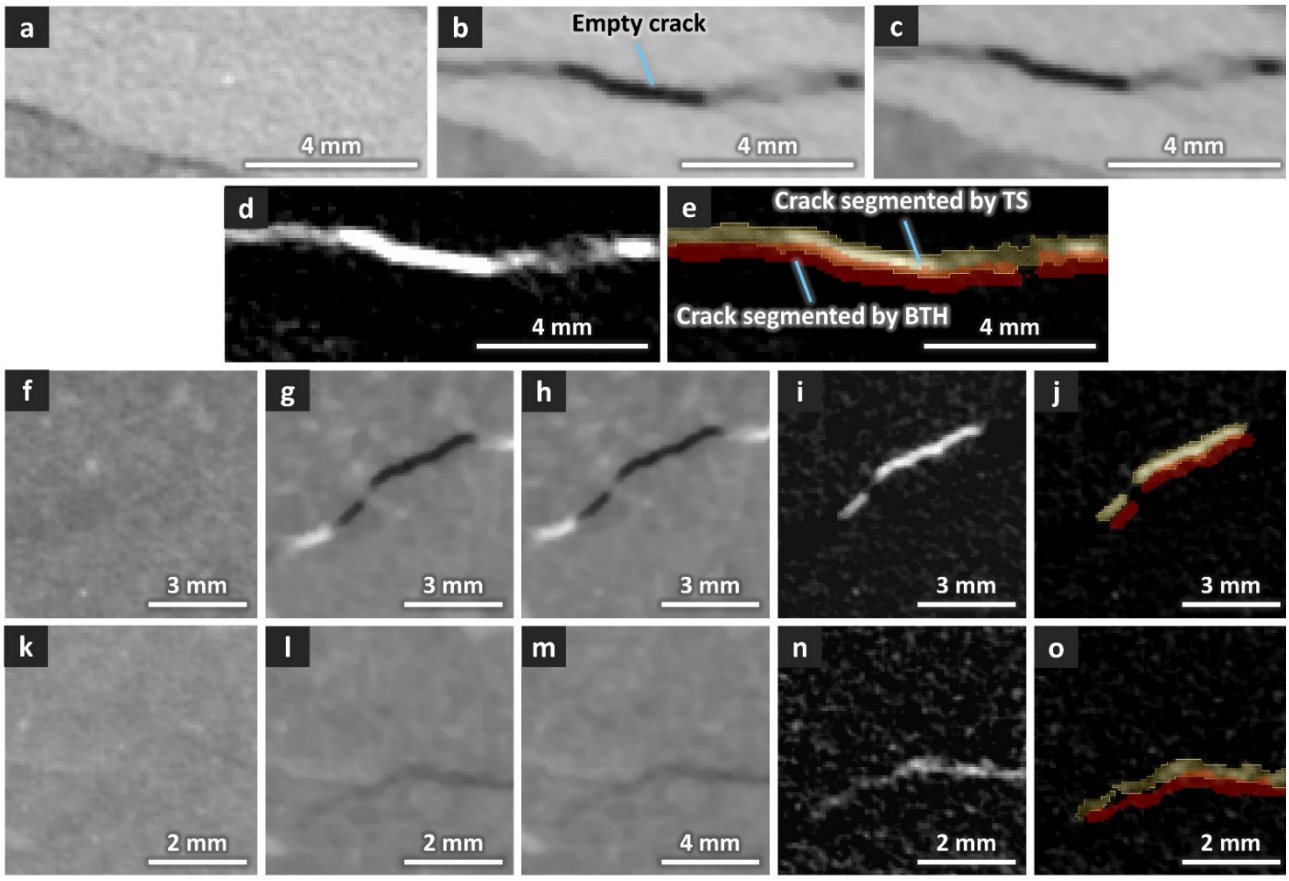

Figure S 11. Evaluation of the effects of non-affine registration on the shape and orientation of ASR-induced cracks, in 3 small volumes of interest (VOIs) of the U-Cs specimen at t_{11}= 250 days. Only one slice from each VOI is shown. (a) One VOI in the reference tomogram, at t_0= 1 day. (b) Same VOI as in (a) but from the rigidly registered tomogram at time point t_{11}= 250 days. (c) Same VOI as in (a) but from the deformed tomogram at time point t_{11}= 250 days, obtained after the rigid, affine

and non-affine registrations, respectively. (d) Same VOI as in (a) but from the difference tomogram which is the result of subtracting the tomogram shown in (c) from the one in (a), as needed for the TS-based empty crack segmentation. (e) Superimposed results of the crack segmentation over the image in (d). The binary tomogram shown in semi-transparent yellow corresponds to the result of the TS segmentation (thresholding from (d)). The binary tomogram in red shows the results obtained with the BTH-based approached applied directly to the non-registered tomogram shown in (b). The third (insets (f) to (j)) and fourth (insets (k) to (o)) rows present two other examples from other VOIs, with the same order as specified for the first example of insets (a) to (e).

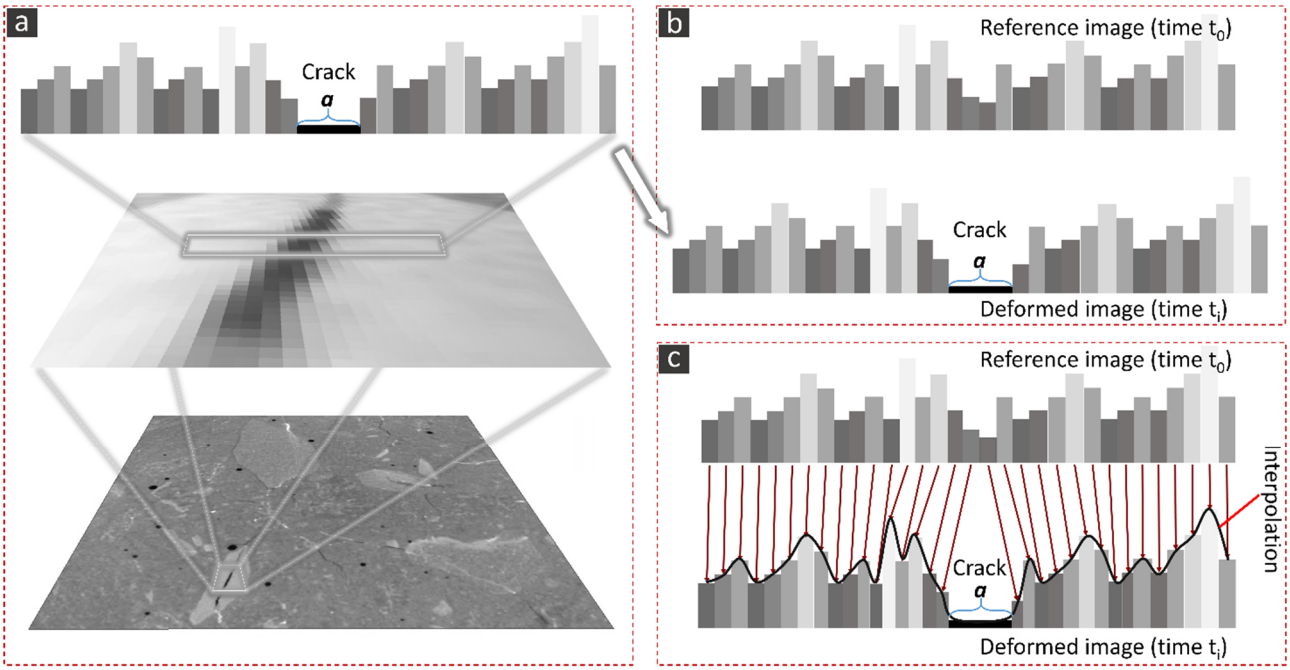

Figure S 12. Schematic illustration of the optical flow concept in non-affine image registration: (a) a crack, shown at higher resolution (middle image) in an actual tomogram (slice thereof shown at the bottom) and a one-dimensional profile from it crossing the crack thickness (top image, schematic cartoon only); (b) comparing the reference state (time t_0) and the state after cracking (deformed image at time t_i) in the same schematic image and (c) comparing the deformed image to its corresponding image after non-rigid (b-spline) registration.

The reason why the shape and size of the cracks segmented by the TS-based workflow were approximately preserved, despite the overall tomogram containing them was deformed, lies, on three intrinsic features of the type of non-rigid registration used (affine + non-affine based on a B-spline expansion):

1. the assumption of "image intensity conservation" (also termed "optical flow equation" [25]), i.e., that a portion (i.e., voxel) of the object gets moved as a consequence of the deformation but keeps its image (voxel) value at the two time points (Figure S 12); written in equations this means that $I\left(\vec{T}_{real}\left(\vec{x}_j\right), t_i\right) = I(\vec{x}_j, t_0)$, where $\vec{T}_{real}(\vec{x})$ is the actual mapping vector field which the registration algorithm tries to approximate as accurately as possible.

2. the chosen image similarity metric, whose maximization drives the search for the optimal approximation of $\vec{T}_{real}(\vec{x})$, depends only upon the statistics of voxel values and not on other features of the tomograms;

3. since the ASR cracks exist in the tomogram at t_i but not at t_0, the regions containing them not only contribute to violate the assumption at point Nr. 1, impairing locally the registration itself, but there is also no possible realization of $\vec{T}(\vec{x})$ which could make their local deformation contribute to increase the image similarity metric; thus, it is as if the registration workflow could not properly deform locally such regions because it lacks the information for doing so. Figure S 13 shows, by a very simplified toy case study, this fact. It reports the results of the same crack segmentation procedure based on the TS approach applied to the case where the only difference between the reference image (Figure S 13 (a)) and the "deformed" one (Figure S 13 (b)) is a new feature appearing only in the latter and being like a thin dark stripe, simulating an empty crack . No other difference exist between the reference and the deformed images, i.e., no kind of deformation at all. Instead, just a part of the reference image, in the form of a thin rectangular stripe, has been "zeroed". It can be observed that the "affine + non-affine" registration chain preserves all the features common in both the reference and the deformed image. In addition, it perfectly adds the new feature of the deformed image to the registration result, without deforming it at all. This suggests that the mentioned two steps of registration cannot "identify" any local deformation of the "deformed" image which could increase the local matching of the registration result with the reference image. Therefore, such feature is exactly reproduced into the resulting, registered image without being modified (Figure S 13 (c));

4. the B-spline expansion representation of each vector component of $\vec{T}_{real}(\vec{x})$ can extend (i.e. copy) to the crack regions the same expression determined as optimal for its nearest neighbouring regions, leading to a $\vec{T}(\vec{x})$ which locally is just constant (pure translation) across a crack region (Figure S 14). A mapping vector field locally across the crack regions, acts as a constant translation which preserves size, orientation and shape.

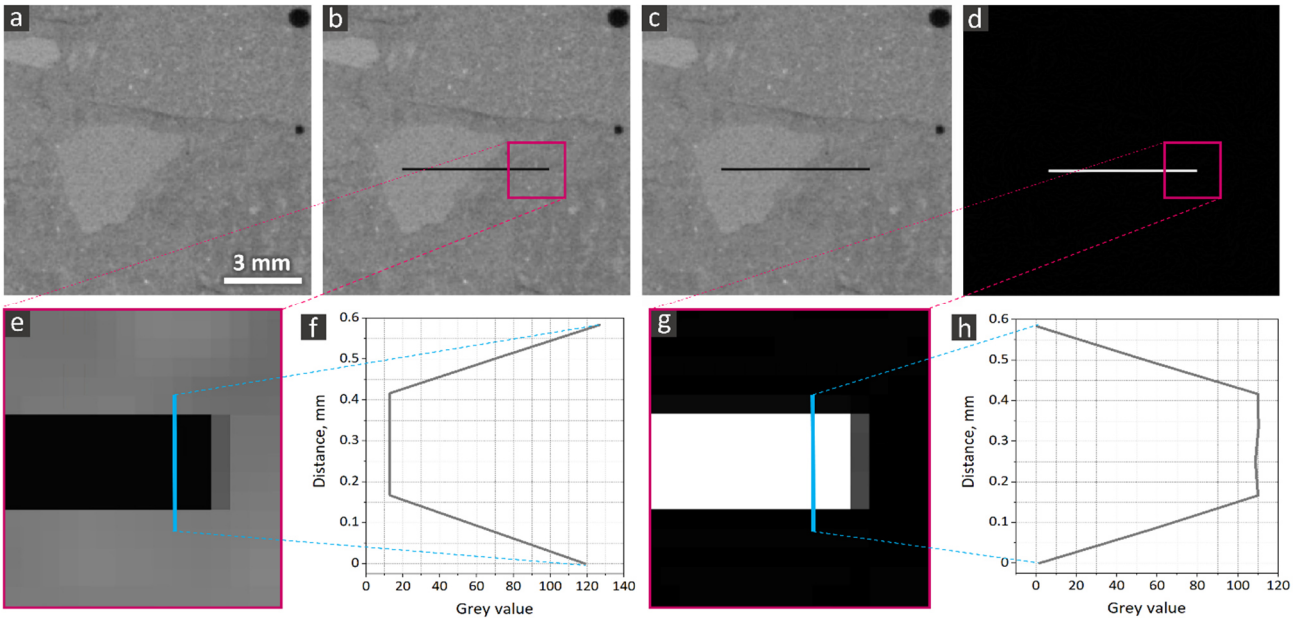

Figure S 13. Evaluating the effect of "affine + non-affine" registrations on a newly emerged feature (a black, crack-like, stripe in this example) in the deformed image, compared with the reference one, without any actual deformation or other change having occurred to produce the deformed image. (a) Reference image (a slice from a small ROI from one of the tomograms). (b) "Deformed" image, obtained from (a) just by reassigning value = 0 (i.e., black) to some of its pixels, constituting a thin rectangular stripe. (c) Resulting image after "affine + B-spline" registration of (b) against (a). (d) Result of subtraction of (c) from the reference image shown in (a). (e) and (g) Magnified region in the tip of the crack-like feature shown in (b) and (d), respectively. (f) and (h) The corresponding profile of the pixel values along the blue lines shown in figures (e) and (g), respectively, comparing the width of the crack-like feature before and after the image registration.

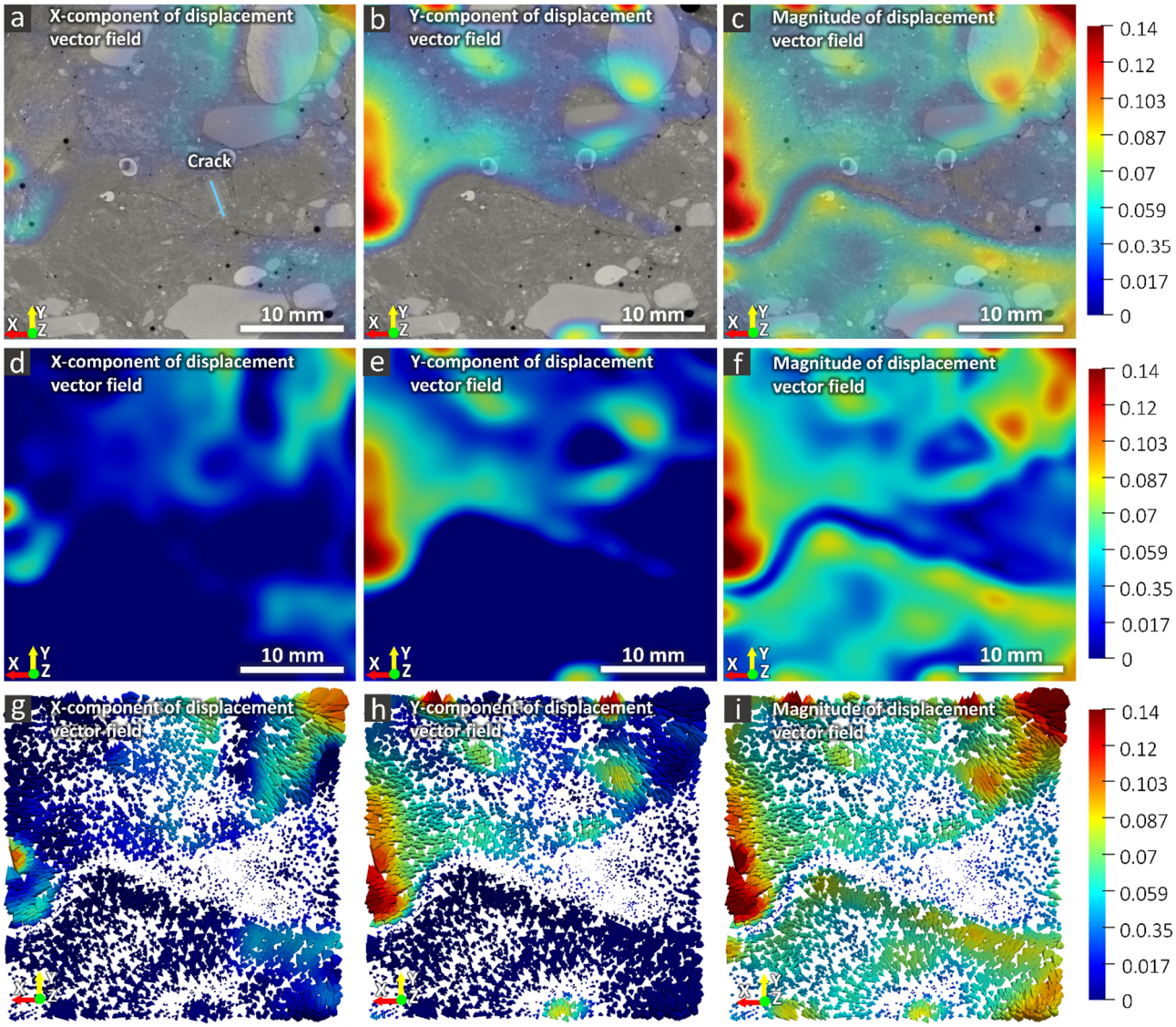

Figure S 14. An example for demonstrating the magnitude of deformation filed, $\|\vec{u}_{N-AFF}\|(\vec{x}, t_i)$, around a cracked region: (a), (b) and (c) superimposed X and Y components and magnitude of the deformation vector filed, respectively, over the corresponding slice and (d), (e) and (f) the components, with the same order mentioned in (a), (b) and (c), but not superimposed over the slice (g)-(i) the same images as shown in insets (d)-(f) but demonstrating the deformation filed, $\vec{u}_{N-AFF}(\vec{x}, t_i)$, with conic glyphs at some grid points.

Figure S 15 summarizes the effects of the different registration steps used in the TS-based crack segmentation procedure on the cracks and their surroundings using a simplified model system. Such model system consists of an artificially created, 2D reference image (Figure S 15 (a)) which was deformed in a way to simulate the deformations due to ASR cracking, including the crack opening (Figure S 15 (b)). The surrogate cracks in this model system are two wedge-like regions with pixel value = 0, introduced in the deformed image of Figure S 15 (b). Based on the introduction of such

surrogate cracks, the remaining portions of the reference image were displaced, rotated and deformed as to simulate ASR cracking and expansion.

The affine registration (Figure S 15 (c)) tries to match the deformed image with the reference one globally. To do so, it relies only on the similar portions in both images. Therefore, the deformed texture (a sort-of "microstructure"), moved in Figure S 15 (b) due to the emergence of the two "cracks", has to be "compressed" back in a way such that it falls approximately back into the same region occupied by the frame of the reference image. Nevertheless, the cracks remain intact in the resulting final image after the registration is done (Figure S 15 (c)). Phenomena similar result also applies when the affine registration is followed by the B-spline-based non-affine one (Figure S 15 (d)). Only similar portions of the image get involved in the registration, which also tries to correct for the spatially heterogeneous part of the deformations, not accounted for by the global affine registration. The cracks still remain intact in the new resulting image (Figure S 15 (d)).

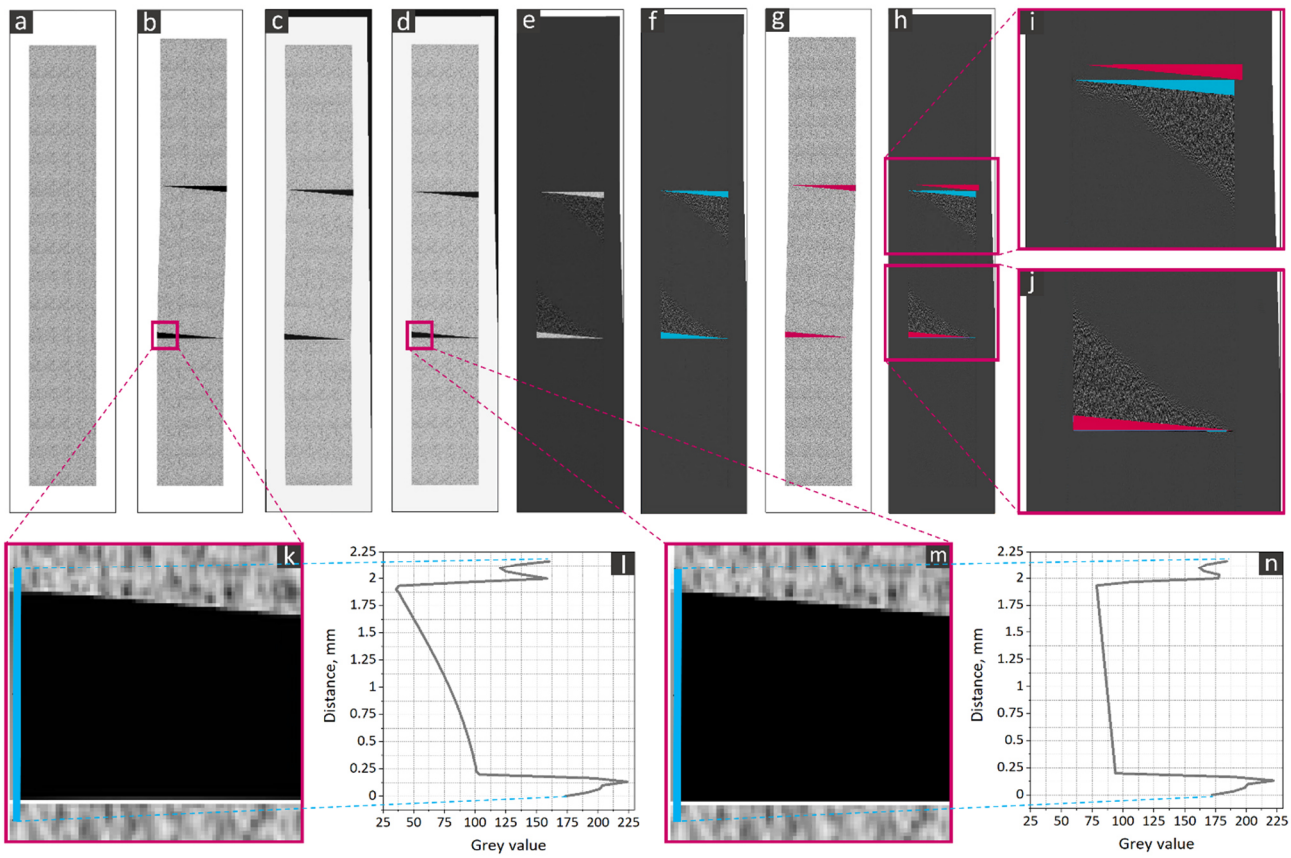

Figure S 15. The effects of different registrations (affine and non-affine), used in the TS-based segmentation, as evaluated on a model, 2D case study where a uni-directional expansion occurred as a consequence of the appearance of new, crack-like features. (a) Reference, artificially created, 2D image. (b) Deformed image, artificially obtained from (a) by inserting two new features, each with the

shape of a triangular wedge and with pixel values = 0, simulating cracks, and by deforming correspondingly the rest of the image as to simulate the effects of ASR crack opening for such toy case. (c) Resulting image after affine registration. (d) Resulting image after "affine + non-affine" registration. (e) Result of subtracting the "affine + non-affine" registered image (shown in (d)) from the reference image (shown in (a)), as done in the TS-based crack segmentation procedure for the real tomograms. (f) Binary image of the segmented "cracks" superimposed over the subtracted image after "affine + non-affine" registration (shown in (e)) and obtained by the TS-based segmentation method. (g) Binary image of the segmented "cracks" (the wedges) superimposed over the deformed image (shown in (b)), rendered as semi-transparent in pink and obtained by BTH-based crack segmentation procedure, used in this case as the reference ("ground-truth") segmentation method. (h) Superposition of both types of binary images (shown in (f) and (g)) over one image to enable an easier comparison. (i) and (j) magnification of the regions in (h) containing the segmented "cracks". (k) and (m) Magnified region at the tip of the "crack" shown in (b) and (d), respectively. (l) and (n) Profiles of the pixel values of (k) and (m) along the blue lines shown on figures (e) and (g), respectively, comparing the "crack" width before and after the "affine + non-affine" registration.

We summarize the advantages of the TS-based segmentation workflow in the two following points.

(1) Compared with the reference segmentation workflow based upon the BTH, the amount of small, quasi-spherical voxel clusters falsely classified as belonging to crack regions because of, e.g., partial volume effects was significantly smaller for the TS-based workflow. Although in both cases the final ASR crack binary tomogram was obtained after applying the sphericity-based filter described before, the false positive segmentation rate was still lower with the registration + subtraction workflow. This result is clearly expectable, since the subtraction operation intrinsically contributes to avoid such false positive segmentation results.

(2) The registration + subtraction workflow could segment regions of cracks with thickness close to the tomogram's spatial resolution which got missed by the reference segmentation workflow. This result can be ascribed to the stronger and negative influence of partial volume effects on the reference segmentation workflow while the registration + subtraction one is more "immune" to them. The latter feature intrinsically stems from the impossibility for the registration to deform the $\left\{\tilde{I}(\vec{x}_j, t_i)\right\}_{j=1,\ldots,N}$, $\forall\, i = 1, \ldots, 11$, as such to "close" the ASR cracks, since they are features which exist in $\left\{I(\vec{x}_j, t_i)\right\}_{j=1,\ldots,N}$ but not in $\left\{I(\vec{x}_j, t_0)\right\}_{j=1,\ldots,N}$ and every registration we performed was based only upon the voxel values, as mentioned before. Essentially, an unavoidable error for the type of image registration used could be exploited in this work to improve the segmentation results, in terms of crack volume fraction actually segmented. This

is a feature of image registration already exploited and proposed by Hild *et al.* for locating crack regions in tomograms of concrete specimens undergoing drying shrinkage even when such cracks were not completely resolved at any point in the tomogram time series [26].

Overall, the TS-based segmentation workflow for ASR-generated empty cracks allowed reducing false positive segmentation results due to partial volume effects and increasing the crack volume segmented.

S3.4 ASR products segmentation

The ASR products were segmented by subtracting the reference tomogram, $\{I(\vec{x}_j, t_0)\}_{j=1,\dots,N}$, from each B-spline registered tomogram, $\{\tilde{I}(\vec{x}_j, t_i)\}_{j=1,\dots,N}$, $\forall\, i = 1, \dots, 11$, the resulting tomogram having large and positive voxel values only where the products appeared between the times t_0 and t_i, given that the products provided their voxels extremely high values compared to voxels where most of the other material phases were contained. It was thus possible to choose a range of voxel values (thresholding) to select the products' voxels in such difference tomogram.

In order to further distinguish between products in cracks from those in other types of pores, e.g., air voids, the same type of sphericity-based filter described in Section S3.3 was used. Clusters of products' voxels with sphericity SD (see Eq. (ES5) above) smaller than 0.4 were classified as belonging to cracks, while those with SD larger than 0.4 were classified as belonging to other types of pores. Thus two disjoint binary tomograms were created, called $\{\tilde{I}^B_{ASR\ prod.-\ crack}(\vec{x}_j, t_i)\}_{j=1,\dots,N}$ and $\{\tilde{I}^B_{ASR\ prod.-\ void}(\vec{x}_j, t_i)\}_{j=1,\dots,N}$, $\forall\, i = 1, \dots, 11$, respectively.

The union, by a Boolean OR operator, of $\{\tilde{I}^B_{ASR\ prod.-\ crack}(\vec{x}_j, t_i)\}_{j=1,\dots,N}$ and $\{\tilde{I}^B_{ASR\ crack}(\vec{x}_j, t_i)\}_{j=1,\dots,N}$ led to the creation of a new binary tomogram, called $\{\tilde{I}^B_{ASR\ crack-tot}(\vec{x}_j, t_i)\}_{j=1,\dots,N}$, $\forall\, i = 1, \dots, 11$, classifying voxels exhibiting changes to ASR, in comparison to the reference tomogram at t_0. The respective change was due to the appearance of a crack, either containing products with high Cs concentration or no products or with low Cs concentration.

S3.5 Crack network: quantitative characterizations

Shape tensor analysis

Each binary tomogram of cracks, with or without ASR products and ASR-induced or not, $\{\tilde{I}^B_{ASR\ crack-tot}(\vec{x}_j, t_i)\}_{j=1,\dots,N}$, $\forall\, i = 1, \dots, 11$, and $\{I^B_{crack}(\vec{x}_j, t_0)\}_{j=1,\dots,N}$, was first of all subjected to labelling: each set of interconnected, segmented voxels (clusters) was identified and assigned a digital label to identify it as a distinct 3D object. Each cluster was thus treated as a distinct crack (or

"branch" of the crack network). Thus, each of those binary tomograms provided a statistical *ensemble* of crack network branches at a given time point in the series, including the reference time t_0. The labelling was performed with the module "Label Analysis" of the Avizo 3D software.

The same module of Avizo 3D was used to compute, for each distinct labelled crack, its shape tensor $\boldsymbol{G}$. The shape tensor $\boldsymbol{G}$ of a geometrical, 3D object is an analogue of the moment of inertia tensor of a physical body. Its elements are defined as

$$G_{ij} \equiv \int_{\Omega} \left(x_i - x_{i,CM}\right)\left(x_j - x_{j,CM}\right) d\vec{x}, \ \forall\, i,j = 1,2,3 \qquad \text{(ES6)}$$

where Ω means the 3D region occupied by the branch as a 3D object, $\vec{x}_{CM} \equiv \frac{1}{V_\Omega}\int_\Omega \vec{x} d\vec{x}$ is the branch's center-of-mass (CM) position vector, V_Ω means the volume of the branch and the indexes i and j just enumerates the three Cartesian components of a position vector inside Ω. In Avizo 3D, $\boldsymbol{G}$ is also called as "variance-covariance matrix" because it has the form of the covariance matrix of a random vector, being it in this case the position vector for the points inside Ω. The same software module computed the *eigen*values $\lambda_1 \geq \lambda_2 \geq \lambda_3$ and the respective *eigen*vectors, $(\hat{u}_1; \hat{u}_2; \hat{u}_3)$ of $\boldsymbol{G}$. The *eigen*vectors' directions indicate the principal axes (called in short "*eigen*directions" in what follows) of the branch. The *eigen*direction associated with the largest *eigen*value is the direction along which the branch is the most elongated.

A parallelepiped with sides oriented along the three *eigen*directions and circumscribing the object (called "bounding box" in the following) allows characterizing its characteristic sizes, shape and orientation in space [27]–[31]. We used the three lateral sizes of such bounding box as definitions of length (L), height (or equivalently called width, H) and thickness (T) of the object, corresponding to the largest, mid and smallest size of the parallelepiped box, respectively ($L \geq H \geq T$) [29]. We computed L, H and T by using two feature variables associated with the direction of each *eigen*vector and computed by the same Avizo 3D module. They are called in such module "ExtentMax$i$" and "ExtentMin$i$", where $i = 1,2,3$ enumerates the *eigen*vectors. ExtentMax$i$ is always a positive number while ExtentMin$i$ is always negative. ExtentMax$i$ is computed as the distance between the CM of the branch and the plane tangent to the branch's boundary surface and orthogonal to the *eigen*vector $\hat{u}_i$, on the side pointed at by $\hat{u}_i$. ExtentMin$i$ is computed similarly as ExtentMax$i$ but for the plane also tangent to the branch's boundary surface, also orthogonal to the $\hat{u}_i$ but on the side in the opposite direction of $\hat{u}_i$, thus being assigned a negative value. We then computed the feature variable ExtentTot$i$ = ExtentMax$i$ – ExtentMin$i$, which is equal to the size of the bounding box.

We defined the three "crack boundary box size measures" as the following:

- length L = ExtentTot1
- height (or width) H = ExtentTot2
- thickness T = ExtentTot3.

We note as L, H and T correspond to the Feret (or caliper) diameters along the directions of $\hat{u}_1$, $\hat{u}_2$ and $\hat{u}_3$, respectively. L and T are not necessarily equal to the maximum and minimum Feret diameter of the branch, respectively, although they may be close to, depending upon the crack's surface shape.

Ratios of the *eigen*values of $\boldsymbol{G}$ allow a coarse classification of shape, even when the 3D object is very irregularly shaped. We used two such useful variables (also called shape anisotropy degrees [32]):

$$E = 1 - \frac{\lambda_3}{\lambda_1} \quad \text{(ES7)}$$

and

$$F = 1 - \frac{\lambda_3}{\lambda_2} \quad \text{(ES8)}$$

where $\lambda_1 \geq \lambda_2 \geq \lambda_3$ are the three eigenvalues of $\boldsymbol{G}$. E is an **elongation** parameter while F is a **flatness** one. We then mapped each independent branch to a point in the $(E; F)$ 2D plane. The analysis of the distribution of $(E; F)$ points allowed comparing crack shapes across specimens.

Finally, we used the distribution of the direction of the *eigen*vector of $\boldsymbol{G}$ associated with the first *eigen*value, $\hat{u}_1$, to assess the crack orientations. The direction of $\hat{u}_1$ was expressed in spherical coordinates, $(\varphi_1; \theta_1)$, and mapped on one hemisphere of a 3D sphere of radius equal to one for better visualization of the orientation distribution.

Local thickness analysis

We computed, at any time point, the local thickness scalar field, $T_{local}(\vec{x})$, at any position $\vec{x}$ inside the region Ω of any segmented crack network branch by using the binary tomograms $\left\{\tilde{I}^{B}_{ASR\ crack-tot}(\vec{x}_j, t_i)\right\}_{j=1,\dots,N}$, $\forall\, i = 1, \dots, 11$.

The mathematical definition of $T_{local}(\vec{x})$ is the one proposed by Hildebrand and Rüegsegger [33]. $T_{local}(\vec{x})$ is there defined as the diameter of the largest sphere which (1) contains $\vec{x}$ and (2) is contained within the region Ω. The actual computation of $T_{local}(\vec{x})$ was performed with Avizo 3D's module "Thickness Map", with its option "Boundary Voxels" set to "included", by which Hildebrand and Rüegsegger's algorithm was implemented with additional "inclusion" of the voxels belonging to the boundary of Ω.

S3.6 ASR-induced deformations: global and local analysis by 3D image registration

Global analysis

Insets (a) and (b) in Figure S16 show cartoons illustrating how time-lapse measurements of size along the specimen's longitudinal direction ("length"), $L_Z(t_i), \forall\, i = 0, 1, \dots, T$, were performed both on the specimens undergoing time-lapse XMT and for three additional ones. A mechanical displacement gauge (by Mitutoyo) with accuracy of 1 μm was used. An Invar prism with nominal length of 160 mm

was used for calibrating the gauge at each t_i. Invar is a Ni-Fe alloy with a considerably low thermal expansion coefficient. Care was taken to locate the specimen on the gauge such that, at each t_i, its pins were always positioned approximately the same, at the center of the specimen's ($X-Y$) lateral faces (Figure S16 (b)). The whole specimen-scale relative change in length, $\frac{\Delta L_Z}{L_Z}(t_i)$, $\forall\, i = 1, \dots, 11$, was then computed to assess the specimen's global deformation (see Figure 1 (a) in the article for the P data and Figure S17 (a) below for the U ones).

In order to assess the corresponding relative length change for the portion of the specimen which was tomographed (also called volume of interest, VOI, in Figure S16 (e)), we exploited the results of the global affine registration (Section S3.3 above).

Since the global affine registration model is based upon the assumption of a linear mapping vector field (see Eq. ES1 above), the corresponding displacement vector field, $\vec{u}_{AFF}(\vec{x})$, is also linearly dependent on $\vec{x}$,

$$\vec{u}_{AFF}(\vec{x}, t_i) \equiv \vec{x}'(t_i) - \vec{x} = \vec{T}_{AFF}(\vec{x}, t_i) - \vec{x} = (\boldsymbol{S}(t_i) \cdot \boldsymbol{L}(t_i) \cdot \boldsymbol{R}(t_i) - \mathbb{I}_{\mathbf{3}}) \cdot \vec{x} + \vec{t}(t_i), \forall\, i = 1, \dots, 11 \quad \text{(ES9)}$$

where $\mathbb{I}_{\mathbf{3}}$ is the 3×3 identity matrix. Inset (c) in Figure S16 shows the plot of $u_{Z,AFF}(\vec{x}, t_i)$ inside the tomographed volume of a specimen at a given time point t_i, with $i \neq 0$, showing how it depends mainly on z. Inset (f) in Figure S16 shows with two distinct vertical axes the changes of two features. The red line in the plot is associated with the left vertical axis. It shows on the horizontal axis the values of $u_{Z,AFF}(\vec{x}, t_i)$ averaged over various 2D ROIs, each located on a slice orthogonal to the Z-axis (Figure S16 (d)) and centered in the center of the slice itself, as a function of the slice's Z-position (shown on the left vertical axis). Such a plot was repeated for a distinct size of the 2D ROIs (from 0.175×0.175 mm^2 to 10.5×10.5 mm^2). The results were independent from the ROI size. The vertical axis on the right hand-side shows all those $X-Y$ ROI size values. At each position along such right vertical axis, the corresponding minimum and maximum values of the averaged $u_{Z,AFF}(\vec{x}, t_i)$ are plotted with circular markers with distinct colors for the distinct ROI size. Such double vertical axes plot shows that (1) $u_{Z,AFF}(\vec{x})$ clearly varied linearly with z, (2) the X-Y-averaged $u_{Z,AFF}(\vec{x})$ is independent of the $X-Y$ ROI size and (3) the tomographed portion of the specimen, centered about its mid, got deformed along the specimen's longitudinal direction from the center off (negative displacement values below the center, positive ones above).

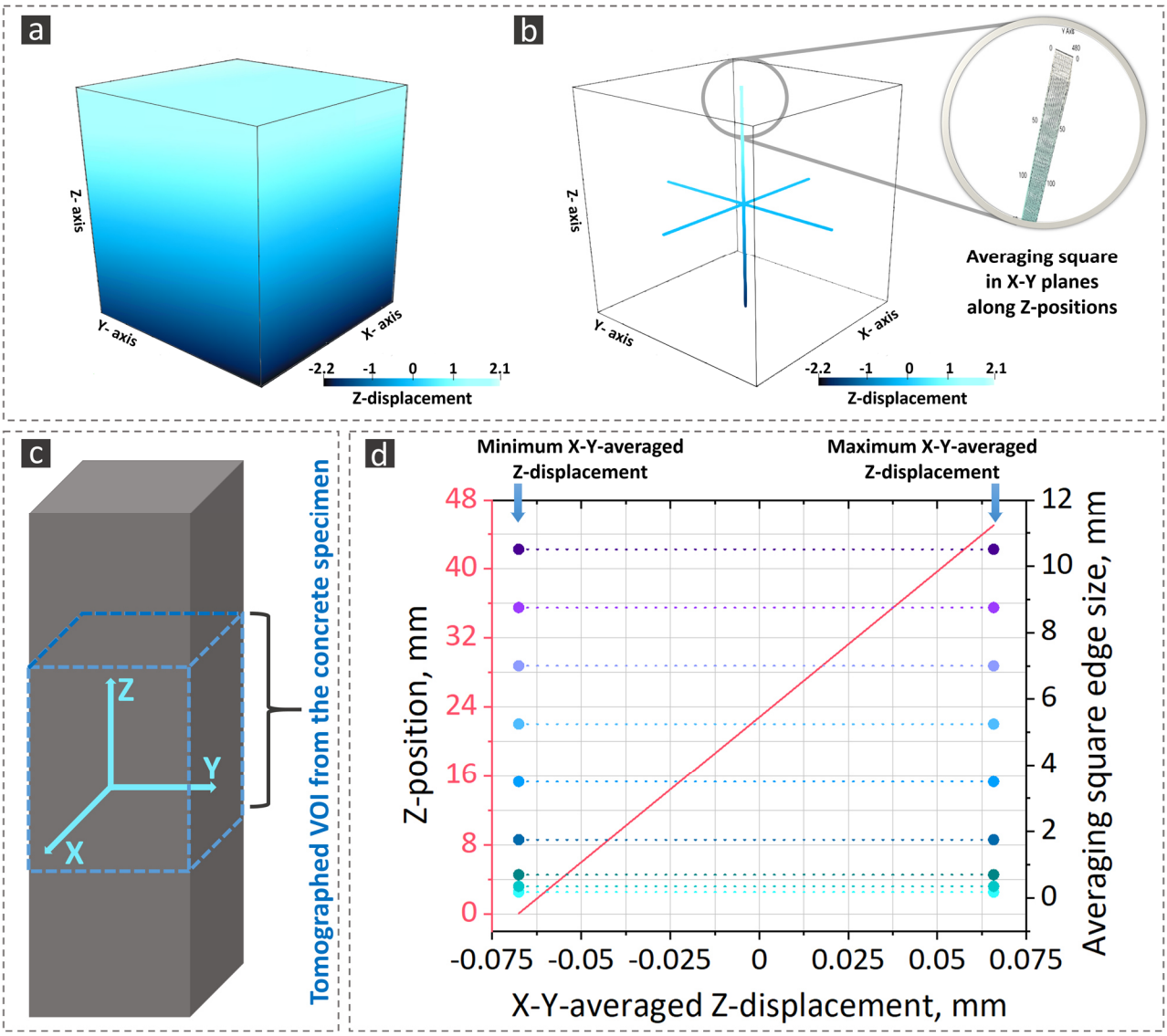

Figure S 16. Measurement results for the relative length change of the specimens, both using a conventional mechanical gauge and based upon the 3D, global affine registration of the tomograms. (a) and (b) Schematic illustration of the gauge used for measuring experimentally the length change (dimensional change along the Z-axis) of the specimens. (c) Rendering of the Z-component of the displacement vector field associated with the global affine registration results, $u_{Z,AFF}(\vec{x}, t_i)$, for a specimen at a given time point t_i, with $i \neq 0$. The color scale is in units of number of voxels. The units for the axes of the Cartesian frame of reference are also number of voxels. (d) The $u_{AFF,Z}(\vec{x})$ inside a 3D ROI spanning the entire volume along the Z-axis, with size 0.2 × 0.2 mm^2 on the $X-Y$ slices and centered in the middle of each such slice. (e) Schematic illustration of the specimens used in this study and the axes of the Cartesian frame of reference. The indicative location of the volume investigated by XMT is also specified. (f) Horizontal axis: values of $u_{Z,AFF}(\vec{x}, t_i)$ averaged over various 2D ROIs of distinct sizes located on slices orthogonal to the Z-axis and centered in the center of the slice itself, as a function of their Z-position (left vertical axis). Vertical axis on the right: size of the 2D X-Y

ROIs over which $u_{Z,AFF}(\vec{x},t_i)$ was averaged. The red line refers to the left vertical axis. The colored, circular markers refer to the right vertical axis and show the minimum and maximum values of $u_{Z,AFF}(\vec{x},t_i)$ along the Z-axis, after averaging it over various 2D, rectangular ROIs. Circles of distinct colors show minimum and maximum values in correspondence of distinct ROI size.

We used the same procedure based upon the affine registration results to measure the dimensional changes of each tomographed volume at any time point along the X- and Y- axis. We computed the relative change of the size of the tomographed volume along the Z direction, $\frac{\Delta L_{AFF,Z}}{L_{AFF,Z}}(t_i)$, $\forall\, i = 1,\dots,11$, as the absolute value of the difference between the maximum and the minimum value of $u_{AFF,Z}(\vec{x})$ inside a 3D ROI spanning the entire volume along the Z-axis, with size 0.2 × 0.2 mm^2 on the $X-Y$ slices and centered in the middle of each such slice (Figure S16 (d)). The resulting $\frac{\Delta L_{AFF,Z}}{L_{AFF,Z}}(t_i)$, $\forall\, i = 1,\dots,11$, values, reported in Figure 1 of the article for the P specimens and in Figure S 17 for the U ones, were essentially independent from the $X-Y$ size of such 3D ROI, as shown in Figure S16 (f). Similar results were also obtained by computing $\frac{\Delta L_{AFF,Z}}{L_{AFF,Z}}(t_i)$ with a distinct approach, consisting first of averaging $u_{AFF,Z}(\vec{x})$ on 2D, centered ROIs located on $X-Y$ slices, then computing the minimum and maximum values of the resultant function of z over the whole range of Z slices and finally computing the absolute value of their difference.

Local analysis

We used the results of the non-affine registration to create 3D scalar fields providing information about the spatial distribution of ASR-induced deformations. One such scalar field is the Euclidean norm (i.e. magnitude) of the displacement vector field associated with the vector field of the non-affine mapping,

$$\|\vec{u}_{N-AFF}\|(\vec{x},t_i) \equiv \|\vec{x}'(t_i)-\vec{x}\| = \left\|\vec{T}_{N-AFF}(\vec{x},t_i)-\vec{x}\right\|, \forall\, i = 1,\dots,11 \qquad \text{(ES10)}.$$

It provides the spatial map of a sort-of "intensity" or "degree" of the local deformations.

The second scalar field is the determinant of the Jacobian matrix of the mapping vector field $\vec{T}_{N-AFF}(\vec{x},t_i)$, in short called the Jacobian of the mapping:

$$J_{\vec{T}_{N-AFF}}(\vec{x},t_i) \equiv det\left(\frac{\partial \vec{T}_{N-AFF}}{\partial \vec{x}}\right)(\vec{x},t_i) \qquad \text{(ES11)},$$

where

$$\frac{\partial \vec{T}_{N-AFF}}{\partial \vec{x}} \equiv \begin{pmatrix} \frac{\partial T_{N-AFF,1}}{\partial x_1} & \frac{\partial T_{N-AFF,1}}{\partial x_2} & \frac{\partial T_{N-AFF,1}}{\partial x_3} \\ \frac{\partial T_{N-AFF,2}}{\partial x_1} & \frac{\partial T_{N-AFF,2}}{\partial x_2} & \frac{\partial T_{N-AFF,2}}{\partial x_3} \\ \frac{\partial T_{N-AFF,3}}{\partial x_1} & \frac{\partial T_{N-AFF,3}}{\partial x_2} & \frac{\partial T_{N-AFF,3}}{\partial x_3} \end{pmatrix} \qquad \text{(ES12)}$$

is the Jacobian matrix of the mapping vector field $\vec{T}_{N-AFF}(\vec{x}, t_i)$, $x_1 = x$, $x_2 = y$ and $x_3 = z$.

We remind that (see [34])

$$d\vec{x}' = \frac{\partial \vec{T}_{N-AFF}}{\partial \vec{x}} \cdot d\vec{x} \quad \text{(ES13)}$$

such that

$$dV_{\vec{x}'} = J_{\vec{T}_{N-AFF}}(\vec{x}, t_i) \cdot dV_{\vec{x}} \quad \text{(ES14)},$$

i.e., the Jacobian of the non-affine mapping provides a spatial map of the ratio between the local volume at time t_i and the local volume at time t_0 [34]. Values larger than 1 indicate a local volumetric expansion while values smaller than 1 a local contraction.

Both $\vec{u}_{AFF}(\vec{x}, t_i)$ and $\frac{\partial \vec{T}_{N-AFF}}{\partial \vec{x}}(\vec{x}, t_i)$ were computed as outputs of the respective registration workflows implemented by the use of the SimpleElastix image registration library.

S4. Effect of the alkali-doping on ASR

The preliminary ASR experimental campaign, based upon the "concrete prism test" and described in Section S2.2 above, included time-lapse measurements of relative changes, compared with the start, of specimen longitudinal size and of specimen mass [35]. All types of alkalis boosted up the reference concrete type's normal ASR expansion. However, the extent of such effect varied with the type of alkalis used. For instance, Rb and K increased the expansion the most. Na enhanced it slightly less. Cs produced the least increase.

S5. Dimensional and mass changes during ASR acceleration

S5.1 Dimensional changes

The main difference in the expansion behaviour of the specimens cast with the two aggregate types was quantitative: the P specimens expanded more slowly than the U ones. Compare the results in Figure 1 with those in Figure S 17. This result was independent of Cs-doping.

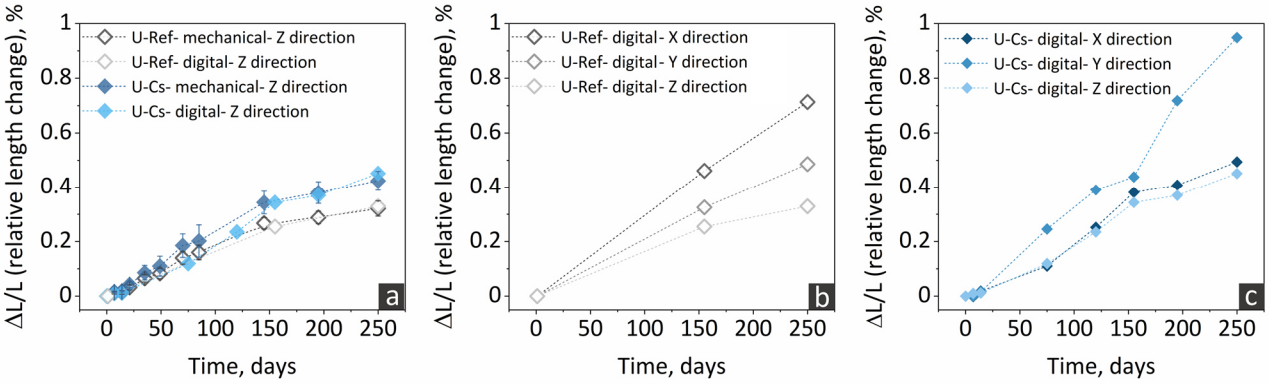

Figure S 17. *Similar plot as in Figure 1 of the article but for the U-Ref and U-Cs specimens.*

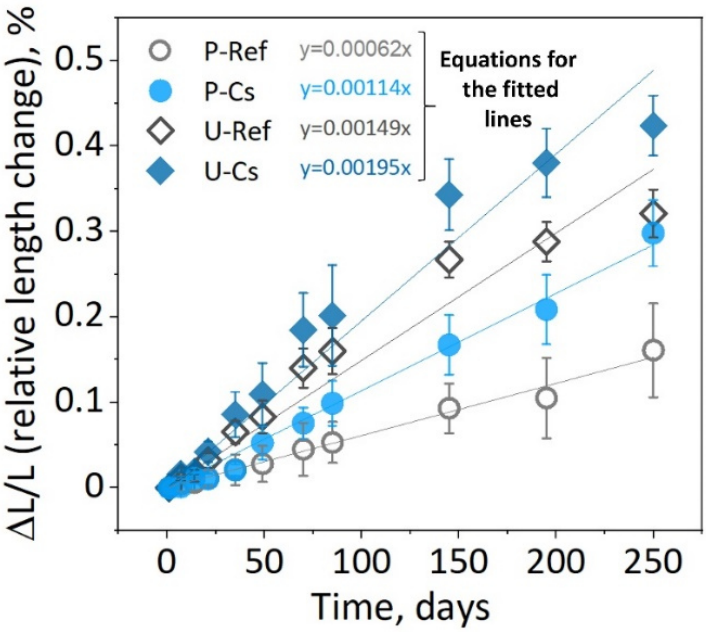

Figure S 18. Linear regression analysis (not weighted by error bars) of the experimentally measured relative length change of the Cs-doped and reference specimens. It was performed to estimate and compare overall approximate rates of expansion. The coefficient of determination, R^2, values are 0.994, 0.994, 0.974 and 0.977, for the P-Ref, P-Cs, U-ref and U-Cs specimens, respectively. The markers correspond to the average values of the relative length change of six distinct specimens, at each time point. The error bar of each marker corresponds to the standard deviation over those six distinct values.

Comparison of experimentally measured and global affine registration-based estimates of length changes

In order to compare the experimentally measured relative length change values, $\frac{\Delta L_Z}{L_Z}$, with the respective value obtained by the global affine registration procedure described in Section S3.6, $\frac{\Delta L_{AFF,Z}}{L_{AFF,Z}}$, we made the following operative assumptions:

1. the six $\frac{\Delta L_Z}{L_Z}$ values, each from a distinct full specimen, were samples from a random variable with Gaussian distribution with mean value estimated by the average of the six samples, $\langle\frac{\Delta L_Z}{L_Z}\rangle$ (reported in Table T2 below), and standard deviation approximated by the empirical standard deviation of the six samples, $\sigma_{\frac{\Delta L_Z}{L_Z}}$ (also reported in Table T2 below); randomness in $\frac{\Delta L_Z}{L_Z}$ values stemmed not only from measurement errors but also from material heterogeneity;

2. if the tomographed volume, belonging to one of those six specimens and being slightly smaller than 30% of the total specimen volume, was representative enough of the whole specimen's volume, in terms of ASR-induced expansion, then the $\frac{\Delta L_{AFF,Z}}{L_{AFF,Z}}$ value (reported in Table T3 below), obtained from its affine registration to the first tomogram of the same volume in the time series, at the beginning of the ASR acceleration, should be just another sample of the same random variable as at point 1.

Under the assumption at point 2 above, a $\frac{\Delta L_{AFF,Z}}{L_{AFF,Z}}$ value should differ from a $\frac{\Delta L_Z}{L_Z}$ one just by randomness (null hypothesis) with Gaussian statistics characterized by $\langle\frac{\Delta L_Z}{L_Z}\rangle$ and $\sigma_{\frac{\Delta L_Z}{L_Z}}$. As a consequence of such null hypothesis, the probability of measuring, by the affine registration of tomograms with such size, $\frac{\Delta L_{AFF,Z}}{L_{AFF,Z}}$ values differing in absolute value from $\langle\frac{\Delta L_Z}{L_Z}\rangle$ more than 1.96 times $\sigma_{\frac{\Delta L_Z}{L_Z}}$ should be smaller than 5%. Table T4 reports, for each specimen type, the absolute value of the difference between $\langle\frac{\Delta L_Z}{L_Z}\rangle$ and $\frac{\Delta L_{AFF,Z}}{L_{AFF,Z}}$, normalized by $\sigma_{\frac{\Delta L_Z}{L_Z}}$. Such values were computed either at identical or close enough times when the two variables, $\frac{\Delta L_Z}{L_Z}$ and $\frac{\Delta L_{AFF,Z}}{L_{AFF,Z}}$, were measured. A value in Table T4 smaller than 1.96 corresponds to a probability smaller than 5% that the difference in the relative length change estimates was only due to randomness. In such a case, the null hypothesis can be rejected with 95% confidence, which we assume as our confidence level. When that happens, it cannot be stated that the tomographed volume expanded in a way representative of the expansion of the whole specimen volume.

Table T2: time series of relative length change values obtained by experimental measurements with the mechanical gauge, $\frac{\Delta L_Z}{L_Z}$. For each specimen type, only the average (Ave.) and the standard deviation (Std.) values computed from the six specimens are reported. Such time series are plotted in Figure 1(a) of the article and in Figs. S 17 and S 18 above.

	U-Ref		**P-Ref**		**U-Cs**		**P-Cs**	
Time [days]	**Ave. [%]**	**Std. [%]**	**Ave. [%]**	**Std. [%]**	**Ave. [%]**	**Std. [%]**	**Ave. [%]**	**Std. [%]**
1	0	0	0	0	0	0	0	0
7	0.012	0.004	0.004	0.008	0.016	0.003	0.001	0.006
14	0.014	0.007	0.006	0.009	0.018	0.002	0.011	0.006
21	0.032	0.009	0.011	0.009	0.042	0.012	0.011	0.006
35	0.065	0.013	0.021	0.018	0.086	0.026	0.021	0.007
49	0.083	0.019	0.028	0.021	0.110	0.037	0.053	0.019
70	0.14	0.023	0.045	0.031	0.185	0.043	0.076	0.018
85	0.16	0.027	0.053	0.024	0.202	0.059	0.099	0.026
145	0.267	0.021	0.093	0.029	0.343	0.042	0.168	0.035
195	0.288	0.023	0.105	0.047	0.380	0.040	0.209	0.041
250	0.321	0.028	0.161	0.055	0.424	0.035	0.298	0.039

Table T3: time series of relative length change values obtained from the global affine registration of the tomograms, $\frac{\Delta L_{AFF,Z}}{L_{AFF,Z}}$. For each specimen type, only one value is available because only one of the three tomographed specimens was analyzed. Such time series are plotted in Figure 1 of the article and in Figs. S 17 above.

U-Ref		**P-Ref**		**U-Cs**		**P-Cs**	
Time [days]	**Value [%]**	**Time [days]**	**Value [%]**	**Time [days]**	**Value [%]**	**Time [days]**	**Value [%]**
1	0	1	0	1	0	1	0
						3	0.001
				7	0.010	7	0.018
				14	0.012	14	0.021
						21	0.03
						30	0.031
						50	0.048
				75	0.119	65	0.067
				120	0.235	85	0.13
155	0.254	155	0.069	155	0.344	145	0.2
				195	0.369	195	0.24
250	0.329	250	0.199	250	0.451	250	0.285

Table T4: absolute value of the difference between the global affine registration-based relative length change of the tomographed volume and the average value of the experimentally measured relative length changes, normalized by the standard deviation of the latter, $\frac{\left|\frac{\Delta L_{AFF,Z}}{L_{AFF,Z}} - \langle\frac{\Delta L_Z}{L_Z}\rangle\right|}{\sigma_{\frac{\Delta L_Z}{L_Z}}}$*, where* $\langle\frac{\Delta L_Z}{L_Z}\rangle$ *means the average of the six values of* $\frac{\Delta L_Z}{L_Z}$ *while* $\sigma_{\frac{\Delta L_Z}{L_Z}}$ *is the empirical standard deviation of such six values.*

Time [days]	U-Ref	P-Ref	U-Cs	P-Cs
7			1.89	2.96
14			2.80	1.53
21				3.09
50				0.24
85				1.18
150	0.60	0.83	0.01	0.93
195			0.27	0.77
250	0.30	0.69	0.77	0.34

S5.2 Mass changes

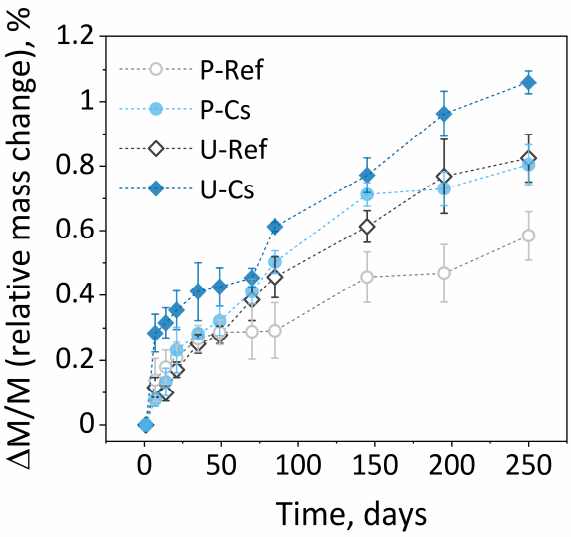

Figure S 19. The relative mass changes of the Cs-doped specimens and their corresponding reference specimens during the ASR acceleration. For each mix type, the measurements were performed on the same exact six specimens on which the length was also measured, including among

them the specimen being the subject of the tomography analysis. Each marker shows the average of the six values. Each error bars shows their standard deviation.

S6. Evolution of the mechanical properties for the specimens cast with Uri aggregates

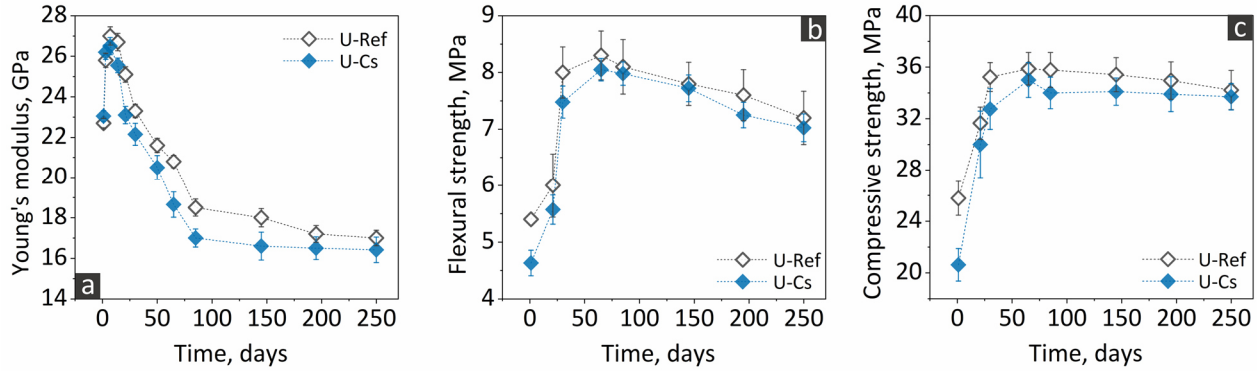

Figure S 20. The time series of the (a) quasi-static Young's modulus, (b) the flexural and (c) the compressive strength of specimens with and without Cs addition, cast with U aggregates.

S7. Qualitative analysis of ASR cracking by time-lapse tomography.

Reference specimens

Figure S21 and Figure S22 showcase the crack network segmentation results for the reference specimens. They serve the double goal of (1) showing the quality of the segmentation results and of (2) illustrating some typical features of the cracking evolution in such specimens. For each aggregate type, a small ROI of the respective tomograms at three time points was selected as representative, because containing several evolving cracks. At times 155 and 250 days, the tomograms after the final non-affine registration were used. This choice allowed easier analysis of the temporal evolution, since the main difference between the tomograms is due to the evolving cracks.

The first row in each figure shows, at any time point, a specific 2D digital cross-section ($X-Y$ slice) from the chosen ROI. The position of the cross-section is the same at every time point. The second row shows the same slices as in the first one. However, overlapped on top of them and rendered in solid, blue/purple color, are the corresponding slices from the respective crack network binary tomograms. The overlapping helps with assessing the quality of the segmentation. It provides a qualitative idea about whether the majority of the cracks are segmented, which ones are typically not and to which degree single cracks are segmented (in terms of length and width). The segmented, full crack

network is shown in the third row as a 3D solid volume rendering, for any time point. The parallelepiped box containing it indicates the tomographed volume of the specimen. Note that the point of view of the rendering of the 3D scene is the same at any time point, such that it is easier to track the cracking and to compare the crack network at successive time points. The last row shows the rendered crack network at the last time point (250 days) overlapped on top of the 3D rendering of the respective, non-affine registered tomogram, made semi-transparent. Such rendering is shown twice, from two distinct points of view.

On the one hand, the time series of a single slice shows that several parts of the crack network evolved both in length and in width and, in several cases, starting from cracks already existing at 1 day, i.e., before the ASR acceleration started. On the other hand, the time series of 3D renderings of the full crack network shows that the cracks were rather homogeneously distributed inside the tomographed volume. The latter is a feature to be expected since (1) ASR cracking mainly starts inside aggregates and (2) the specimens had stress-free boundary conditions. The 3D rendering of the segmented crack network at time = 250 days also shows that the chosen U-Ref specimen clearly achieved a larger crack volume fraction (total crack volume divided by tomogram volume) than the chosen P-Ref one. Such result was confirmed for all the specimens by the quantitative analysis of their crack networks (see Figure 8 in the article and Figure S 30).

More details of the ASR cracks are visible in Figure S 23, which shows zoom-in ROIs from the $X-Y$ slices shown in insets (a) – (c) of Figures S 21 and S 22. Such figure is organized exactly as insets (a) – (f) of Figures S 21 and S 22. In addition to provide a better view of some details of the cracks, the quality level of the crack segmentation can be better appreciated in Figure S 23 (d) – (f) and (j) to (l), for the P-Ref and U-ref specimens respectively.

Examples of cracks which appeared to be filled with ASR products are pointed at in Figure S 21 (b), Figure S 22 (b) and Figure S 23 (b) and (h). These examples show the very small X-ray attenuation contrast between the natural products and the other material phases of the aggregate and in the cement paste. Such small contrast and the limited tomographic spatial resolution (in comparison to the thinnest cracks at early and intermediate times) made it challenging, even for the human eye, to detect the products inside the cracks, let alone their systematic segmentation by algorithms.

Figure S 24 shows the binary tomograms of the segmented cracks at the three time points of Figures S 21 and S 22 and for the same specimens. Such binary tomograms are rendered with distinct colors and superimposed on top of each other in the order 250, 150 and 1 days. Its insets (a) and (c) show 2D ROIs from a slice while (b) and (d) show the 3D rendering.

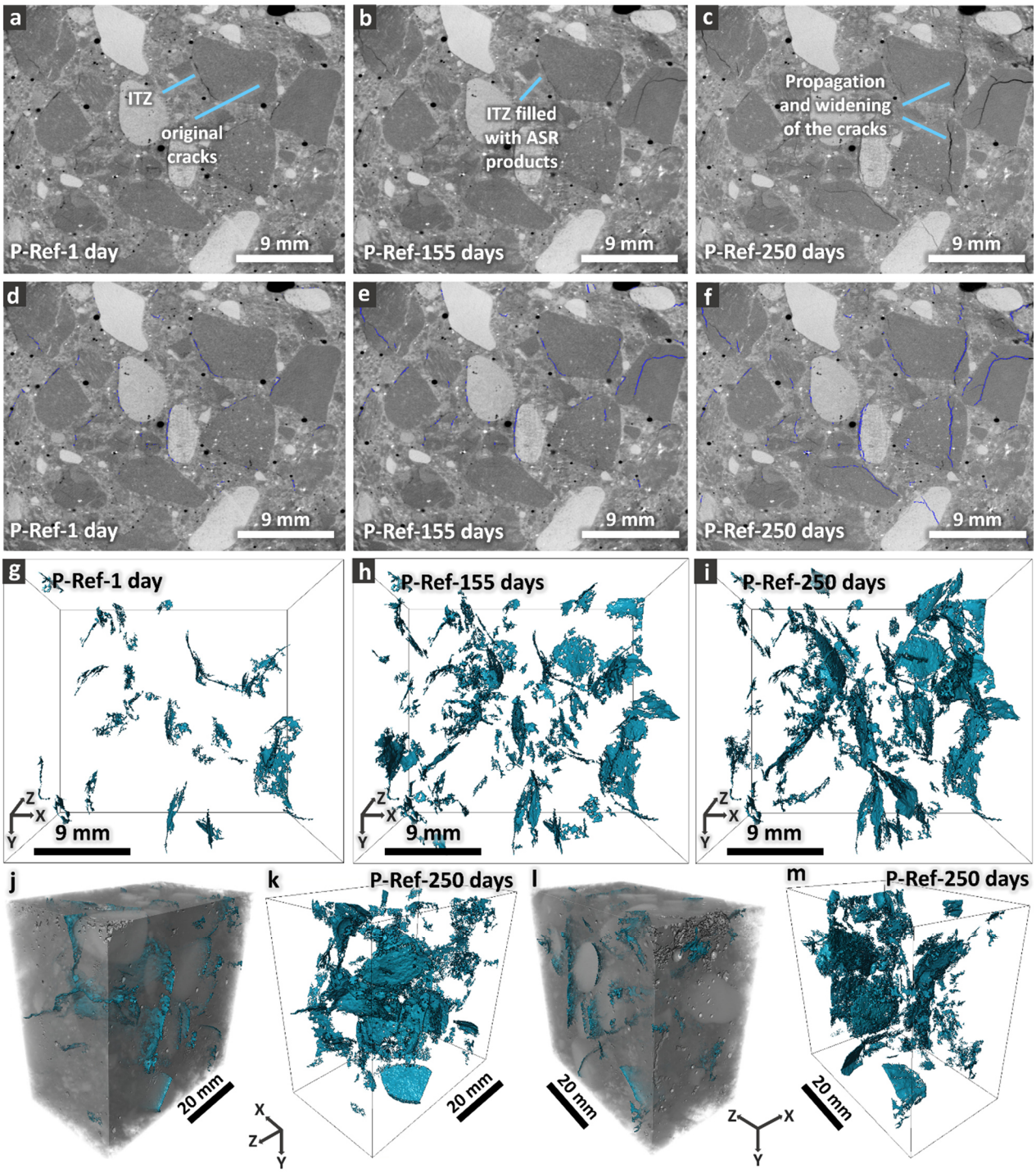

Figure S 21. Temporal evolution of the crack network in the P-Ref specimen. (a)-(c): 2D cross-section ($X-Y$ slice) from a small ROI of the tomogram at 1 day, 155 days and 250 days, respectively. The position of the slice and of the ROI is the same at any time point. The tomograms at 155 and 250 days are those obtained as output from the final non-affine registration. (d)-(f): the same slice as in (a)-(c) and, overlapped on top of it and in blue/purple color, the corresponding slice from the corresponding crack binary tomogram. (g)-(i): 3D rendering of the crack binary tomogram for the full tomographed volume of the specimen. (j) and (l): 3D rendering in semi-transparent grey

tones of the non-affine registered tomogram at time = 250 days and, overlapped on top of it, the correspondingly segmented crack network, also shown independently in (k) and (m), respectively. Two distinct points of views for rendering the 3D scene.

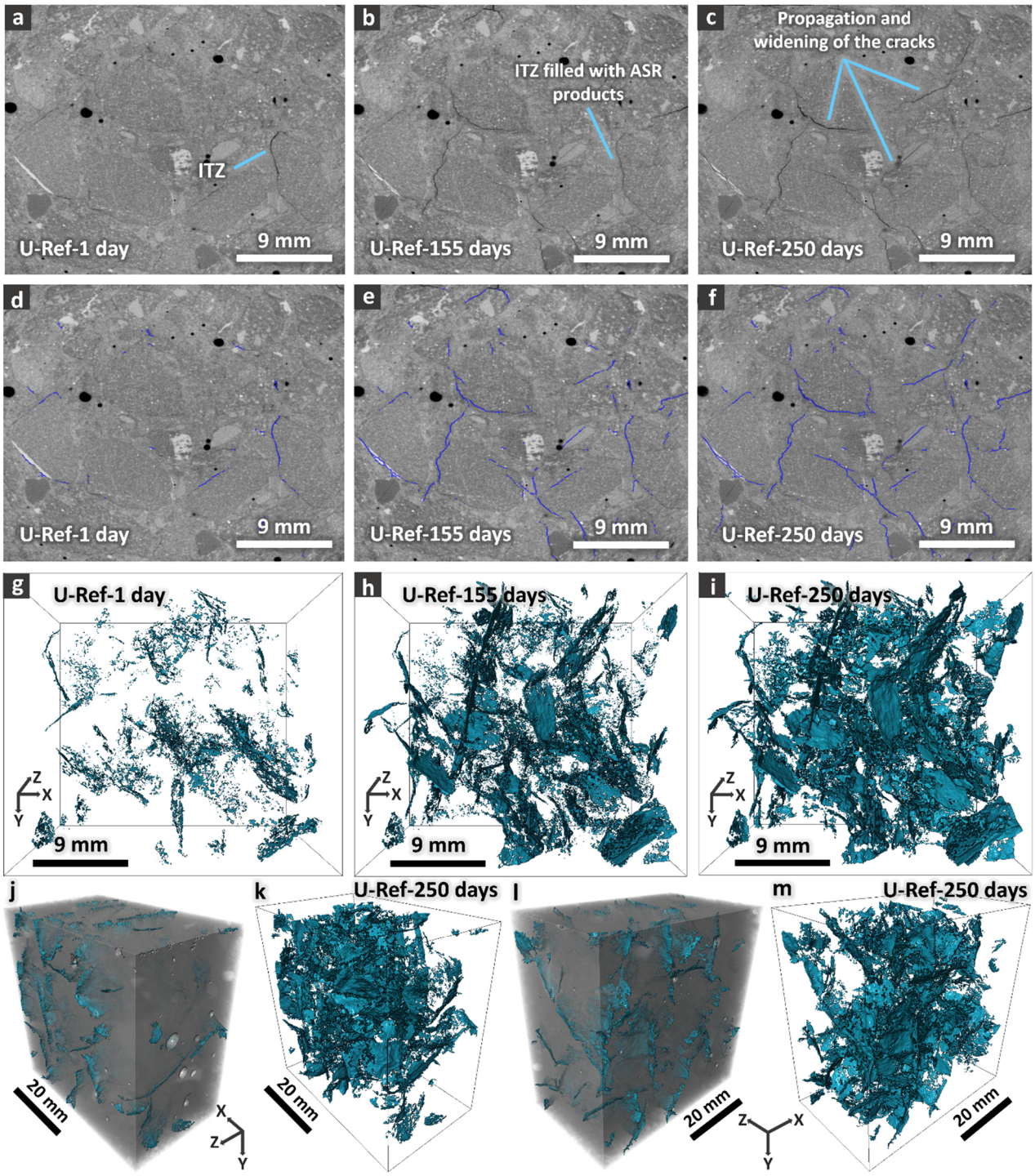

Figure S 22. Temporal evolution of the crack network in the U-Ref specimen. (a)-(c): 2D cross-section ($X-Y$ slice) from a small ROI of the tomogram at 1 day, 155 days and 250 days, respectively. The position of the slice and of the ROI is the same at any time point. The tomograms at 155 and 250 days are those obtained as output from the final non-affine registration. (d)-(f): the same

slice as in (a)-(c) and, overlapped on top of it and in blue/purple color, the corresponding slice from the corresponding crack binary tomogram. (g)-(i): 3D rendering of the crack binary tomogram for the full "tomographed" volume of the specimen. (j) and (l): 3D rendering in semi-transparent grey tones of the non-affine registered tomogram at time = 250 days and, overlapped on top of it, the correspondingly segmented crack network, also shown separately in (k) and (m), respectively. Two distinct points of views for rendering the 3D scene.

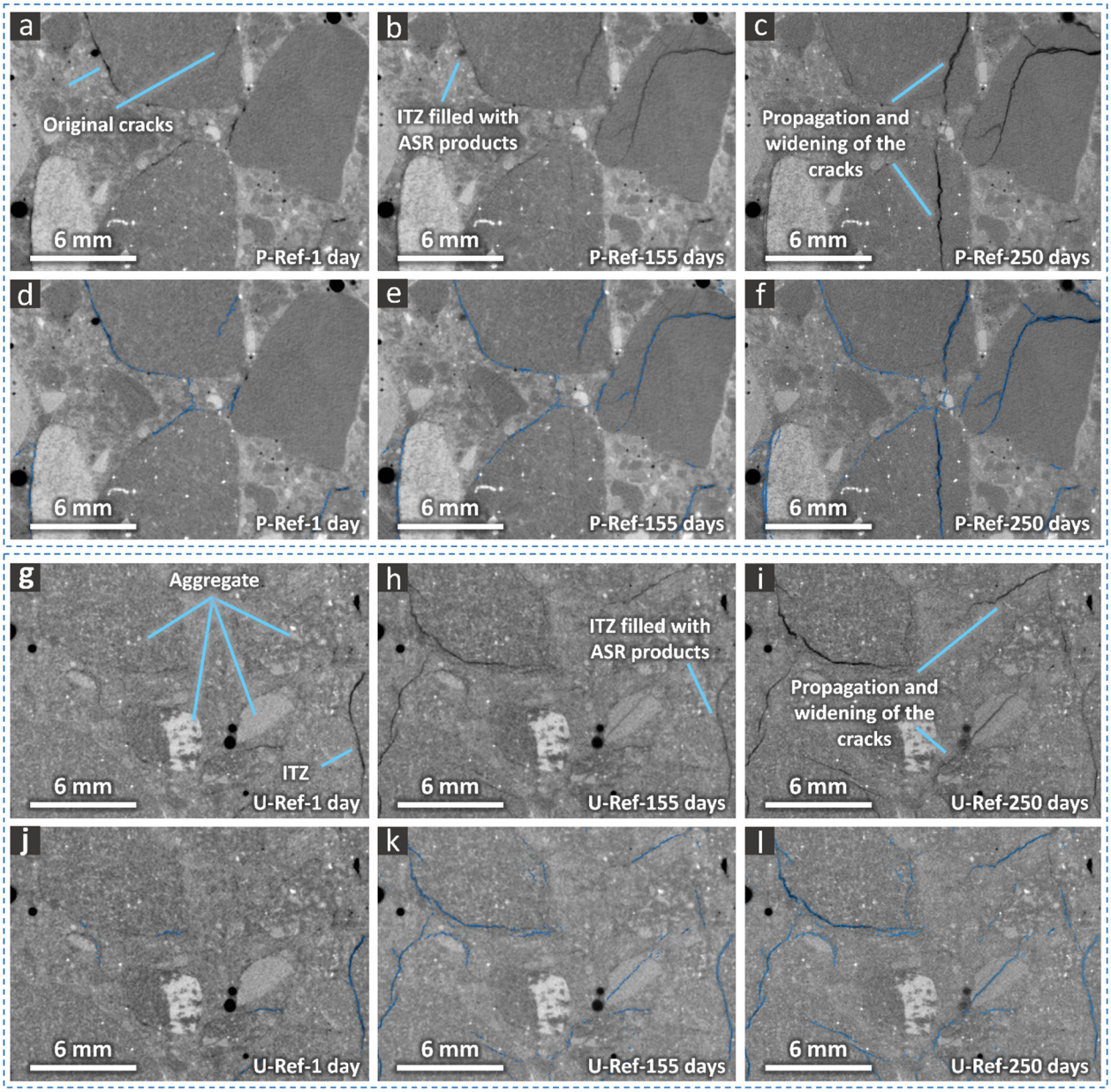

Figure S 23. Smaller region of interest (ROI) from the slices shown in Figure S21 and Figure S22 in insets (a)-(f), summarized in a single image to facilitate the visibility and the comparison.

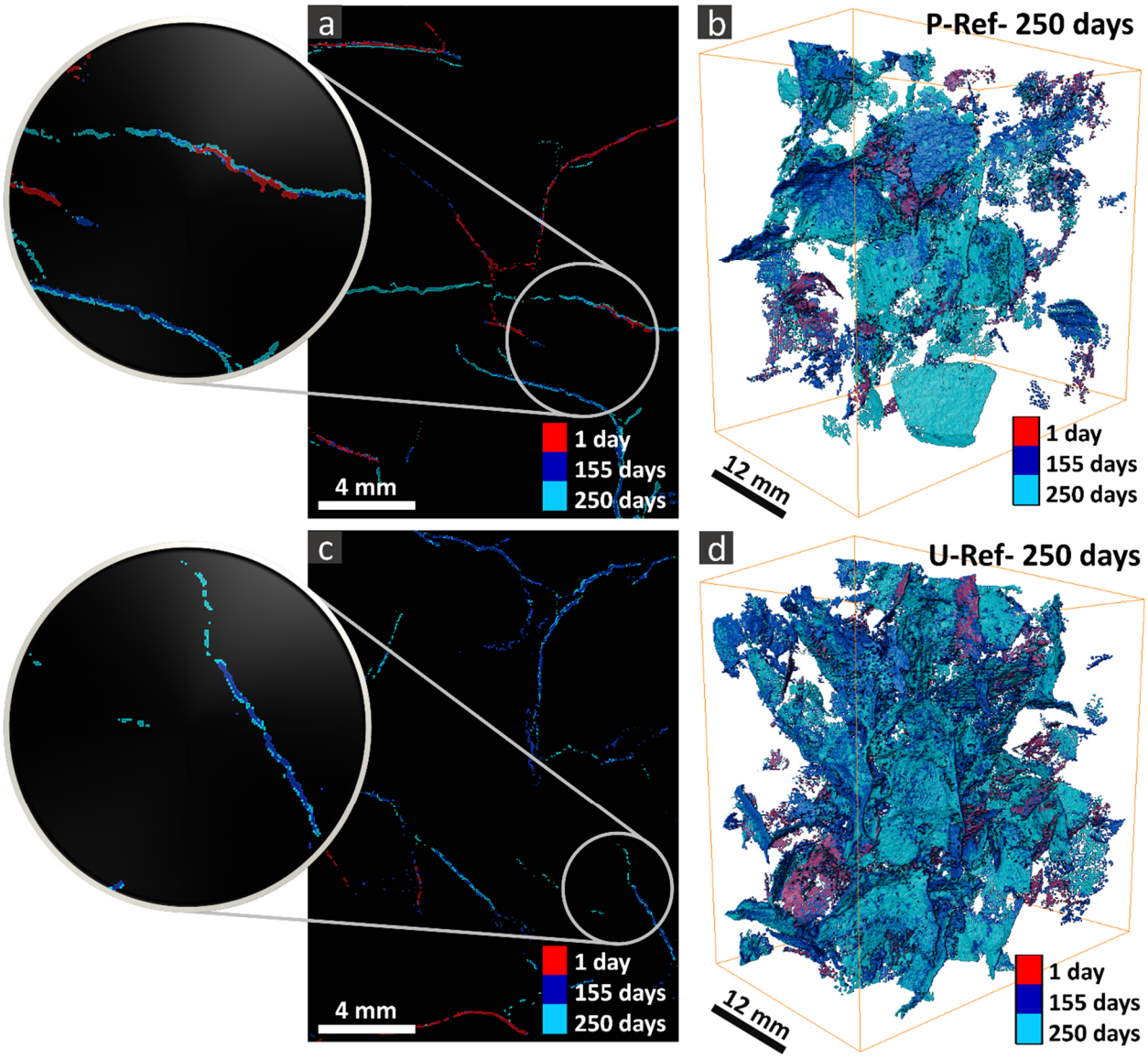

Figure S 24. Visualization of the time evolution of crack networks. Examples from the reference specimens. Top row: P-Ref specimen. Bottom row: U-Ref specimen. Left column: in each row, 2D digital cross-section taken from a ROI fixed at the three distinct time points (color coded). The binary tomograms were overlapped in order of decreasing time. Right column: 3D rendering of the overlapped crack network binary tomograms of the two reference specimens, at the same three time points as in insets (a) and (c), respectively.

S8. Qualitative analysis of ASR cracking by time-lapse tomography.

Cs-doped specimens

P-Cs specimen

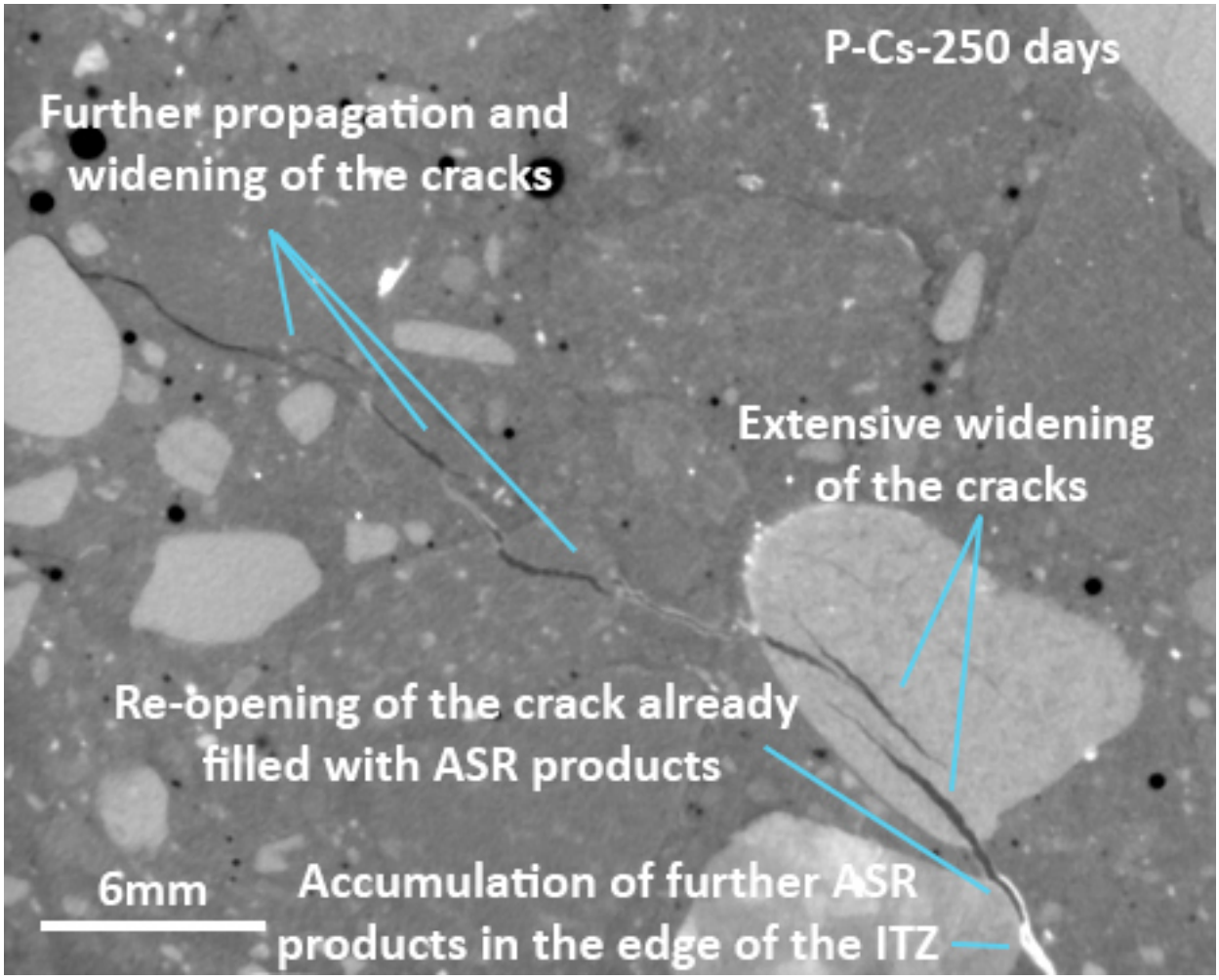

Movie MS1*: last frame of a movie simply consisting of the sequence of a* $(X - Y)$ *slice taken from the same ROI of the tomograms of the P-Cs specimen. All the tomograms in the time series of this specimen were used to create the movie. The positions of the ROI and of its slice were always the same, at each time point. At times* > 1 *day, the "non-affinely" registered tomograms were used to allow full sequential comparability of the slice at the distinct time points. The ROI used for this movie contained the one used for Figure 5 in the article. The blue line in each frame points to the main aggregate of interest, which is the same aggregate as in the center of the slices shown in Figure 5. The slice shown in this movie was not at the same exact position as the one used for Figure 5. The movie file is MS1.avi, in the uncompressed AVI format (readable by Microsoft Windows Media Player or any other media player, e.g., VLC), or MS1.mov, in the MPEG4-compressed format (readable by QuickTimeX or Quicktime Pro on Apple's computers) and is available at https://doi.org/10.5281/zenodo.4813591.*

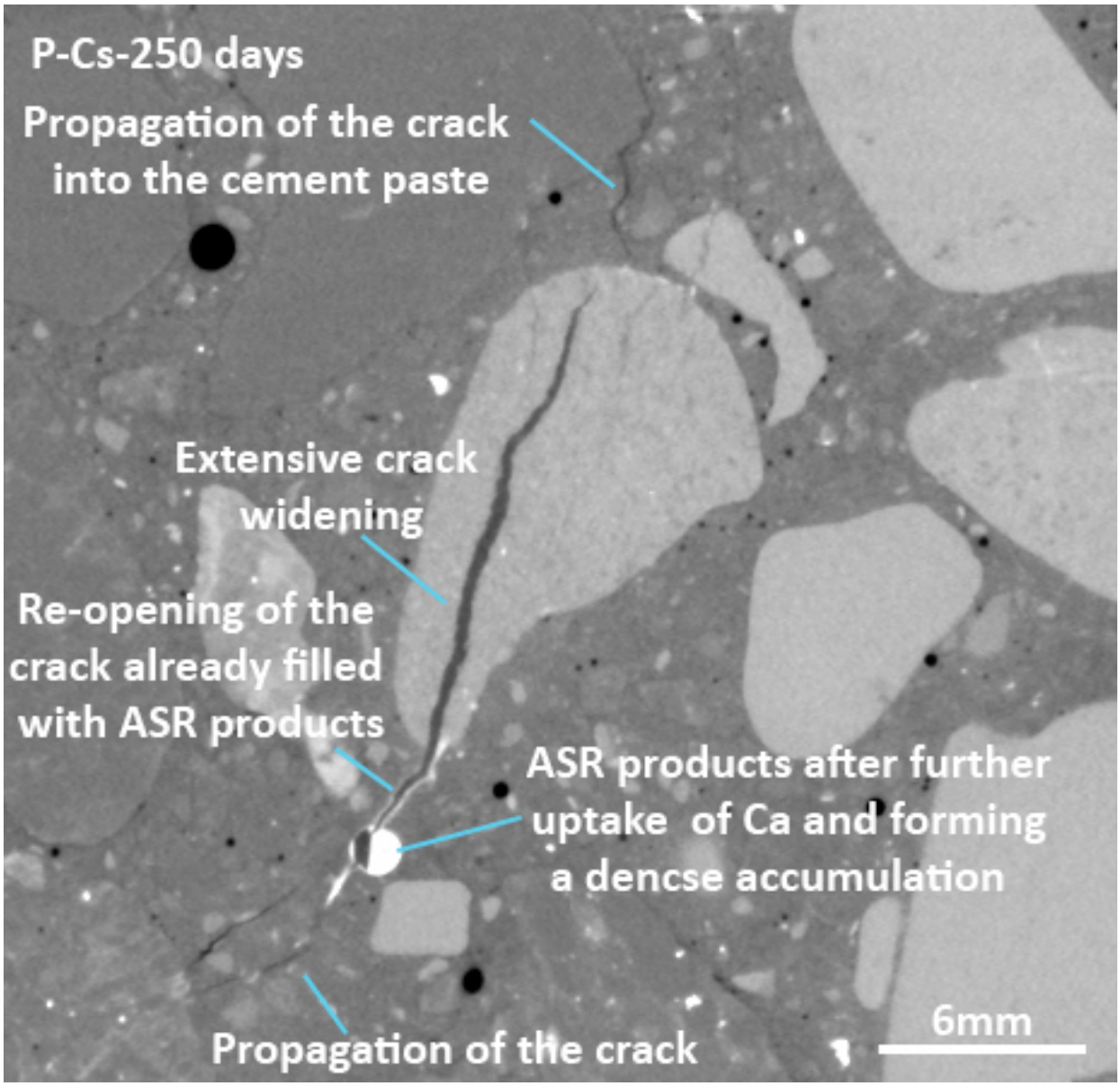

***Movie MS2**: last frame of a movie simply consisting of the sequence of a $(Z-Y)$ slice taken from a ROI of the tomograms of the P-Cs specimen, the ROI being different as the one considered in Movie MS1 but containing the ROI of the slice shown in Figure 6 of the article. All the tomograms in the time series of this specimen were used to create the movie. The positions of the ROI and of its slice were always the same, at each time point. At times $>$ 1 day, the "non-affinely" registered tomograms were used to allow full sequential comparability of the slice at the distinct time points. The blue line in each frame of the movie points to the main aggregate of interest. The movie file is MS2.avi, in the uncompressed AVI format (readable by Microsoft Windows Media Player or any other media player, e.g., VLC), or MS1.mov, in the MPEG4-compressed format (readable by Quick-TimeX or Quicktime Pro on Apple's computers) and is available at https://doi.org/10.5281/zenodo.4813591.*

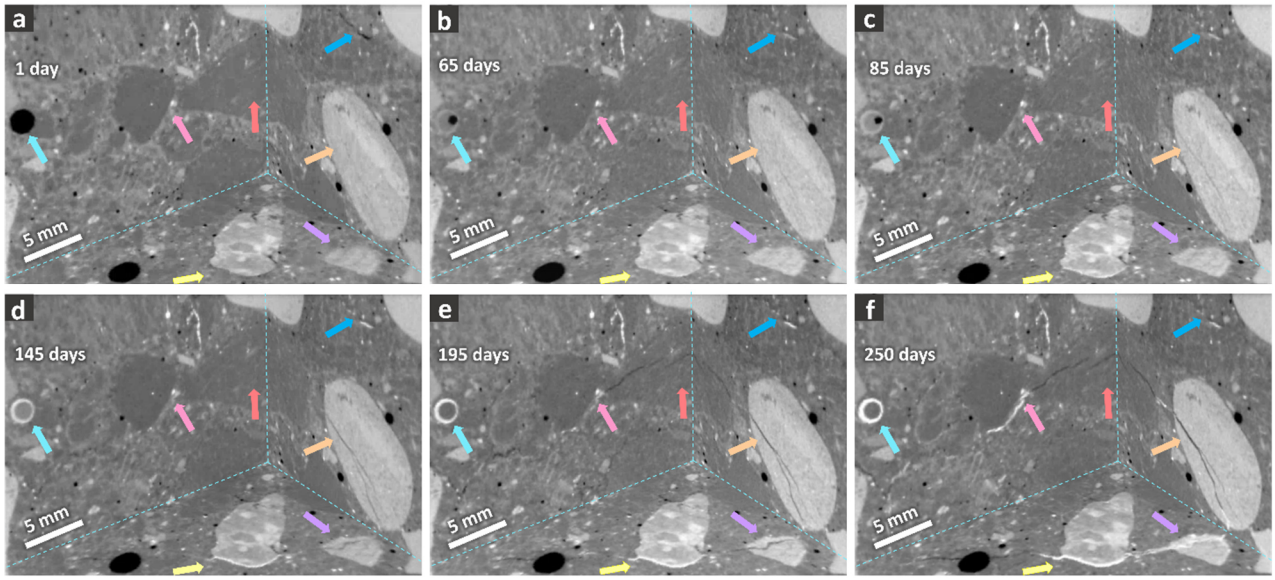

Figure S 25. An additional example of tomographic time series showing the corner of three mutually orthogonal 2D cross-sections ("ortho-slices") from another ROI of the P-Cs specimen. The specific time points at which the images are provided include: (a) 1 day, (b) 65, (c) 85, (d) 145, (e) 195 and (f) 250 days. The light cyan arrow refers to an air void which gets filled with ASR products. The blue arrow showcases an ITZ, being filled with ASR products. The orange arrow points to part of an aggregate with a pre-existing crack which started to open up before other regions in this ROI. The purple arrow refers to the tip of the same aggregate, as the one pointed at by the orange arrow, observed in another ortho-slice. It helps to visualize the fact that this aggregate first widened due to small products at its edges. Then, such products acted like a "jack" which pushed the pieces of that aggregate apart. The opened crack then got filled with further ASR products. The pink arrow shows the ASR products being extruded from another aggregate to the ITZ of its neighbouring aggregate. The yellow arrow also shows similar phenomena as those highlighted by the pink arrow but in the ITZ of another aggregate.

Figure S 26 below shows, for the P-Cs specimen, a time series of two binary tomograms (only parts thereof) rendered in 3D as solid, colored volumes and overlapped on top of each other. The empty crack binary tomogram, $\{\tilde{I}^B_{ASR\ crack}(\vec{x}_j, t_i)\}_{j=1,\dots,N}$, is rendered in cyan. The ASR product one, i.e., the union of $\{\tilde{I}^B_{ASR\ prod.-\ crack}(\vec{x}_j, t_i)\}_{j=1,\dots,N}$ and of $\{\tilde{I}^B_{ASR\ prod.-\ void}(\vec{x}_j, t_i)\}_{j=1,\dots,N}$, is rendered in yellow. What is shown in yellow corresponds to the part of the segmented pore space filled with products, including also the parts of the crack network which are filled.

Not the full binary tomograms are rendered in such figure. For each binary tomogram, each voxel cluster with volume smaller than 10^{-3} mm^3 was excluded from the rendering. Such exclusion allowed for reducing the clutter of 3D objects in the rendered scene while focusing on the most relevant and

largest portions of both the crack network and of the ASR products. The insets (g) and (h) show the same rendering as in inset (f), except for (1) using a different point of view and (2) rendering only the regions filled with ASR products (inset (h)).

The visual comparison of the crack networks rendered in Figure S 21 and in Figure S 26 provides already qualitative evidence of larger crack volume fraction (crack volume *per* tomogram volume) in the chosen P-Cs specimen compared with the chosen P-Ref one. Notice that, in the case of the P-Cs specimen, the cracks filled with ASR products are colored in yellow and are those 3D objects with high aspect ratio. Such qualitative result is generalized and quantitatively confirmed by the data reported in Figure 8 within the article.

A general, qualitative feature of the segmented ASR products in the P-Cs specimen is that they could be observed as being distributed in a very uniform way in the tomographed volume, in some cases even far away from the aggregates or the cracks inside them or propagated inside the cement paste. Their extrusion from the aggregates into the cement paste, via opening and propagating cracks, may have not been the only reason for their presence even far away from the cracks themselves. They may have accumulated as well inside aggregate particles with size smaller than or close to the spatial resolution of the tomograms, thus not directly identifiable by visual inspection.

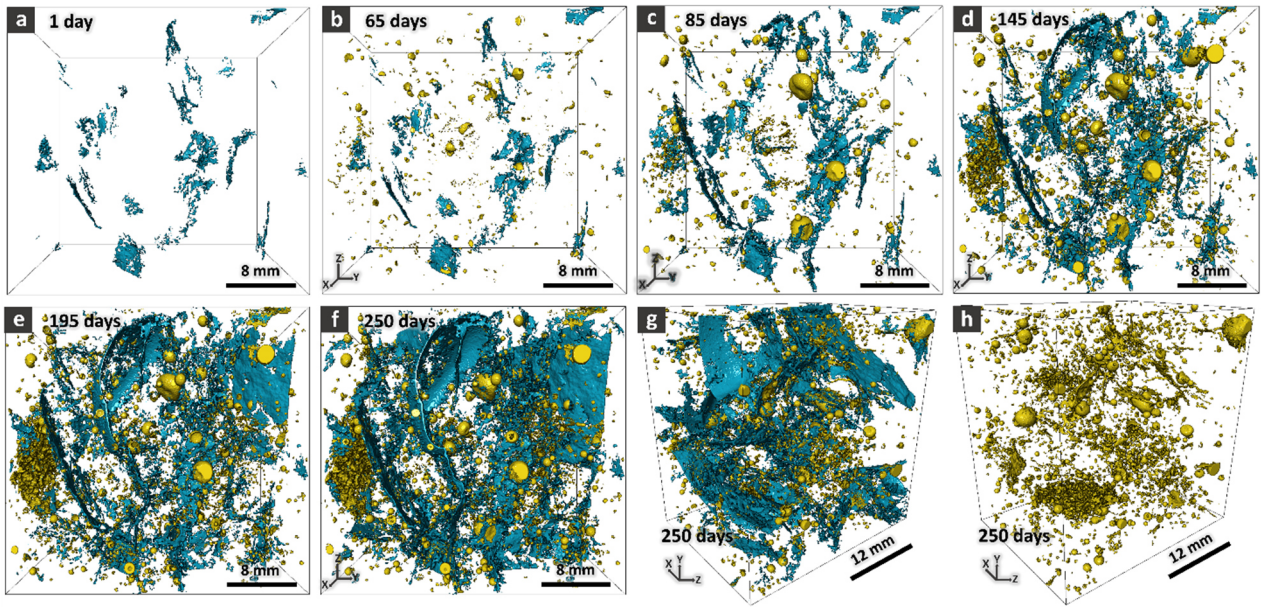

Figure S 26. (a)-(f): 3D rendering of the segmented empty crack network ($\{\tilde{I}^{B}_{ASR\ crack}(\vec{x}_j, t_i)\}_{j=1,\dots,N}$, in cyan) and of the segmented ASR products (both inside cracks, $\{\tilde{I}^{B}_{ASR\ prod.-\ crack}(\vec{x}_j, t_i)\}_{j=1,\dots,N}$, and outside them, $\{\tilde{I}^{B}_{ASR\ prod.-\ void}(\vec{x}_j, t_i)\}_{j=1,\dots,N}$, in yellow) for the tomographed part of the P-Cs specimen. Distinct insets refer to distinct time points: (a) 1 day; (b) 65 days; (c) 85 days; (d) 145 days; (e) 195 days; (f) 250 days. (g) Same as in (f) except for a distinct point of view. (h) Same as in (g) but showing only the ASR products.

U-Cs specimen

Cracking and ASR product extrusion occurred in the U-Cs specimens with similar features and patterns as in the P-Cs specimen.

Figure S27 is the analogue of Figure 5 and Figure 6 in the article but refers to a small ROI from the U-Cs specimen. It shows few, minor differences compared with the P-Cs specimen. They mainly concerned (1) the ASR product distribution, (2) its quantity and (3) the fraction of ASR-affected aggregates.

For the U-Cs specimens, the observation of ASR products in the aggregate interior regions was more frequent than for the P-Cs specimens, especially at later ASR acceleration times. This was at least the case at a length scales above our tomograms' spatial resolution. See Figure S 27 (c) and (d) for examples. This in general indicates the higher propensity of the U aggregates to ASR. It might be associated with their mineral texture.

Since resolvable ASR product accumulation inside aggregate cracks (in addition to paste cracks and air voids) happened more frequently for the U aggregates than for the P ones, a considerable portion of regions containing ASR products had an elongated, crack-like morphology in the U-Cs specimen. On the contrary, the regions containing ASR products in the P-Cs specimen had mainly a rather isotropic shape. Compare Figure S 26 with Figure S 28, for some examples. Such difference points at a higher crack filling ratio by ASR products in the U-Cs specimen than in the P-Cs one.

Figure S 29 shows, for the U-Cs specimen, more details of the ASR crack propagation and products extrusion by focusing on a single, small ROI containing a single aggregate, just as similarly visualized in Figure 7 of the article for the P-Cs specimen.

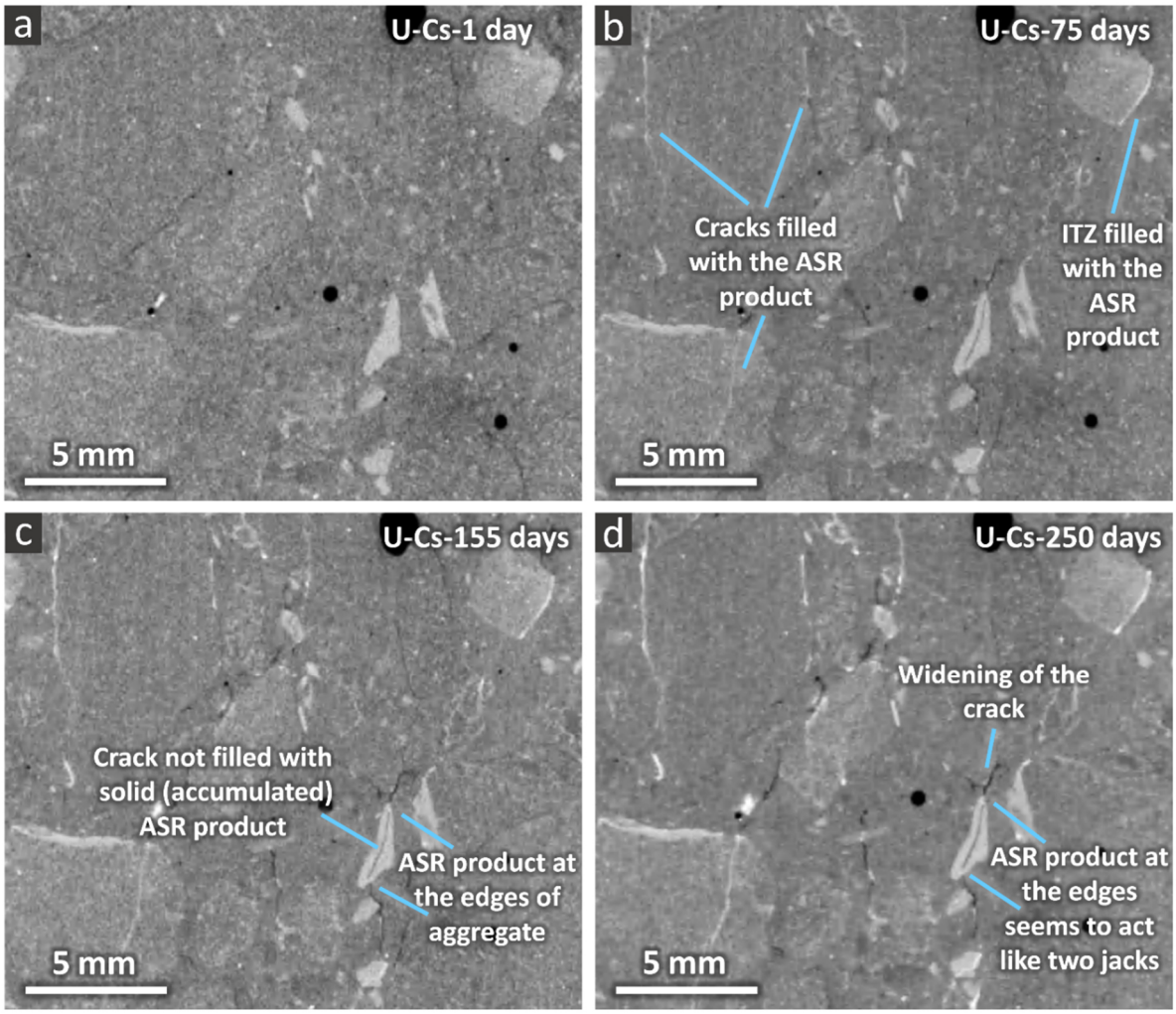

Figure S 27. A slice from a ROI of the U-Cs specimen at four different time points. ASR products can be observed as very bright regions within cracks and near the aggregate boundaries. The four slices shown here are from the tomograms at (a) 1 day, (b) 75 days, (c) 155 days and (d) 250 days, respectively.

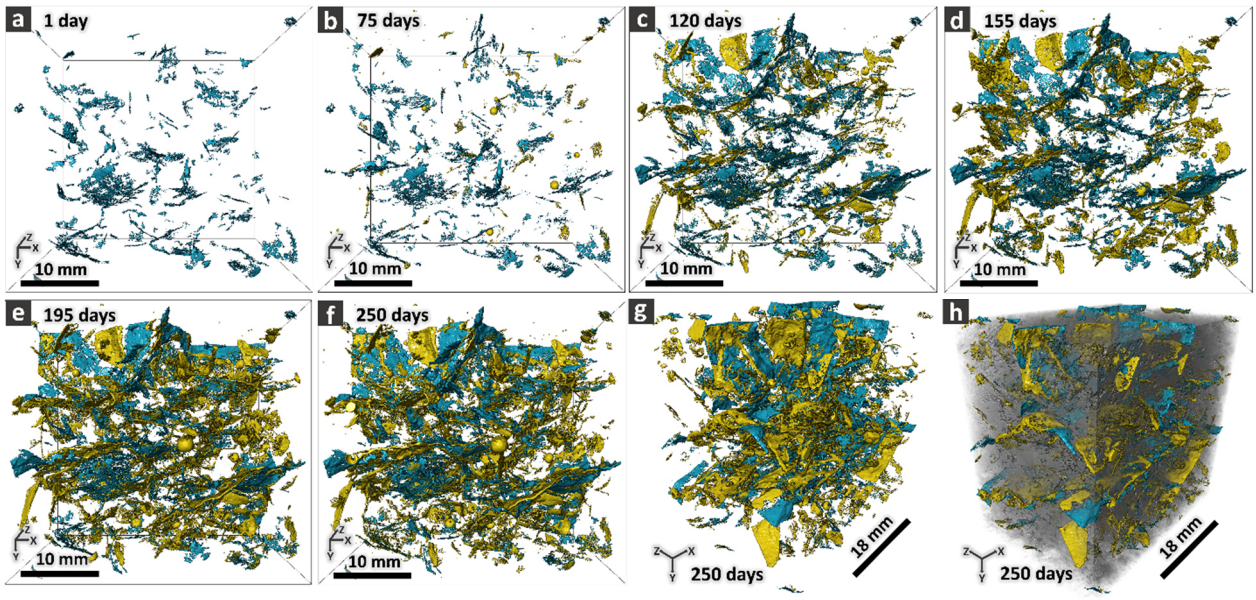

Figure S 28. Same as in Figure S 26 but for the tomographed part of the U-Cs specimen. In inset (h), instead of showing only the rendering of the segmented ASR products, also the empty crack network is shown, in addition to the rendering, in semi-transparent grey tones, of the fully registered tomogram at 250 days.

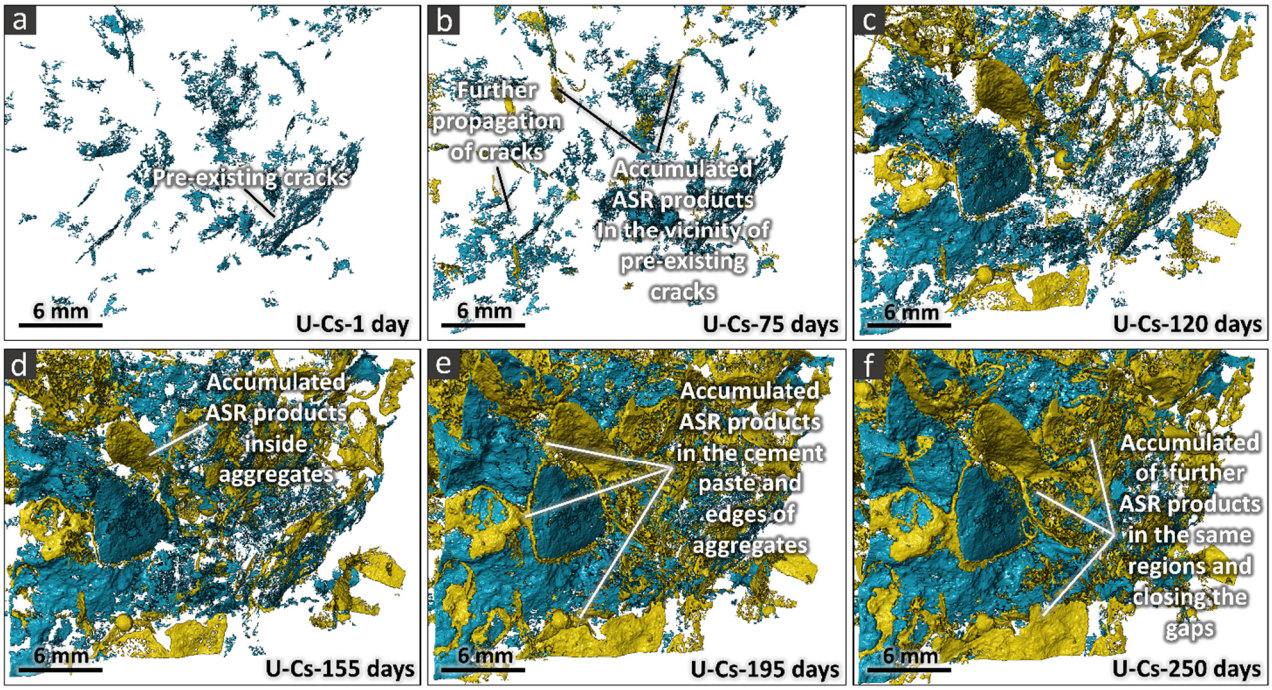

Figure S 29. A small ROI of the binary tomograms of empty cracks (in cyan) and of ASR products (both inside and outside cracks, in yellow) is rendered for the U-Cs specimen. Such ROI contained cracks which were nucleated in an aggregate and further propagated into the surrounding cement

paste. The insets from (a) to (f) correspond to different time points during the ASR acceleration, including 1 day, 75, 120, 155, 195 and 250 days, respectively.

S9. Quantitative analysis of ASR cracking by time-lapse tomography. Volume fractions.

The left column of Figure S 30 shows the time series of the normalized volume of ASR-generated cracks, $V_{ASR\ cracks}$, as defined in Eq. (4) within the article, as well as the normalized volume of ASR products (inside and outside cracks). The normalization of both volumes was performed by the tomogram's volume, $V_{tomogram}$. In addition to the time series for the P specimens, already shown in Figure 8 of the article, those of the U specimens are also shown.

The right column of Figure S 30 shows the time series of the volume of ASR-generated cracks normalized by the volume of cracks detected at the reference time t_0 = 1 day, when the ASR acceleration started. Such normalized volume is defined as

$$\frac{\Delta V_{tot,crack}}{V_{tot,crack}}(t_i) = \frac{V_{tot,cracks}(t_i) - V_{tot,cracks}(t_0)}{V_{tot,cracks}(t_0)} \quad ,\forall\ i = 1,2,\dots,T \qquad \text{(ES15)}.$$

While the $V_{ASR\ cracks}$ time series in the left column allow comparing the ASR crack volume evolution independently of the tomographed volume's size, those in the right column allow comparing its evolution independently of the amount of cracks existing before the ASR acceleration started.

The results shown in Figure S 30 and those shown in Figure 1 in the article and Figure S 17 suggest the existence of a positive correlation between the 1D expansion and the volume of ASR-generated cracks. For example, the U-Ref specimens expanded, along any direction, more than the P-Ref ones (compare Figure 1 with Figure S 17). The U-Ref tomographed volume exhibited a larger ASR cracks volume than that of the P-Ref volume (compare figure S 30 (c) with S 30 (a)). The same pattern is found when the comparing is performed between the Cs-doped specimens or, for any aggregate type, it is performed between specimens without and with Cs-doping. Such positive correlation is more appreciable by the scatter plot in Figure S 31, showing the relative length change, as measured by the mechanical gauge, of the tomographed specimen *versus* its tomographed volume's $V_{ASR\ cracks}$.

The U-Cs specimen exhibited at almost any time point larger values of the normalized volume of ASR products than the P-Cs one. As already observed in Figure S 26, in the case of the P-Cs specimen, the majority of the ASR products were located in The air voids or in (low aspect ratio) aggregate pores. Whereas, in the cases of the U-Cs specimen (Figure S 28), the products accumulated not only in the low aspect ratio pores, but also inside cracks in aggregates and in the paste. In order to quantify such difference, the ratio between the volume of ASR products inside cracks and the total volume of cracks (empty or filled) was computed (**ASR cracks filling ratio**, see Figure S 32). At 250 days, the U-Cs specimen had about 80% of its crack network filled with products, while the P-Cs specimen achieved

30%. The crack filling was quite slow at the beginning, for both aggregate types (Figure S 32). Only at 120 days, the specimens with the two aggregate types started to exhibit a significant difference in cracks filling ratio. After 195 days the cracks filling ratio rate seemed to decline. That may have mirrored the prevalence, from that point on, of product accumulation in the air voids (or in other parts of the pore space) rather than only within the ASR cracks.

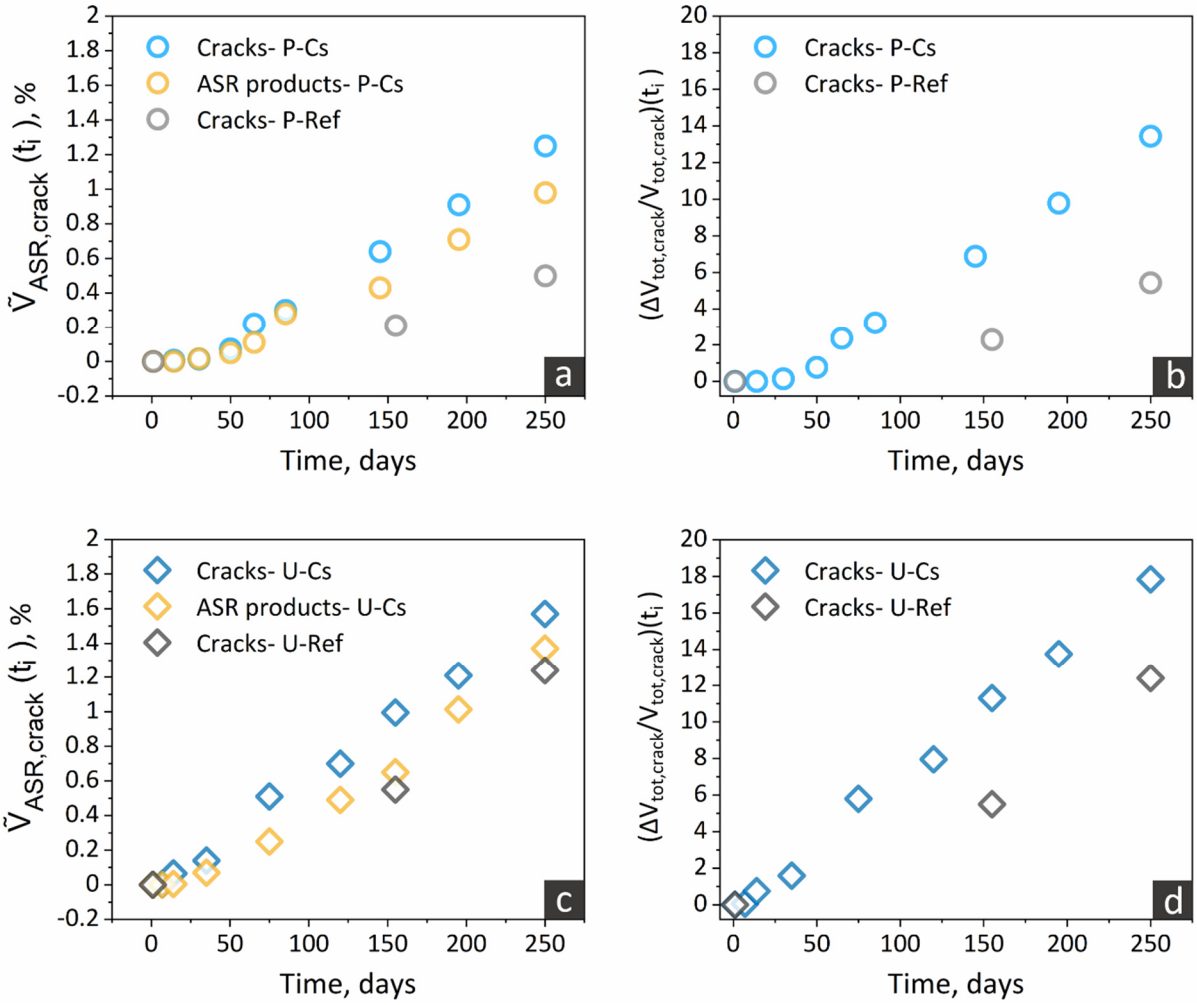

Figure S 30. Quantitative comparison of the ASR cracking in different specimens based on the estimates of two variables: (1) the total volume of ASR-induced cracks (with or without ASR products), normalized by the tomogram volume (named as $V_{ASR\ cracks}$) for the (a) P-Cs and (c) U-Cs specimens, respectively. the total volume fraction of ASR products in each specimen is also shown as yellow markers in each corresponding plot; (2) the total volume of ASR-generated cracks normalized by the volume of cracks at the reference time t_0= 1 day, i.e., cracks existing before the start of the ASR acceleration (the latter variable named as $\frac{\Delta V_{tot,crack}}{V_{tot,crack}}$) for the (b) P-Cs and (d) U-Cs specimens, respectively.

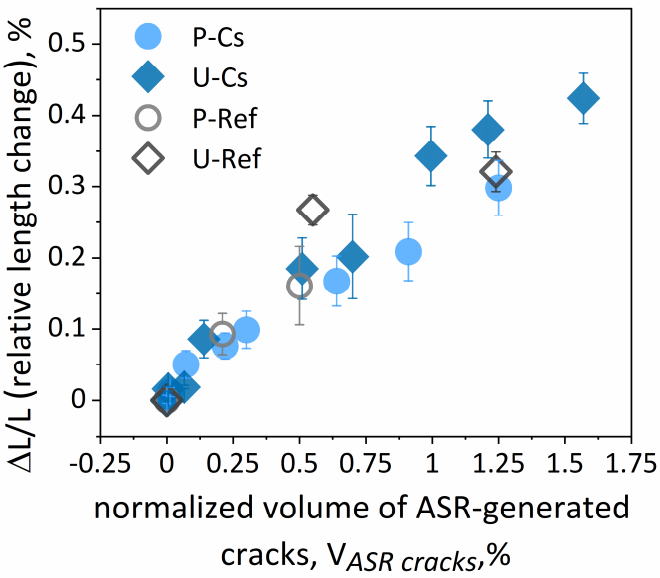

Figure S 31. Scatter plot of the ASR-generated crack volume (normalized by the tomogram volume, $V_{ASR\ cracks}$, see Eq. (4) in the article) and the whole-specimen relative length change measured with the mechanical gauge (see Figure 1 in the article and Figure S 17 for the P and U specimens, respectively). Empty markers refer to the specimens without Cs-doping. Solid markers refer to the specimens with Cs-doping. For each specimen type, the relative length change values are the average of experimentally measured values of relative length changes for six specimens (including the one being the subject of the tomography analysis) of each mix type. The error bars show their standard deviation.

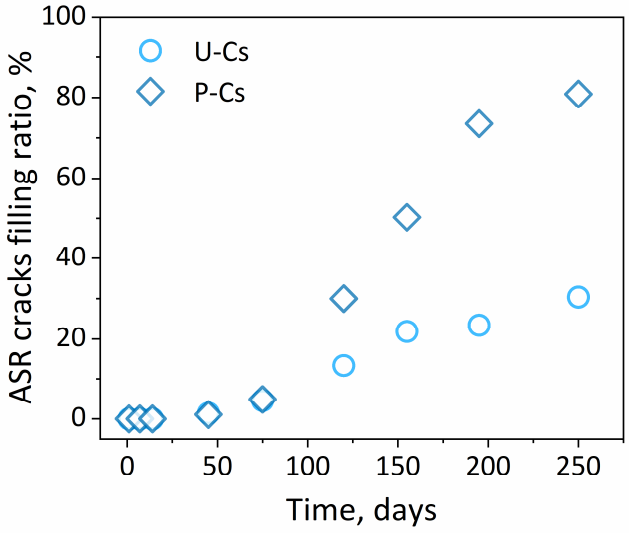

Figure S 32. Time series of the ASR cracks filling ratio, defined as the volume of ASR products classified as belonging to cracks divided by the volume of the total crack network (i.e., ASR cracks containing or not products).

S10. Quantitative analysis of ASR cracking by time-lapse tomography. Crack network features.

S10.1 Shape tensor analysis of the separated cracks.

Validation and meaningfulness

Insets (a)-(c) in Figure S 33 show 3D renderings of the segmented, total crack network (with or without ASR products) of the U-Cs specimen at three distinct time points (120, 155 and 250 days in insets (a), (b) and (c), respectively). Distinct, disconnected branches of the network (simply termed as separate cracks) are rendered with distinct colors. With time, the color of a branch may change as it becomes connected with other branches and becomes part of a new, distinct crack.

Such 3D renderings provide a qualitative idea about the complex evolution of the overall crack network, characterized by a dynamic reorganization of the relative locations of its distinct and separate branches. Despite such complexity, it is evident that several branches of the network can be clearly distinguished. This feature means that (1) the segmentation captured a significant part of the resolvable crack volume and (2) the crack network labelling managed to recognize as distinct parts the different branches of the network.

Figure S 34, Figure S 35 (a) to (c) and Figure S 36 are analogous to Figure S 33 (a) to (c). They refer to the U-Ref, P-Cs and P-Ref specimens, respectively.

The comparison of Figure S 34 with Figure S 36 clearly provides qualitative evidence of less cracking in the P-Ref specimen (Figure S 36) than in the U-Ref one (Figure S 34). The comparison of Figure S 33 (a)-(c) with Figure S 35 (a)-(c) suggests a higher "fragmentation degree" of the crack network in the P-Cs specimen compared with the U-Cs one.

The shape tensor analysis, performed at each time point for the segmented crack network of each specimen, allowed validating or not qualitative observations like the previous one, which relied only upon visual inspection of the 3D rendering of the labelled crack network.

Figure S 33 (d) to (f) shows the 3D renderings of three separate cracks, respectively. They belong to the U-Cs specimen at 250 days. We selected these cracks as examples because they have, from (d) to (f), increasingly complex morphology, e.g., surface folding and fragmentation. While the large, orange box in each inset indicates the tomographed volume, the small blue box is the bounding box of the individual crack, as computed by its shape tensor analysis. Such box is oriented along the three *eigen*vectors of the shape tensor $\boldsymbol{G}$ of the crack. The *eigen*vectors are rendered as solid arrows, starting from the center of mass of the crack itself.

Such type of visual analysis allowed validating qualitatively the shape tensor analysis results. The size of an object along the direction of one *eigen*vector of $\boldsymbol{G}$ may not necessarily provide useful, quantitative information about the object itself. The shape tensor analysis, in this regard, may be

hindered or biased just as it happens with other approaches to estimate size and orientation of a 3D object. That is because the definition of size and orientation is an ill-posed problem for 3D highly convoluted and irregularly shaped objects, as separated cracks are. Indeed, there is no unique and unequivocal definitions of size and main orientation of an object with arbitrary shape.

In our specific case, the type of visual analysis mentioned above showed that the directions of the three *eigen*vectors of $\boldsymbol{G}$ provided, for most of the cracks, the right information about the directions of maximum, intermediate and minimum spatial extent of the crack, despite its eventual complex morphology. Figure S 33 (d)-(f), for the U-Cs specimen, and the analogous Figure S 35 (d)-(f), for the P-Cs specimen, showcase this result. Correspondingly, the lateral sizes of the mentioned crack bounding boxes (length *L*, height *H* and thickness *T*) could be, for a majority of the cracks, meaningfully used for a quantitative assessment of the crack sizes. That was valid for both the reference and the Cs-doped specimens and for each aggregate type. The exceptions consisted of cracks with rather folded surface, e.g., concave cracks as those shown in Figure S 37. For such cracks, the bounding box thickness *T* achieved values which significantly overestimated the scale of an actual crack thickness. In order to avoid the statistics of an indicative crack thickness being spuriously biased by such overestimated boundary box thickness values, we decided not to adopt this feature variable as indicative crack thickness. Instead, we analyzed the statistics of the crack network's local thickness field, $T_{local}(\vec{x})$, introduced in Section S3.5 above.

We finally remark that estimates of crack length and crack height/width more accurate than the computed L and H would need to take into account the actual curvature field of the 3D object, e.g., of its tortuosity [36]. Achieving such more accurate estimates requires more advanced approaches and respective computational techniques and it still presents several challenges. See for example Section 2.6 in [36] and [37] for a description of the open problems and respective approaches. The adoption of such approaches in our work extended beyond the focal points and target of our work, i.e., obtaining meaningful and representative quantitative estimates of crack size even though not the most possible accurate.

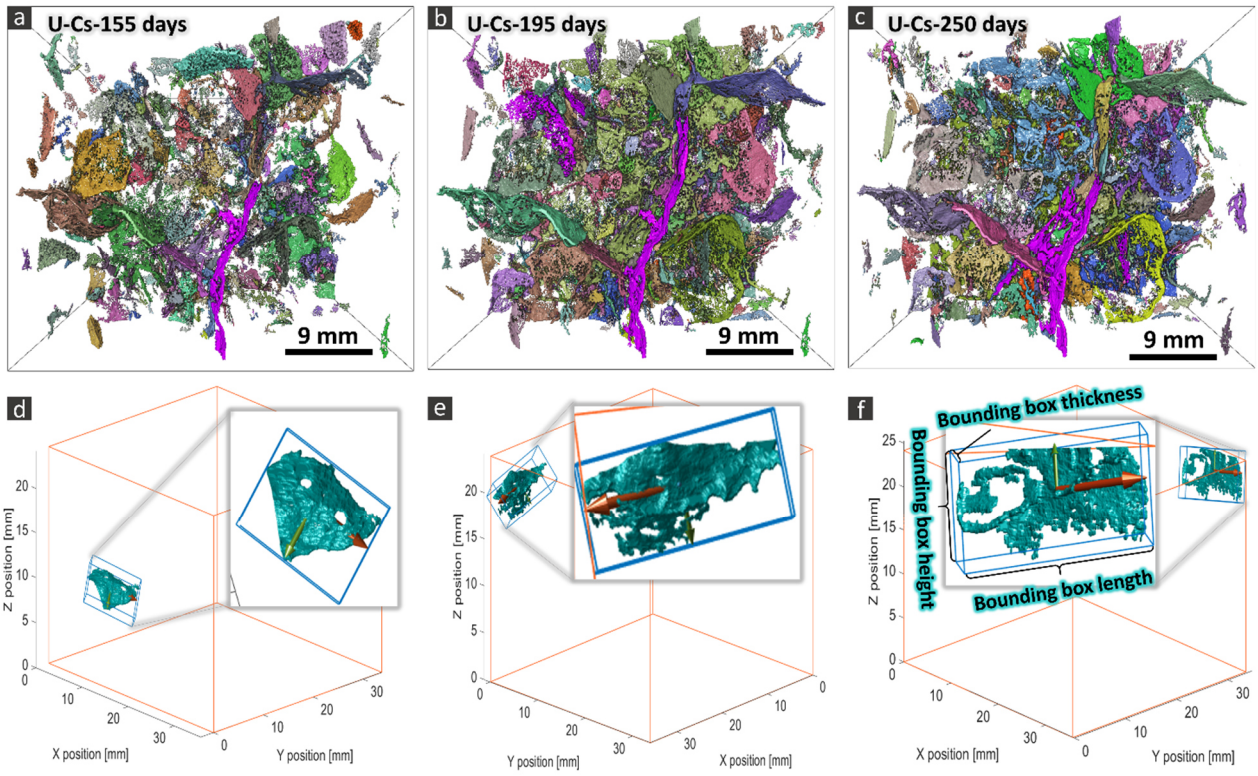

Figure S 33. 3D rendering of the segmented, total crack network (containing or not containing ASR products) of the U-Cs specimen, at 155 days, 195 days and 250 days, insets (a), (b) and (c), respectively. In each of insets (a)-(c), each separated part (branch) of the crack network is rendered with a distinct color, just for the purpose of distinguishing them. The color assignment to each branch was random, i.e., did not remain consistent in time, due to the evolution, e.g., merging or splitting, of the crack network branches. Insets (d)-(f) show three examples of separated branches of the crack network at 250 days, for the same specimen. The large parallelepiped box highlighted in orange delineates the tomographed volume. The smaller grey box shows a zoom-in view of the respective crack branch. The blue, parallelepiped box is the crack's bounding box oriented according to the three eigenvectors of the crack's shape tensor $\boldsymbol{G}$. Each eigenvector, located at the center of mass of the crack and scaled by half the lateral size of the bounding box along the same direction, is also rendered as a solid arrow. The red arrow refers to the eigenvector associated with the first eigenvalue. The green arrow to the second eigenvector and the blue one to the third.

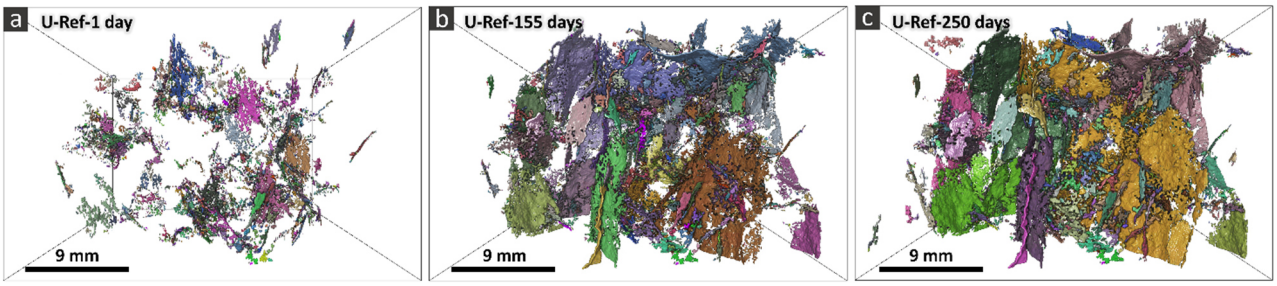

Figure S 34. Similar 3D renderings as in Figure S 33 (a) – (c) but for the U-Ref specimen.

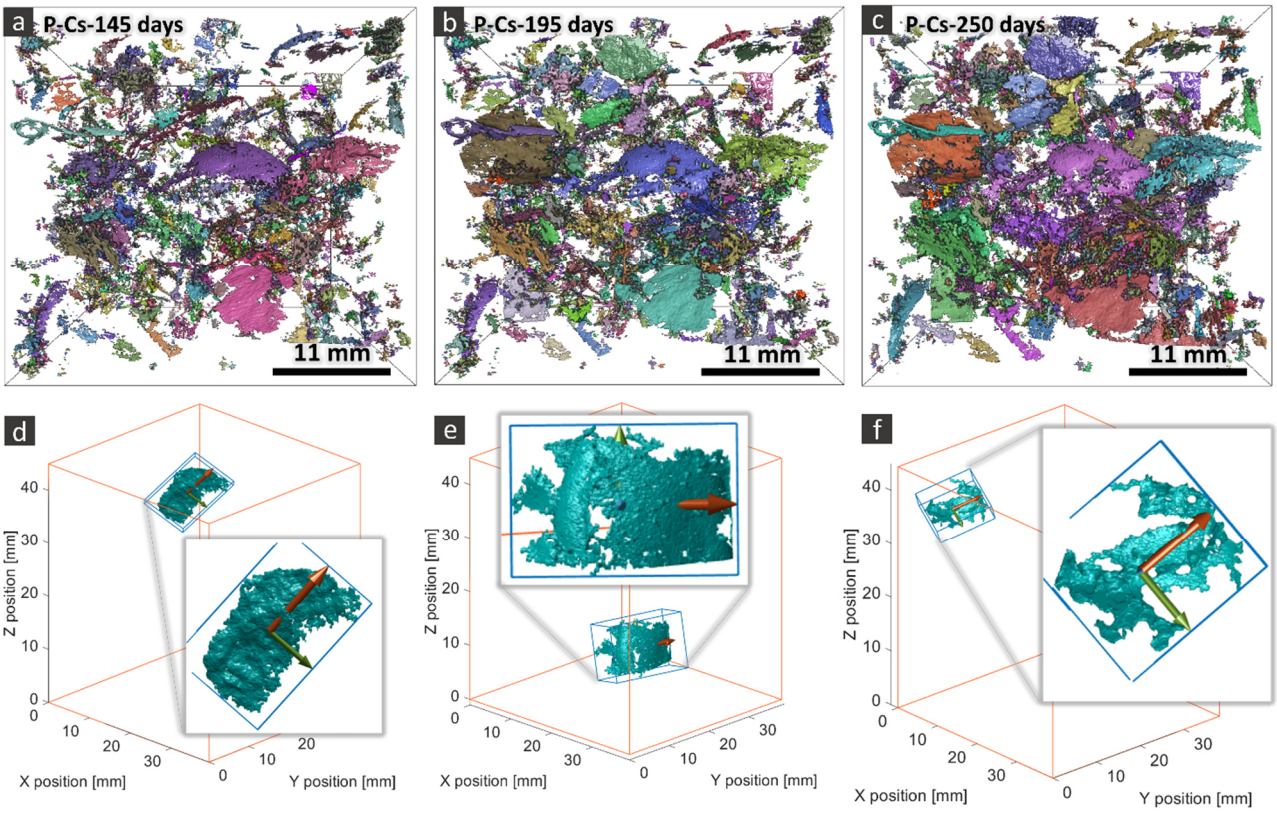

Figure S 35. Similar 3D renderings as in Figure S 33 but for the P-Cs specimen at three points of its tomographic time series.

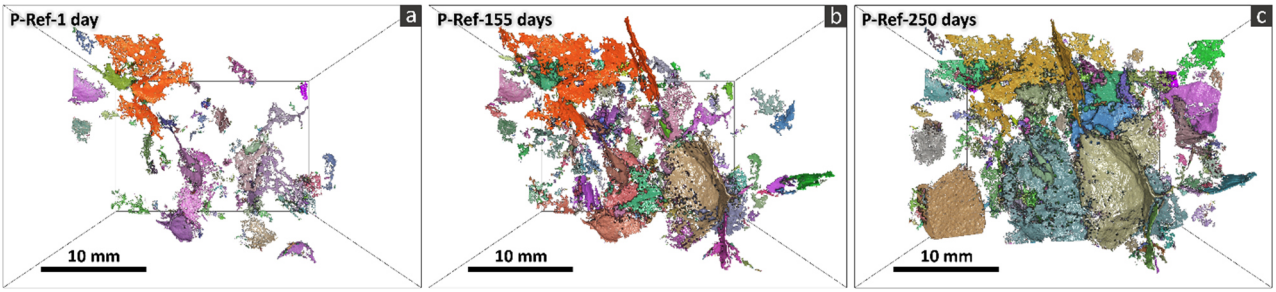

Figure S 36. Similar figure as Figure S 34 but for the P-Ref specimen.

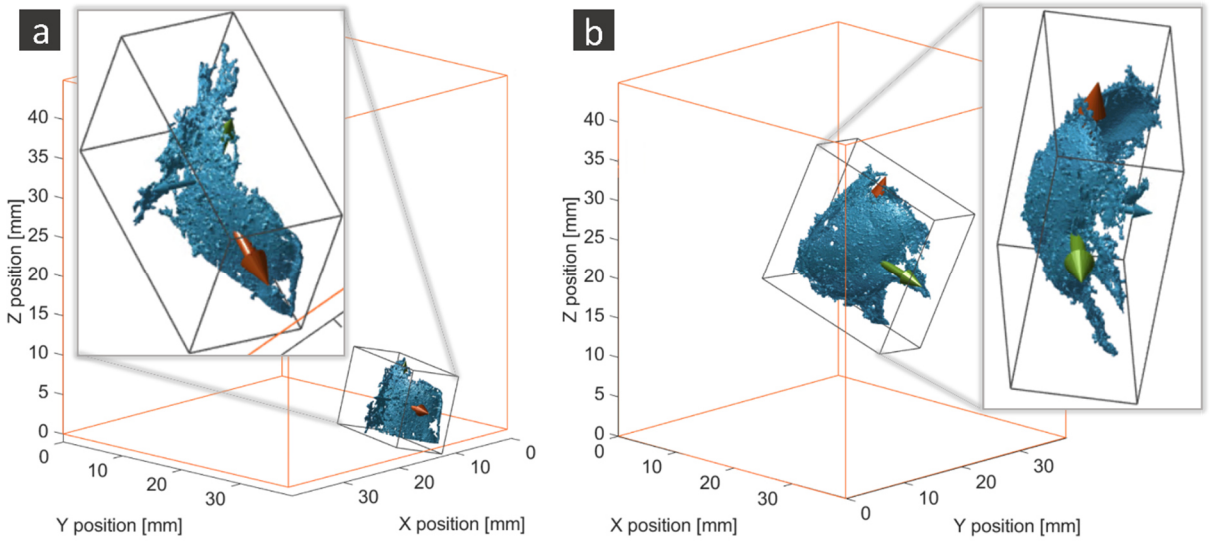

Figure S 37. Two examples of separate cracks (also called crack network branches) with rather folded surface, e.g., concave cracks. The large parallelepiped box highlighted in orange delineate the tomographed volume. The smaller, light grey box shows a zoom-in view of the respective crack network branch. The dark grey, parallelepiped box is the branch's bounding box oriented according to the three eigenvectors of the branch's shape tensor $\mathcal{G}$. Each eigenvector is also rendered as a solid arrow. It is located at the center of mass of the branch and scaled by half the lateral size of the bounding box along the same direction. The red arrow refers to the eigenvector associated with the first eigenvalue. The green arrow to the second eigenvector and the blue one to the third.

Crack size analysis results

Figures S 38 to Figure S 42 show the statistical *ensemble* estimate of the complementary cumulative distribution function (cCDF) of the bounding box length, L, the bounding box height/width, H, and of the separate crack volume, V_{crack}, in insets (a) to (c), respectively. Each cCDF is plotted in $\log_{10}$-$\log_{10}$ scales, i.e., it is shown in the form of a Zipf's plot, as done in Figure 9 in the article.

Figures S 42 and S 52 show similar plots as in Figure 9 of the article except for adding the corresponding plots for the U specimens. Figure S 42 shows the cCDFs of L. Figure S 52 shows those of T_{local}.

One remarkable feature shown in the plots of Figures S 42 and Figures S 52 is that, when comparing the cCDFs at 250 days for the specimens with distinct aggregate types but same mixing (with or without Cs-doping), no dramatic difference in the ranges of L and, more importantly, of T_{local} values is observable. This feature, combined with the results shown in Figure S 30, could provide an explanation for the difference in the macroscopic scale expansion observable in Figure 1 and Figure S 17.

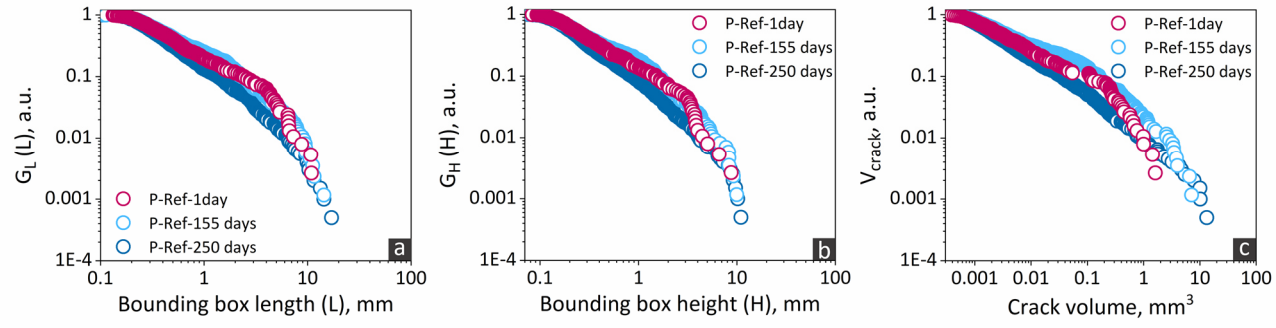

Figure S 38. Empirical (i.e., statistical ensemble) complementary cumulative distribution function of (a) the bounding box length, L, $G_L(L)$, (b) the bounding box height (also called width), H, $G_H(H)$, (c) the crack network branch (also called separate crack) volume, V_{crack}. Each complementary cumulative distribution function is plotted in $\log_{10}$-$\log_{10}$ scales (Zip'f plot). Each separate crack contributed to one sampled value for each variable.

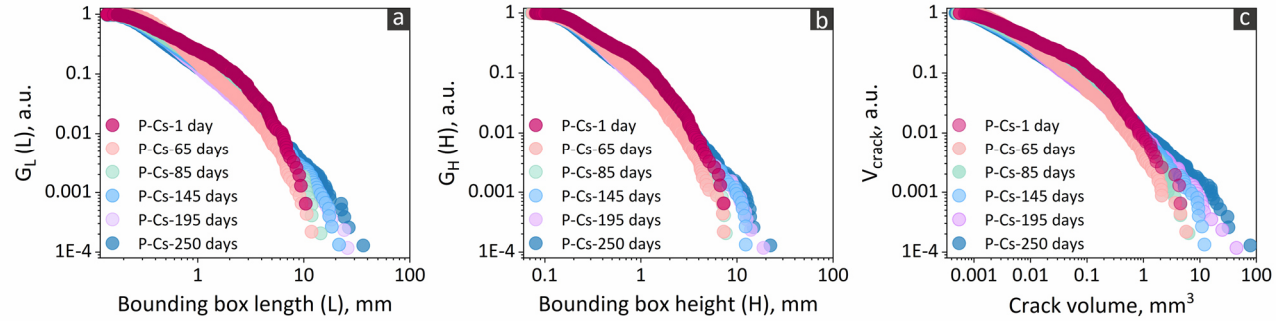

Figure S 39. Similar plots as in Figure S 38 but for the P-Cs specimen.

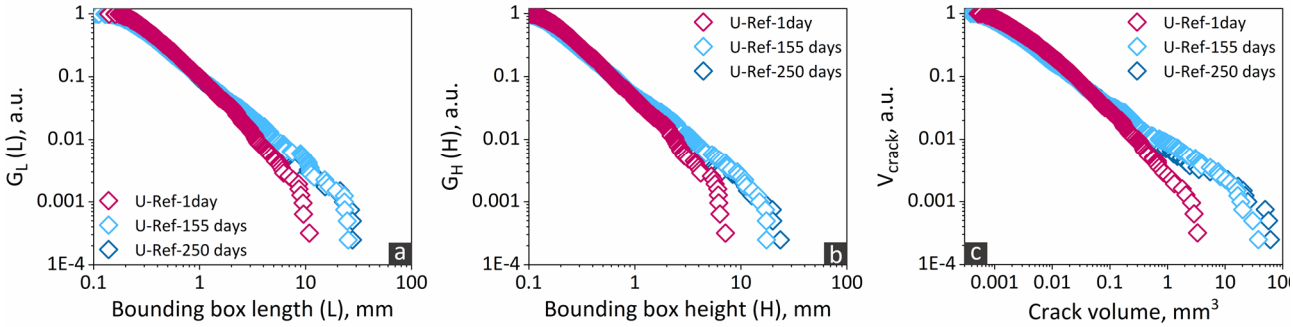

Figure S 40. *Similar plots as in Figure S 38 but for the U-Ref specimen.*

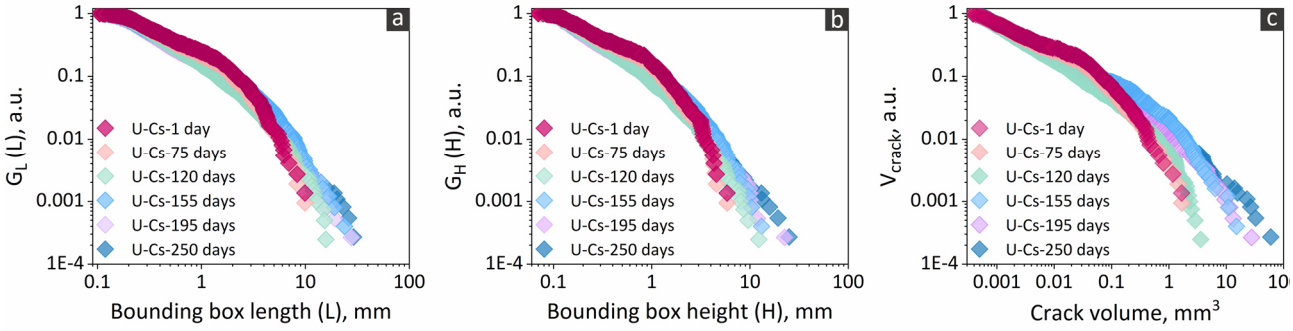

Figure S 41. Similar plots as in Figure S 38 but for the U-Cs specimen.

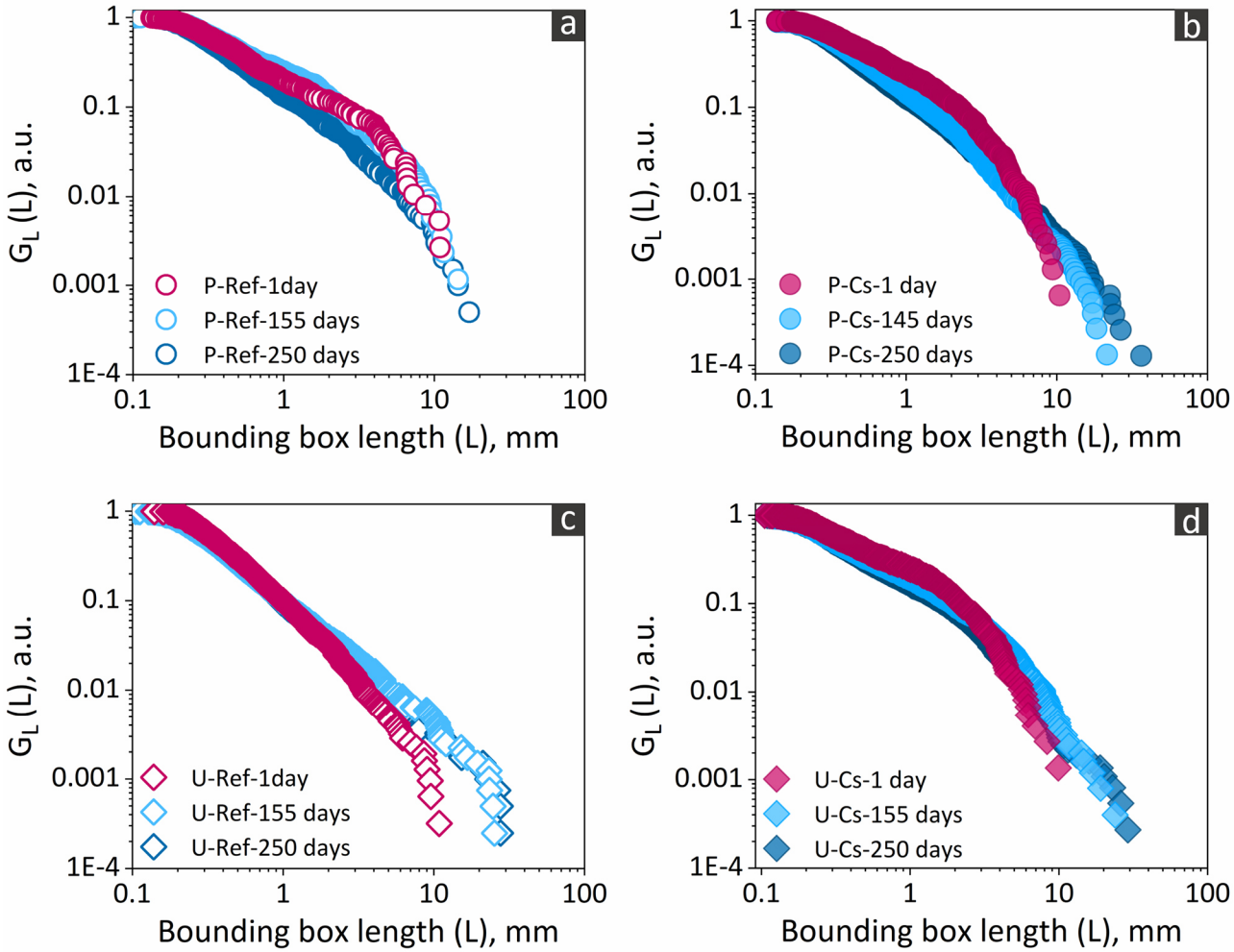

Figure S 42. Empirical (i.e., statistical ensemble) complementary cumulative distribution function of the bounding box length, L, $G_L(L)$, in $\log_{10}$-$\log_{10}$ scales (Zip'f plot). Each separate crack contributed to one sampled value for L.

Crack shape analysis results

The 3D rendering of the segmented, total crack networks illustrated in Figure S 33 to Figure S 36 show that their distinct separate cracks had a broad range of curvatures and degrees of fragmentation. The shape tensor analysis allowed confirming such visual observation. For a given specimen and a given time point, let C be the total number of independent, disconnected branches of the segmented total crack network (separate cracks, containing or not ASR products). Each of them can be mapped to a point in the $(E; F)$ shape feature space. See Eqs. (ES7) and (ES8) in Section S3.5 for the definition of the two shape anisotropy degree feature variables E and F (elongation and flatness, in short), respectively. Notice that, by the E and F definitions themselves, only the $[0; 1] \times [0; 1]$ region of such space can be populated by points. Those points close to the $(0; 0)$ corner correspond to rather spherical separate cracks, while those close to the $(1; 1)$ corner correspond to plate-like cracks.

A segmented, total crack network can be thought of corresponding to a statistical sample $\{(E_i; F_i)\}_{i=1,\dots,C}$ of a bi-variate random variable, $(\mathbb{E}; \mathbb{F})$. The plots in Figure S 43 to Figure S 45 show the kernel density estimate (KDE) of the joint probability density function (PDF) of $(\mathbb{E}; \mathbb{F})$, $f_{(\mathbb{E};\mathbb{F})}(E; F)$. The KDE of $f_{(\mathbb{E};\mathbb{F})}(E; F)$ was obtained, for each specimen and at each time point, applying the "2D Kernel Density" function of the OriginPro 2020b (v9.7.5.184) software package (OriginLab©, Northampton, MA, USA). The chosen parameters for such function included: the "Bivariate Kernel Density Estimation" as the method of density estimation, 32 number of Grid Points in X/Y, no point were used for the displaying, the Grid Range of [-0.05,1.05] for both X and Y and 300 "Interpolate Density Points".

At any time point and for any specimen, the majority of the cracks were mapped to the top-right corner of the region $[0; 1] \times [0; 1]$ in the $(\mathbb{E}; \mathbb{F})$ plane (see from Figure S 43 to Figure S 45). No relevant difference in "shape distribution" could be observed between specimens with distinct aggregate types, with or without Cs-doping, at the beginning of the experimental campaign. The evolution in time also did not seem to alter substantially the shape distribution much. The Cs-doping also did not change much the shape distribution, in comparison with the cases in its absence.

Despite the broad degree of curvature and fragmentation, the fact that the separate cracks are predominantly shaped like irregular plates allowed using the shape tensor analysis also for obtaining representative estimates of crack sizes and for a coarse assessment of the overall orientation of the distinct branches of the crack network.

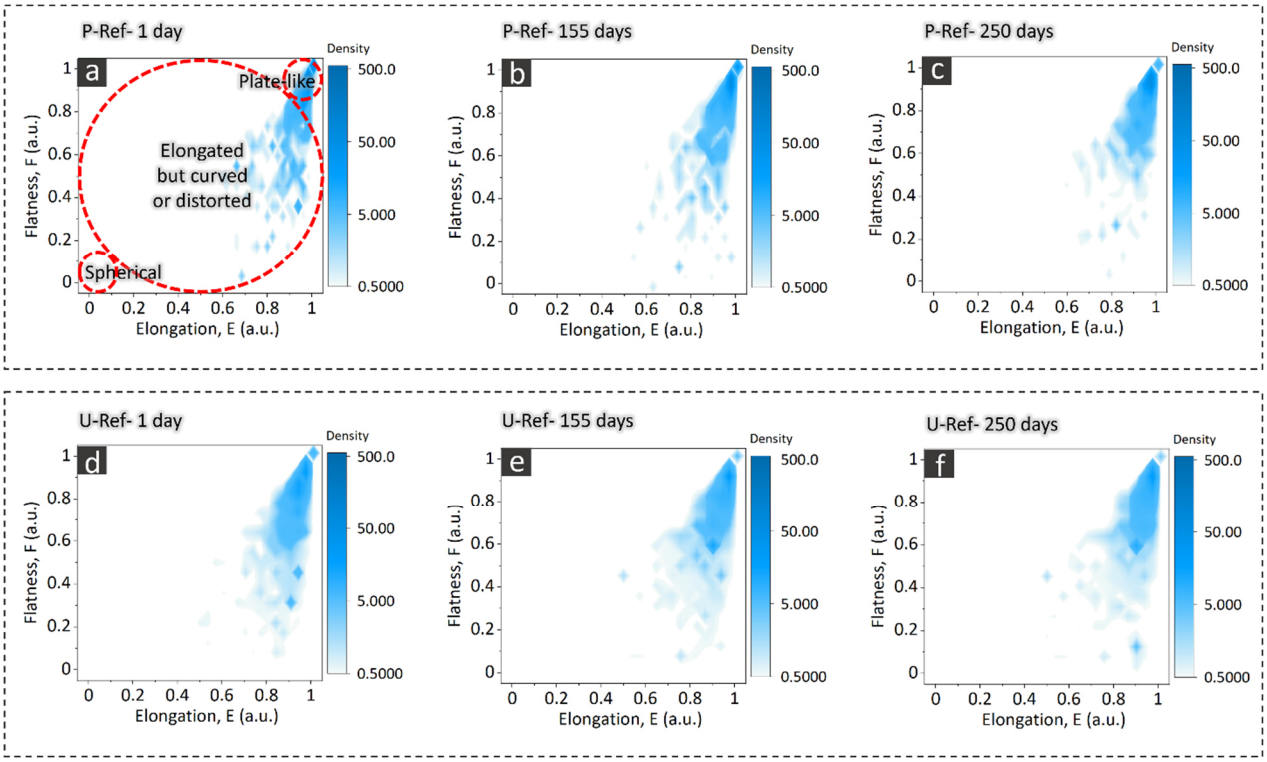

Figure S 43. Plot of the kernel density estimate (KDE) of the joint probability density function (PDF) of the two shape feature variables, the elongation E and the flatness F, computed from the shape tensor analysis of the segmented total crack network and treated as a bi-variate random variable, $(\mathbb{E};\mathbb{F})$. The statistical sample of such PDF was provided, for each specimen and at each time point, by the set of values $\{(E_i;F_i)\}_{i=1,\dots,C}$ obtained from the shape tensor analysis, where C indicates generically the total number of disconnected and independent branches of the segmented, total crack network of a specimen and at a certain time point. (a) to (c): P-Ref specimen, at 1 day, 155 and 250 days, respectively. (d) to (f): U-Ref specimen, at 1 day, 155 and 250 days.

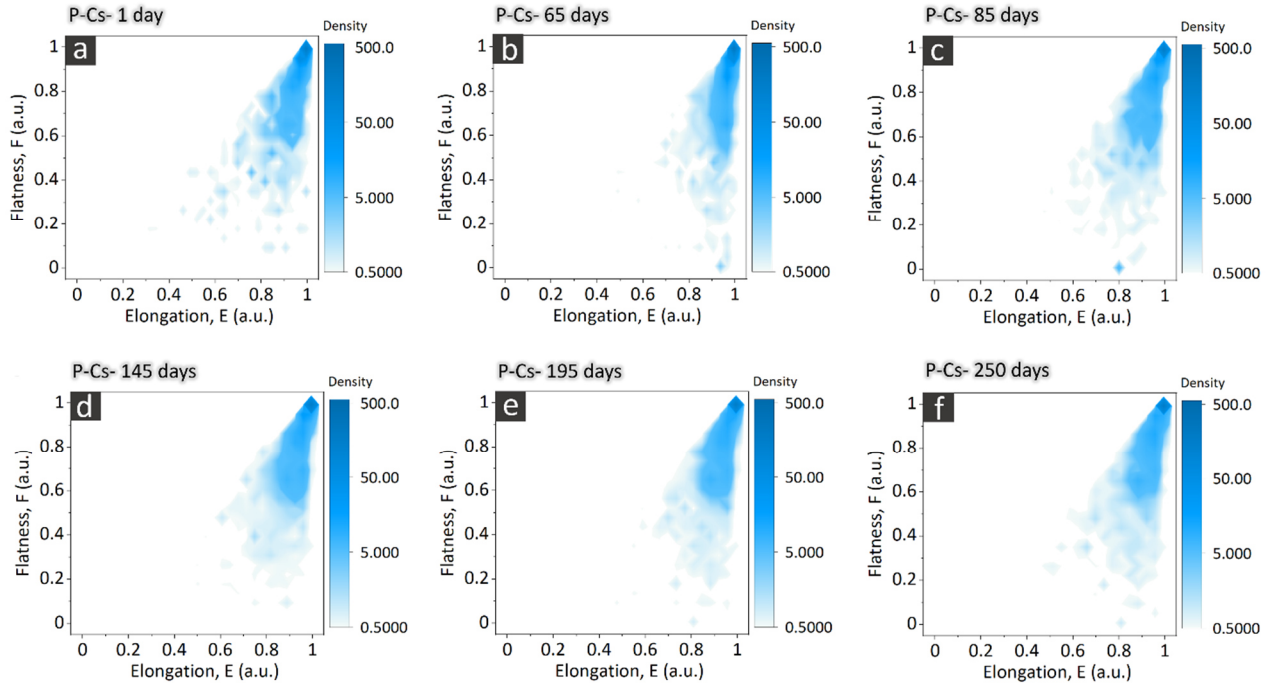

Figure S 44. Same plots as in Figure S 43 but only for the P-Cs specimen: at (a) 1 day (b) 65 days, (c) 85 days, (d) 145 days, (e) 195 days and (f) 250 days.

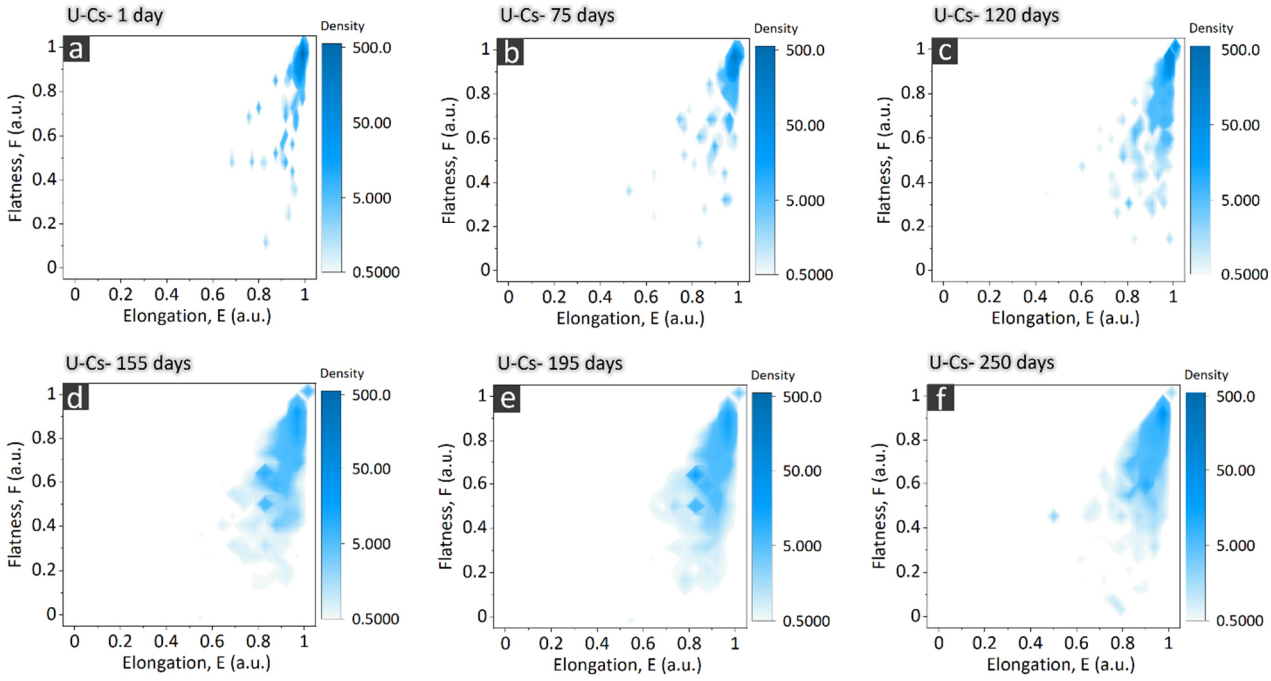

Figure S 45. Same plots as in Figure S 44 but for the U-Cs specimen.

Crack orientation analysis results

As mentioned in Section S3.5, we chose the direction of the first *eigen*vector of $\boldsymbol{G}$, $\hat{u}_1$, to define the feature variable "crack orientation". We performed only a qualitative analysis of the crack orientation of any specimen at any given time point. It was based on plotting the $\hat{u}_1$ of each separate crack. Given that the *eigen*vectors of $\boldsymbol{G}$ are unit vectors, the visualization corresponds to mapping the $\hat{u}_1$'s as points on a unit sphere. The higher the density of points in a portion of such sphere, corresponding to a certain range of spherical coordinate angles $(\varphi; \theta)$, the larger the number of separate cracks whose direction of largest extent (i.e., the $\hat{u}_1$ direction) falls in that angular range.

Figure S 46 to Figure S 48 show the plots of the full $\hat{u}_1$ vectors, after rescaling their magnitudes by a factor equal to 0.33 (in order to ensure the visibility of their projections on the $X-Y$, $Y-Z$ and $X-Z$ planes). The latter are oriented as described in Figure S16, compared with the lateral sides of the specimens. In all the figures, it can be noticed that, by increasing time, the density of vectors increased more considerably within a cone with symmetry axis approximately equal to the Z axis. No specific region of the sphere was completely empty of points/vectors. This feature indicates lack of strong orientation anisotropy. However, the higher densification towards the positive Z direction was a feature charactering every specimen, independently of the aggregate type and of the absence or the presence of Cs-doping. It suggests that Cs-doping brought no evident perturbation of the crack networks, in terms of crack orientation.

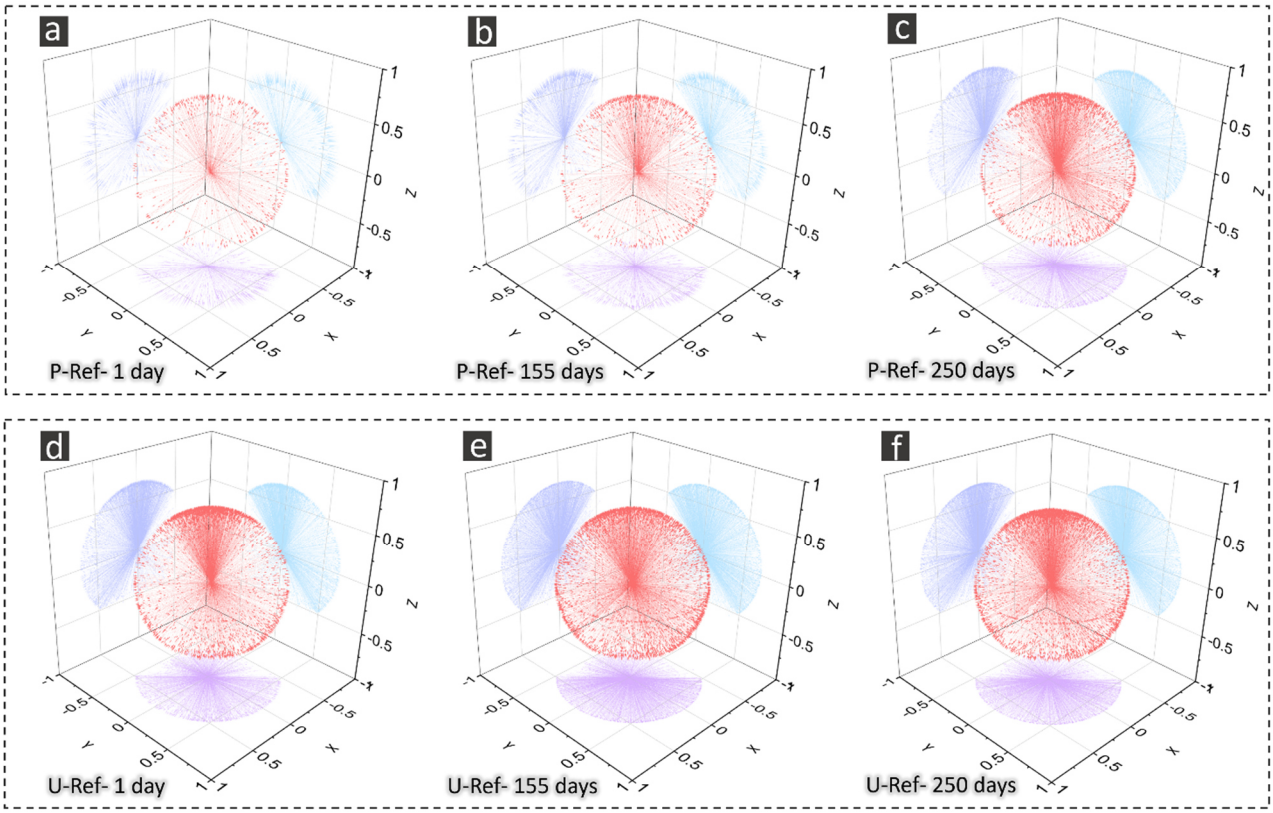

Figure S 46. Visualization of the crack orientation analysis results for the reference specimens. The "crack orientation" was operatively defined as the direction of the eigenvector $\hat{u}_1$ associated with the first and largest eigenvalue of the shape tensor $\boldsymbol{G}$. The segmented total crack network of a specimen corresponded to a set of $\hat{u}_1$'s, one for each independent crack (branch of the network). Each of these vectors are here plotted in red, after rescaling their magnitudes by a factor equal to 0.33, to make their projections on the planes of the Cartesian frame of reference more visible. The projections of $\hat{u}_1$ on the $X-Y$ plane are in violet, those on the $X-Z$ plane are in dark blue and those on the $Y-Z$ plane are in light blue. (a)-(c): distribution of the $\hat{u}_1$ eigenvectors for the P-Ref specimen at 1 day, 155 and 250 days, respectively. (d)-(f): distribution of the $\hat{u}_1$ eigenvectors for the U-Ref specimen at 1 day, 155 and 250 days, respectively.

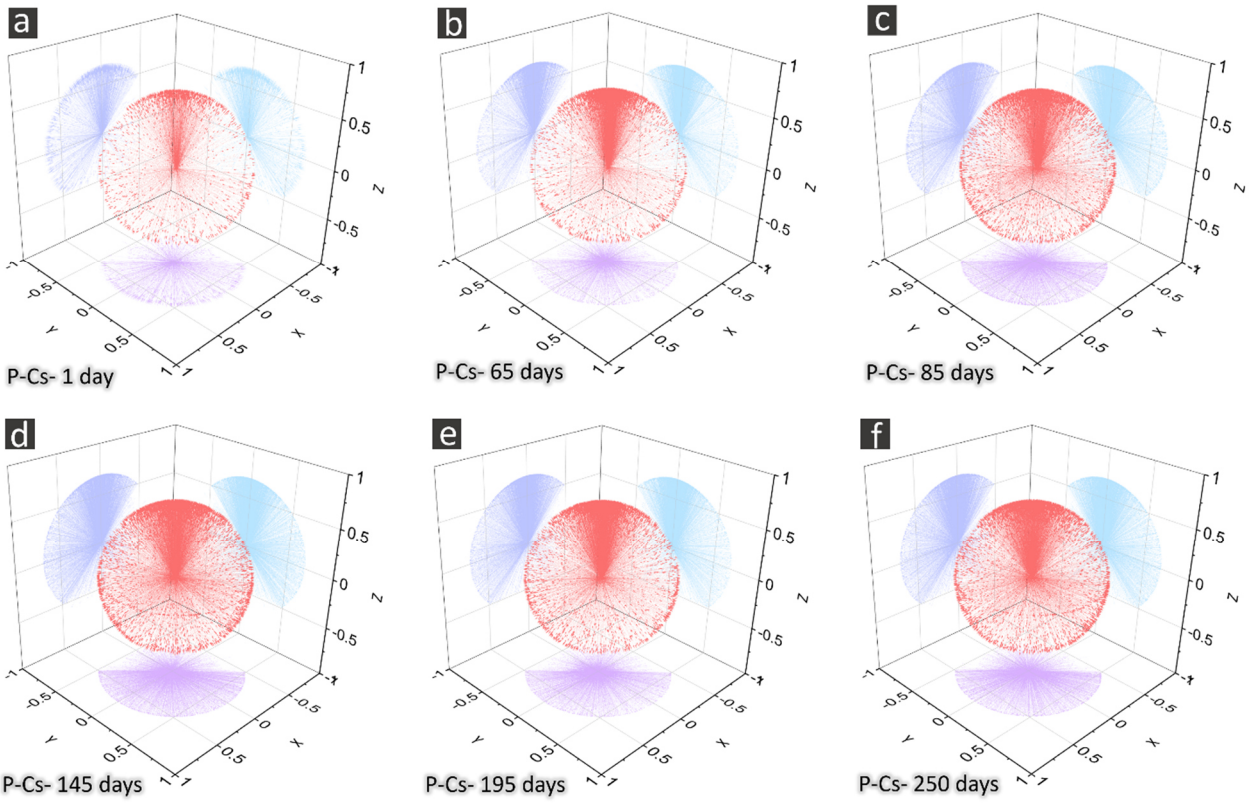

Figure S 47. Similar figure as Figure S 46 but for the P-Cs specimens at 6 of the 12 time points of measurement. (a)-(f): P-Cs specimen at 1 day, 65, 85, 145, 195 and 250 days, respectively.

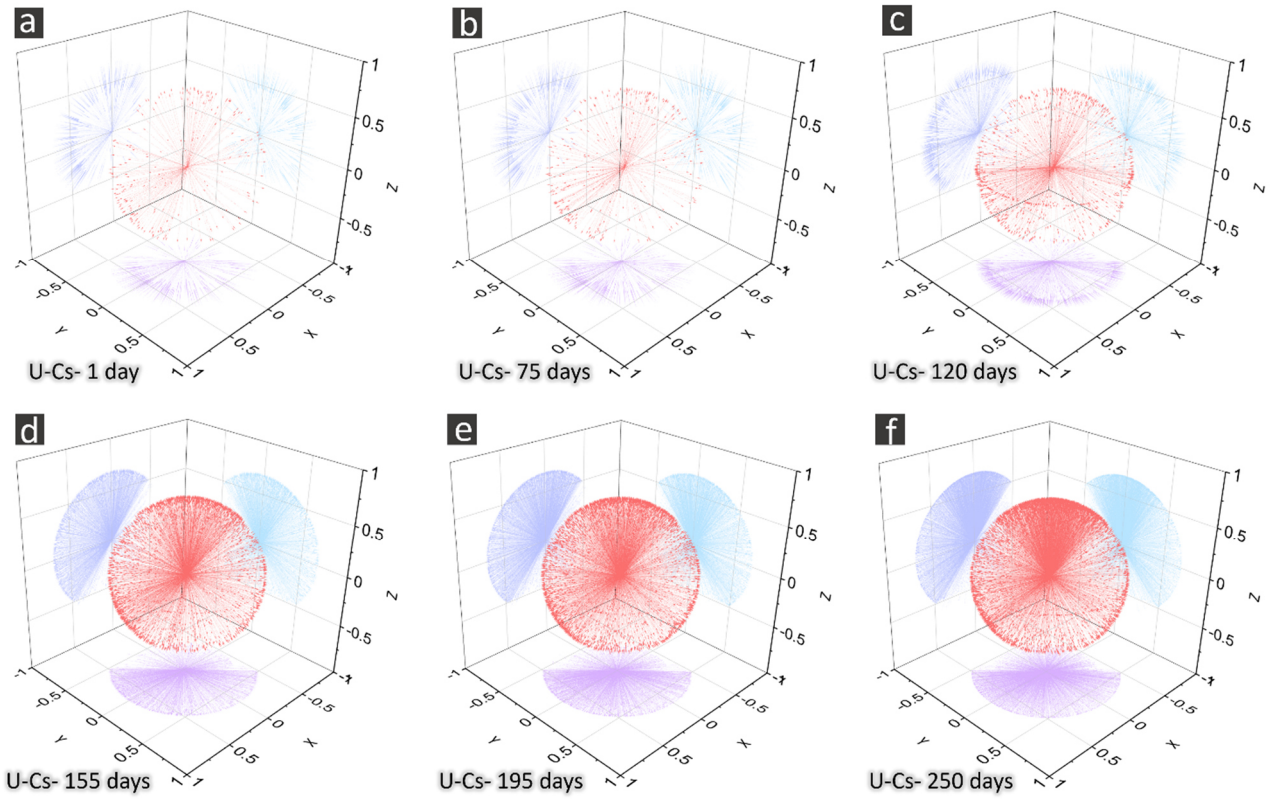

Figure S 48. Similar figure as Figure S 47 but for the U-Cs specimens.

S10.2 Crack local thickness analysis.

Figure S 49 and Figure S 50 show 3D renderings of the local thickness scalar field, $T_{local}(\vec{x})$, computed for the segmented total crack networks of all the specimens and at certain time points. Figure S 49 contains results for the two reference specimens. Figure S 50 shows results for the two Cs-doped specimens. $T_{local}(\vec{x})$, by definition, has value equal to 0 outside the segmented total crack network regions. Thus, in Figure S 49 and Figure S 50, the reader can essentially see 3D renderings of the total crack networks, similar to those in Figure S 33 (a)-(c), Figure S 34 (a)-(c), Figure S 35 (a)-(c) and Figure S 36 (a)-(c). However, the difference consists of the fact that each voxel of a network is rendered with a color which is mapped to the value of T_{local} at that voxel's position. The color scale in each inset of Figure S 49 and Figure S 50 is always the same and is mapped to the same range of T_{local} values. The complementary cumulative distribution function of T_{local}, computed for any specimen (with and without Cs-doping) and (for the Cs-doped specimens) at additional time points, compared with what shown in Figure S 52, is shown in Figure S 51Figure S .

The 3D renderings in Figure S 49 and S 50 confirm visually what observable in Figure 9 within the article and in Figure S 51 and Figure S 52: a gradual temporal shift of the T_{local} value distributions

(especially their right-hand side tails) towards larger values. No significant differences in the spatial-temporal T_{local} distributions of the reference specimens could be noticed.

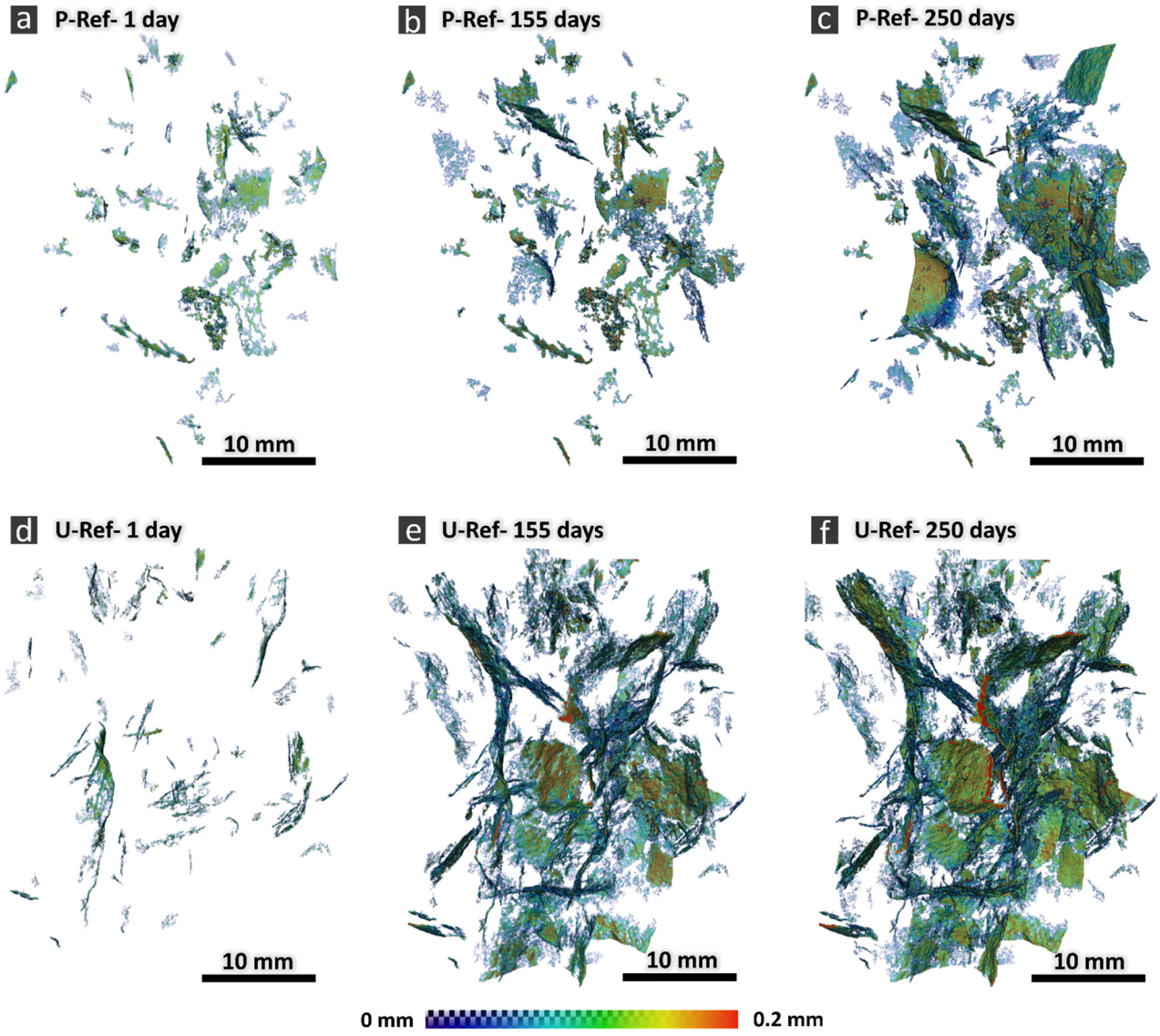

Figure S 49. 3D rendering of the local thickness scalar field, $T_{local}(\vec{x})$, computed for the segmented total crack network. (a)-(c): P-Ref specimen at 1 day, 155 and 250 days. (d)-(f): U-Ref specimen at 1 day, 155 and 250 days.

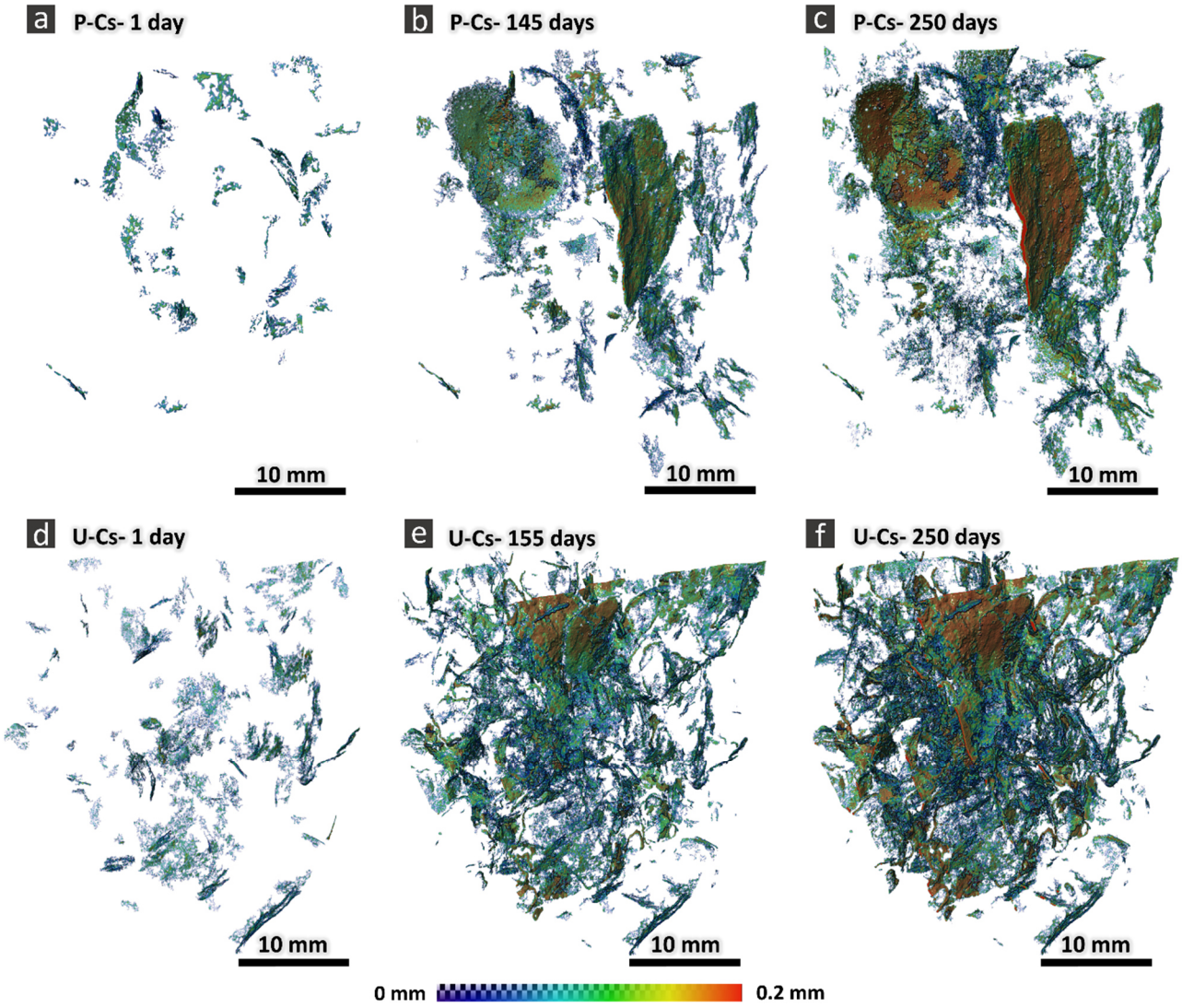

Figure S 50. Same figure as Figure S 49 but for the P-Cs specimen, insets (a) - (b), at 1 day, 145 and 250 days, respectively, and for the U-Cs one, insets (d)-(f), at 1 day, 155 and 250 days, respectively.

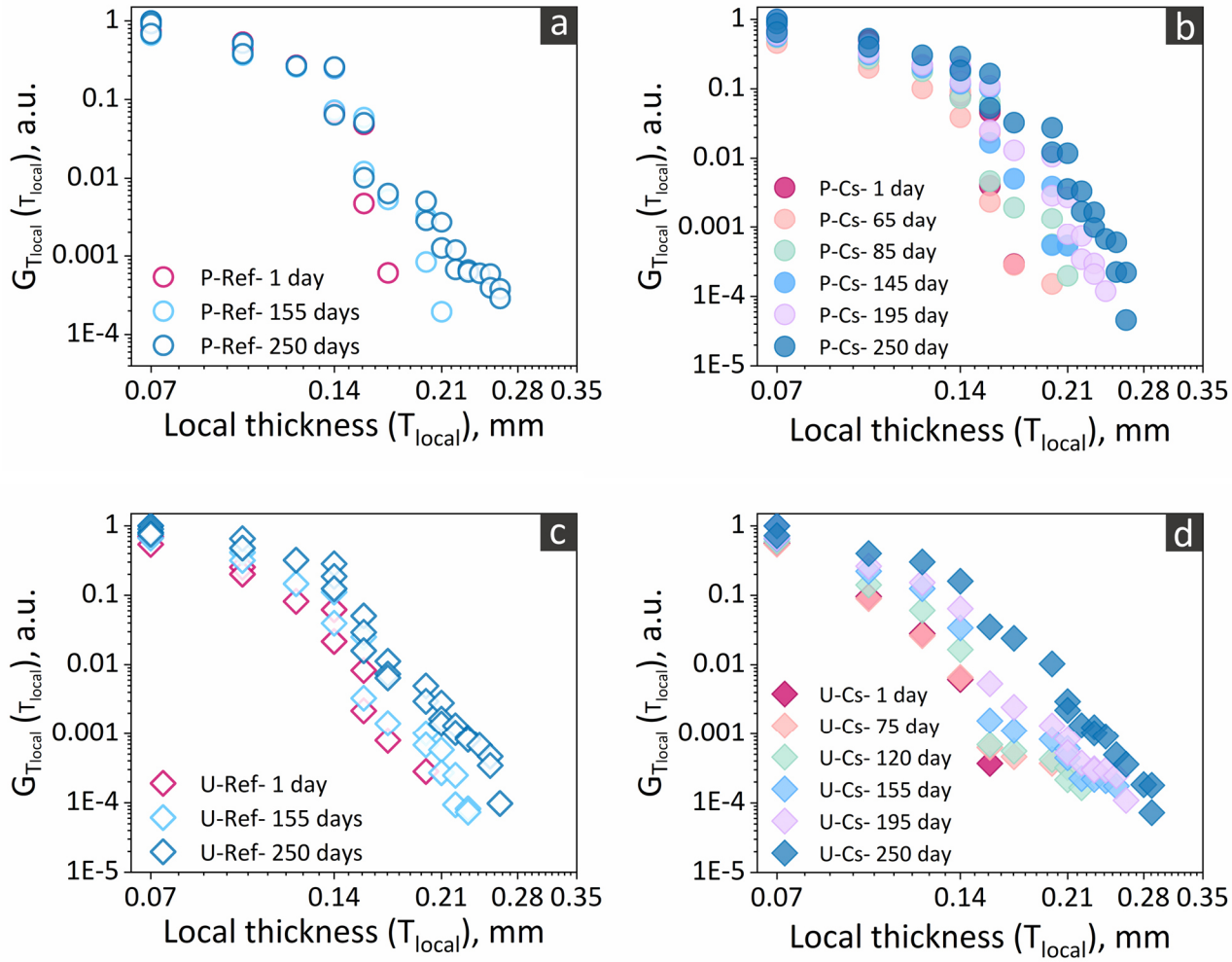

Figure S 51. Empirical (i.e., statistical ensemble) complementary cumulative distribution function of the total crack network's local thickness, $T_{local}(\vec{x})$, $G_{\mathbb{T}_{local}}(T_{local})$, in log_{10}-log_{10} scales (Zip'f plot) (a) P-Ref, (b) P-Cs, (c) U-Ref and (d) U-Cs specimens, respectively, at various time points specified on the corresponding plots.

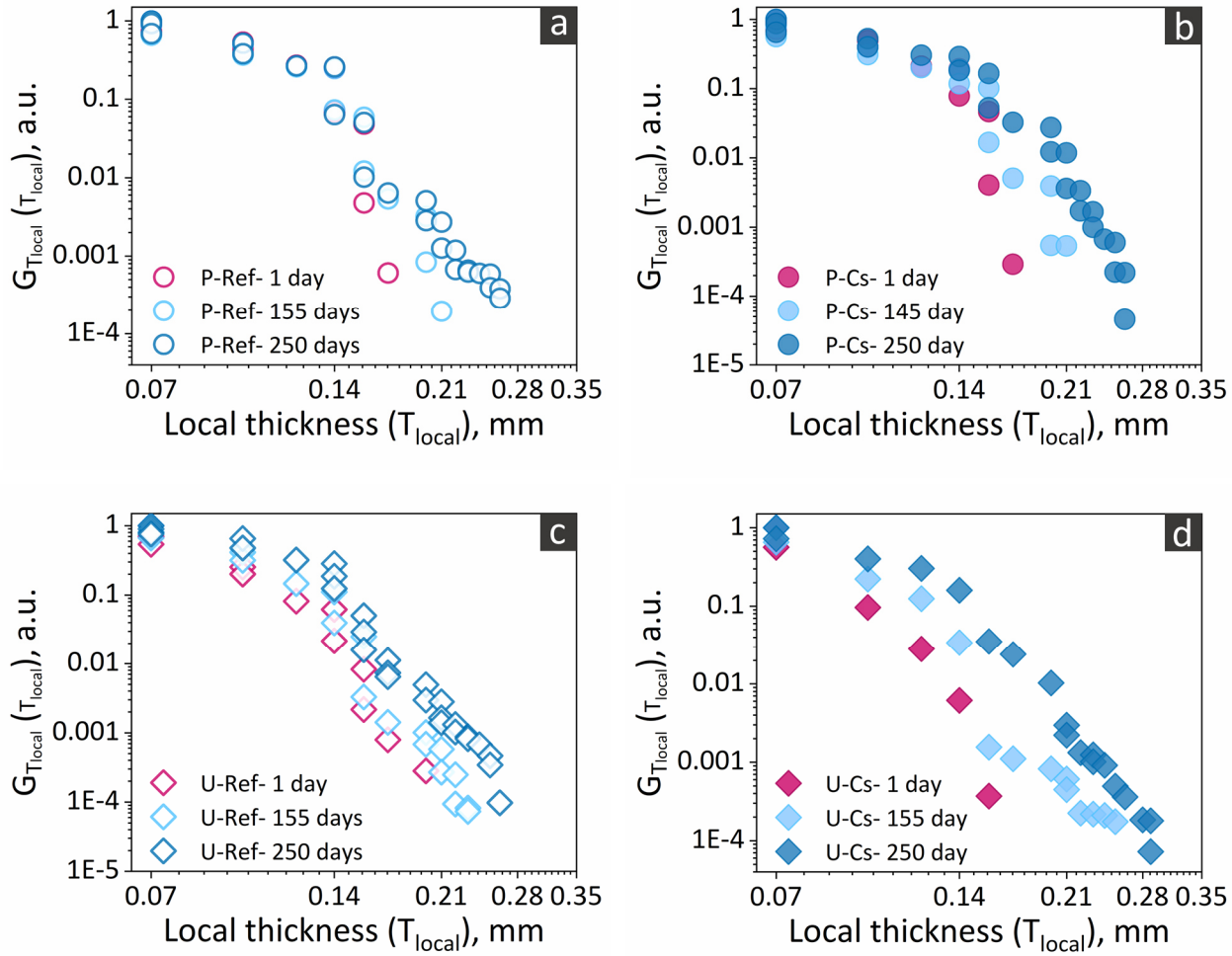

Figure S 52. Similar to Figure S 51, but comparing only three time points for each specimen.

S11. Quantitative analysis of ASR cracking by time-lapse tomography. Local deformations analysis.

In this Section, we report further visualizations, both of 2D cross-sections and of smaller sub-volumes, of the two scalar fields, $\|\vec{u}_{N-AFF}\|(\vec{x}, t_i)$ and $J_{\vec{T}_{N-AFF}}(\vec{x}, t_i)$, which we used as 3D maps of where and how the displacement vector due to the ASR deformations was spatially heterogeneous. Both scalar fields, as mentioned in Section S3.6 above, are derived from the displacement vector field, $\vec{u}_{N-AFF}(\vec{x}, t_i)$, generated by the non-affine registration procedure.

We remind the reader that such displacement vector field is not the total one due to the ASR deformations. Rather, it is only its component having a spatial dependence, the other component being the one computed from the global affine registration procedure. We also note that the total displacement vector field due to the ASR deformations is not simply the sum of the two fields just mentioned, rather a more complicated nonlinear function of the two. However, from a qualitative point of view, the global

affine field captures the overall, bulk effect of the ASR deformations, while the non-affine one describes their local details.

The visualizations in this Section aim at providing examples additional to those shown in Section 3.6 of the article, concerning the most relevant features of the ASR-induced local deformations. These examples also aim at showing that such features were observed in both the specimens with the P aggregates and in those with the U ones and were essentially independent from the presence or absence of the Cs-doping, except for the different timing at which they appeared.

P-Ref and U-Ref specimens

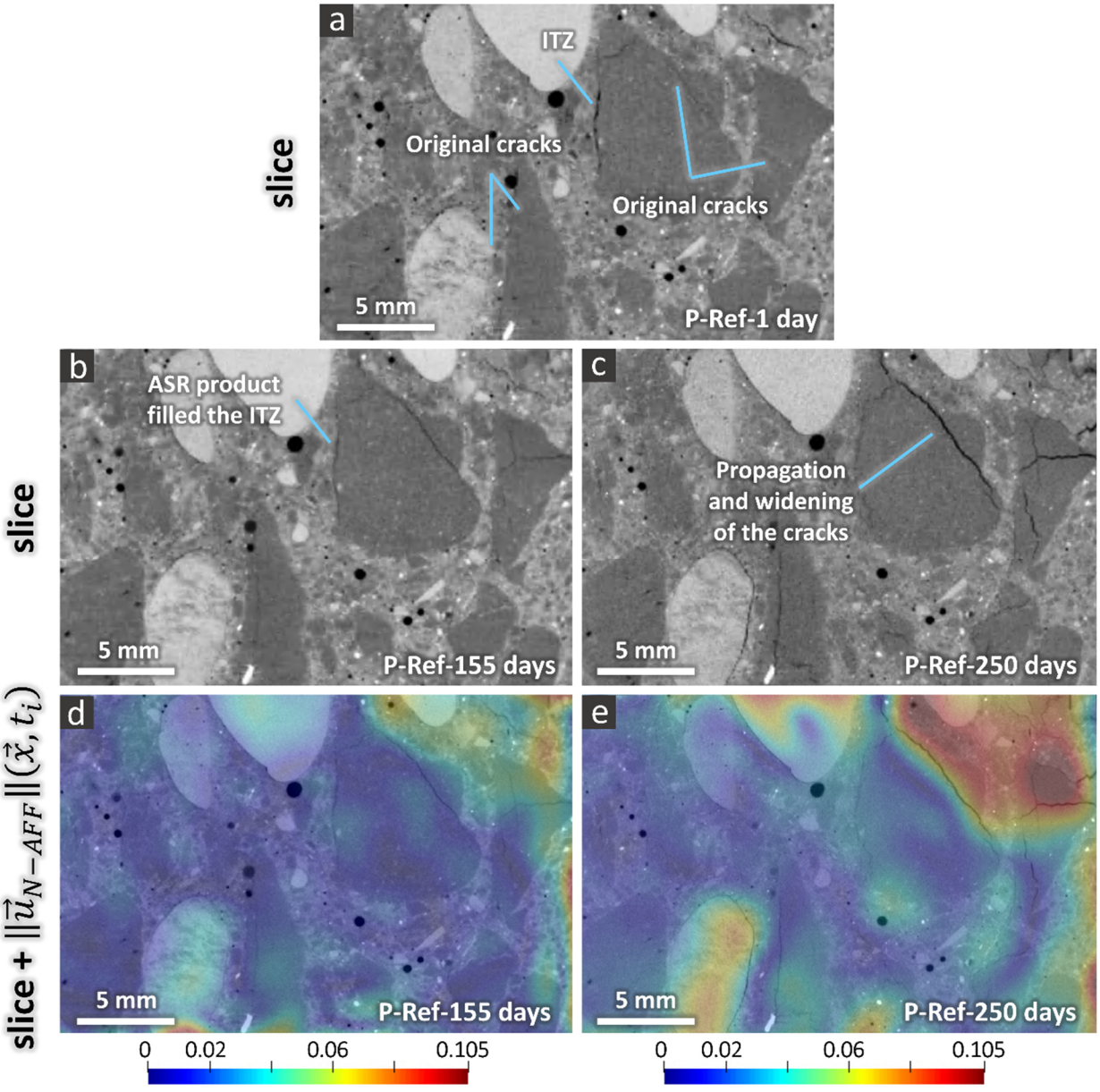

Figure S 53. Visualization of the magnitude of the displacement vector field, $\|\vec{u}_{N-AFF}\|(\vec{x},t_i)$, associated with the transformation vector field, $\vec{T}_{N-AFF}(\vec{x},t_i)$, of the non-affine registration, for the P-Ref

specimen. The scalar field $\|\vec{u}_{N-AFF}\|(\vec{x},t_i)$ is used as spatial map of the "degree of local heterogeneity" of the ASR deformation. In this figure, only one 2D cross-section from the "tomographed" volume is shown. (a) X-ray tomogram of the P-Ref specimen at the beginning of the ASR acceleration (1 day) and shown only at the position of the chosen 2D cross-section ("slice"). (b) and (c): slice from the X-ray tomograms at 155 and 250 days, respectively. (d) and (e): the same slices as in (b) and (c), respectively, plus, overlapped on top of them semi-transparently and rendered according to the indicated color scale, the 2D cross-section, at the same position, from $\|\vec{u}_{N-AFF}\|(\vec{x},t_i)$, at 155 and 250 days, respectively. The color scale bars of insets (d) and (e) are in units of mm.

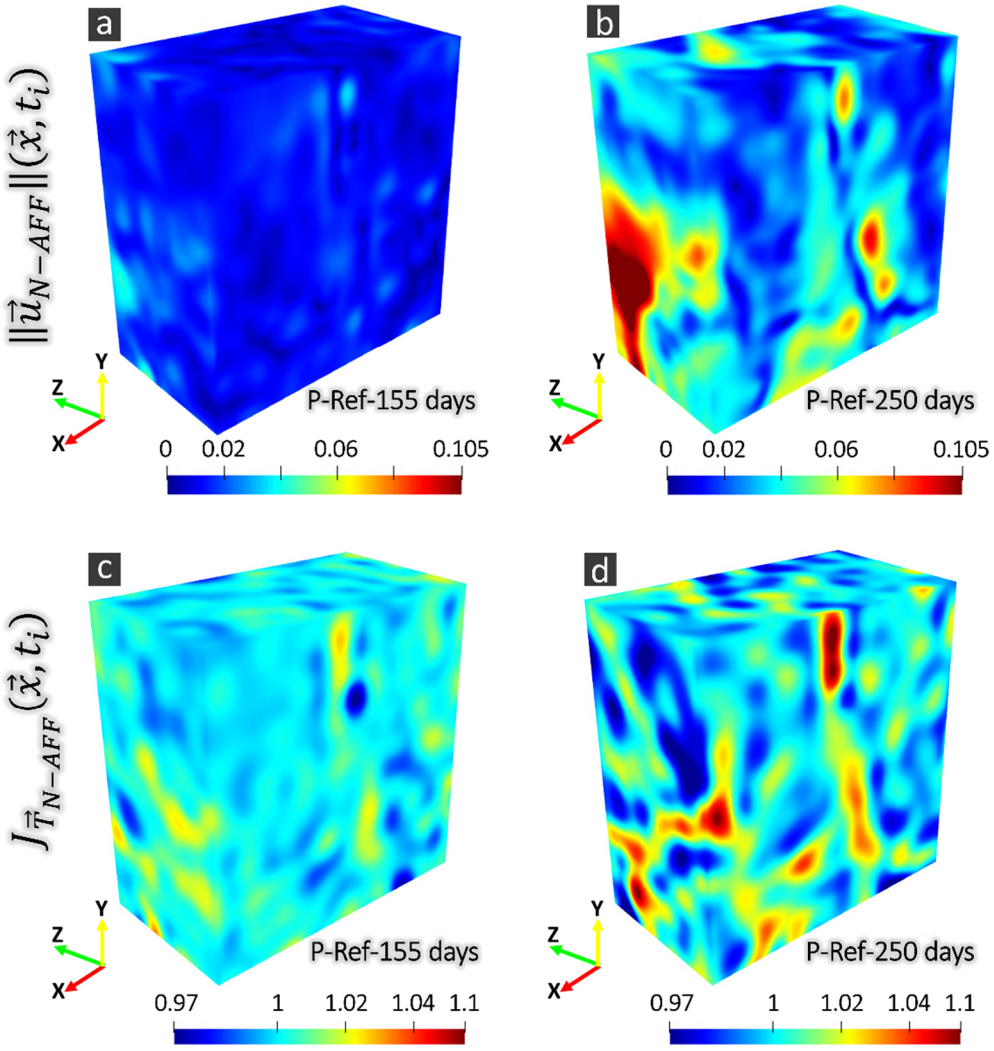

Figure S 54. 3D Visualization of the two scalar fields computed from the displacement vector field, $\vec{u}_{N-AFF}(\vec{x},t_i)$, associated with the non-affine transformation vector field, $\vec{T}_{N-AFF}(\vec{x},t_i)$, obtained from the non-affine registration and used as indicators of the spatially heterogeneous component of the overall displacement due to the ASR deformations. Case of the P-Ref specimen. Each scalar field

is shown on the boundary surfaces of a parallelepiped ROI smaller than the "tomographed" volume of the specimen and it is color-coded. (a) and (b): the scalar field is the magnitude of $\vec{u}_{N-AFF}(\vec{x}, t_i)$, $\|\vec{u}_{N-AFF}\|(\vec{x}, t_i)$. *(c) and (d): the scalar field is the determinant of the Jacobian matrix of* $\vec{T}_{N-AFF}(\vec{x}, t_i)$, $J_{\vec{T}_{N-AFF}}(\vec{x}, t_i)$. *(a) and (c) refer to the time point* t_2*= 155 days. (b) and (d) refer to* t_2*= 250 days. In insets (a) and (b) the unit for the color scale bars is mm. The color scale bars of (c) and (d) have no unit because of the meaning of* $J_{\vec{T}_{N-AFF}}(\vec{x}, t_i)$ *of a volumetric ratio. Values greater than 1 represent volumetric expansion while smaller than 1 indicate volumetric contraction.*

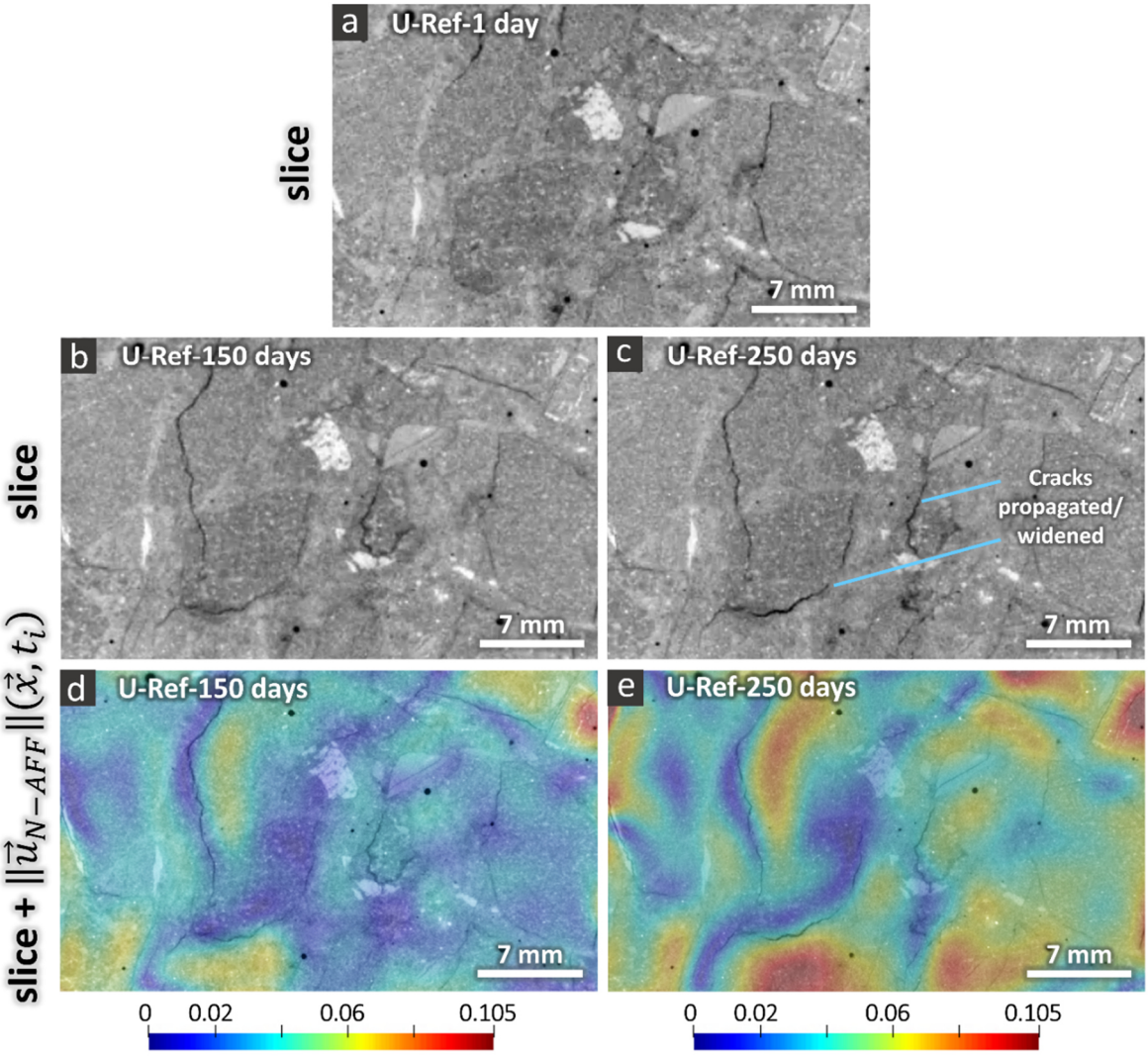

Figure S 55. Similar visualization of $\|\vec{u}_{N-AFF}\|(\vec{x}, t_i)$ *as in Figure S 53 but for the U-Ref specimen. (a): tomographic slice at 1 day. (b) and (c): the same tomographic slices at 155 and 250 days, respectively. (d) and (e): the same tomographic slices as in (b) and (c) plus, overlapped on top of them semi-transparently and according to the color scale indicated below, the values of* $\|\vec{u}_{N-AFF}\|(\vec{x}, t_i)$ *on the same plane as the one of the tomographic slice and at the respective time points. In (d) and (e) the unit for the color scale bars is mm.*

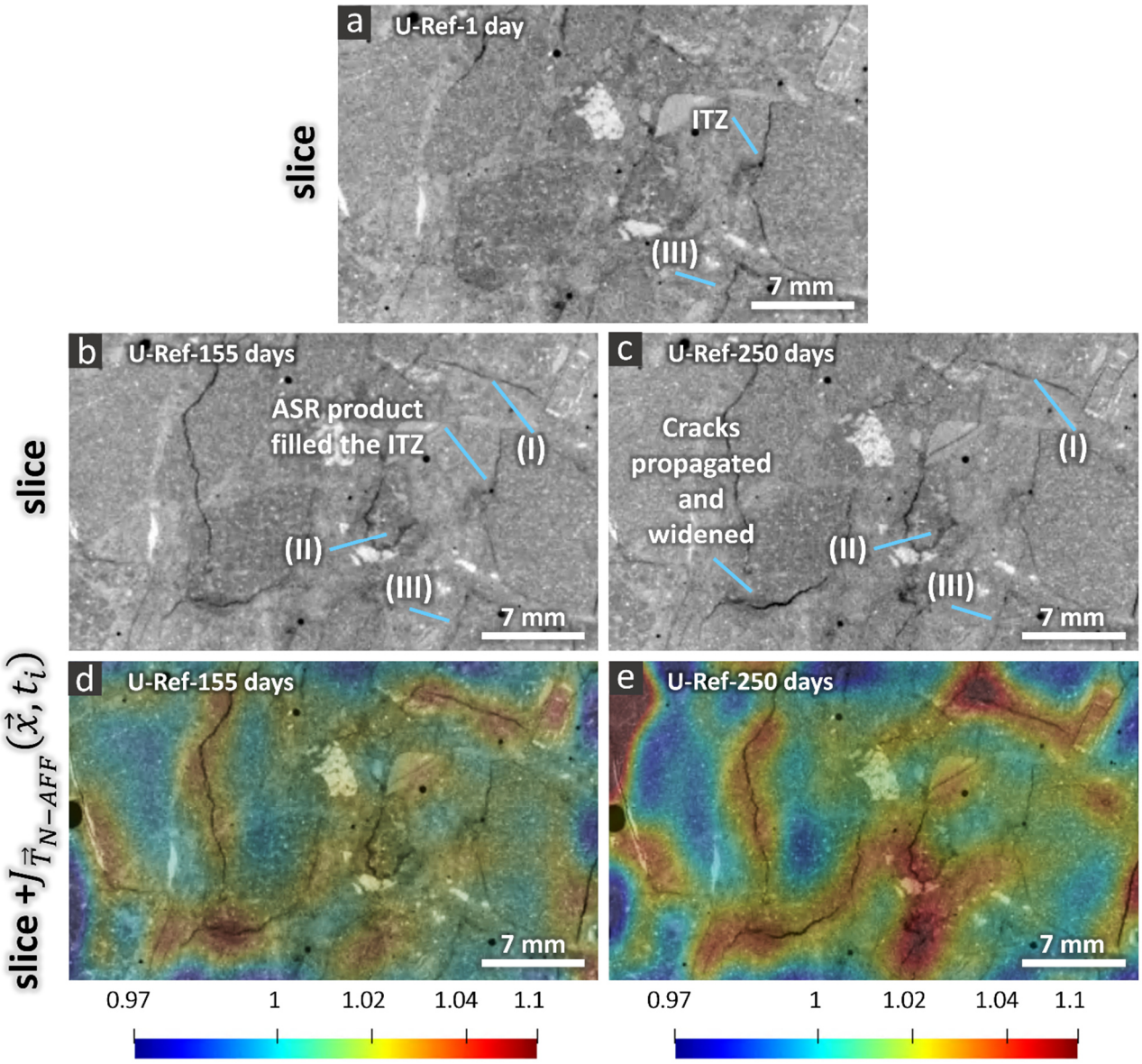

Figure S 56. Similar plots as in Figure 10 within the article but for the U-Ref specimen. Features (I) and (II) refer to the enlargement (opening) of cracks (zones of high expansion, appearing in red in the $J_{\vec{T}_{N-AFF}}$ map far away from the cracks). Feature labelled by (III) indicate original crack or more porous regions at the aggregate boundaries that did not evolve into an opening and lengthening crack, rather they either remained the same or gradually got closed or filled up.

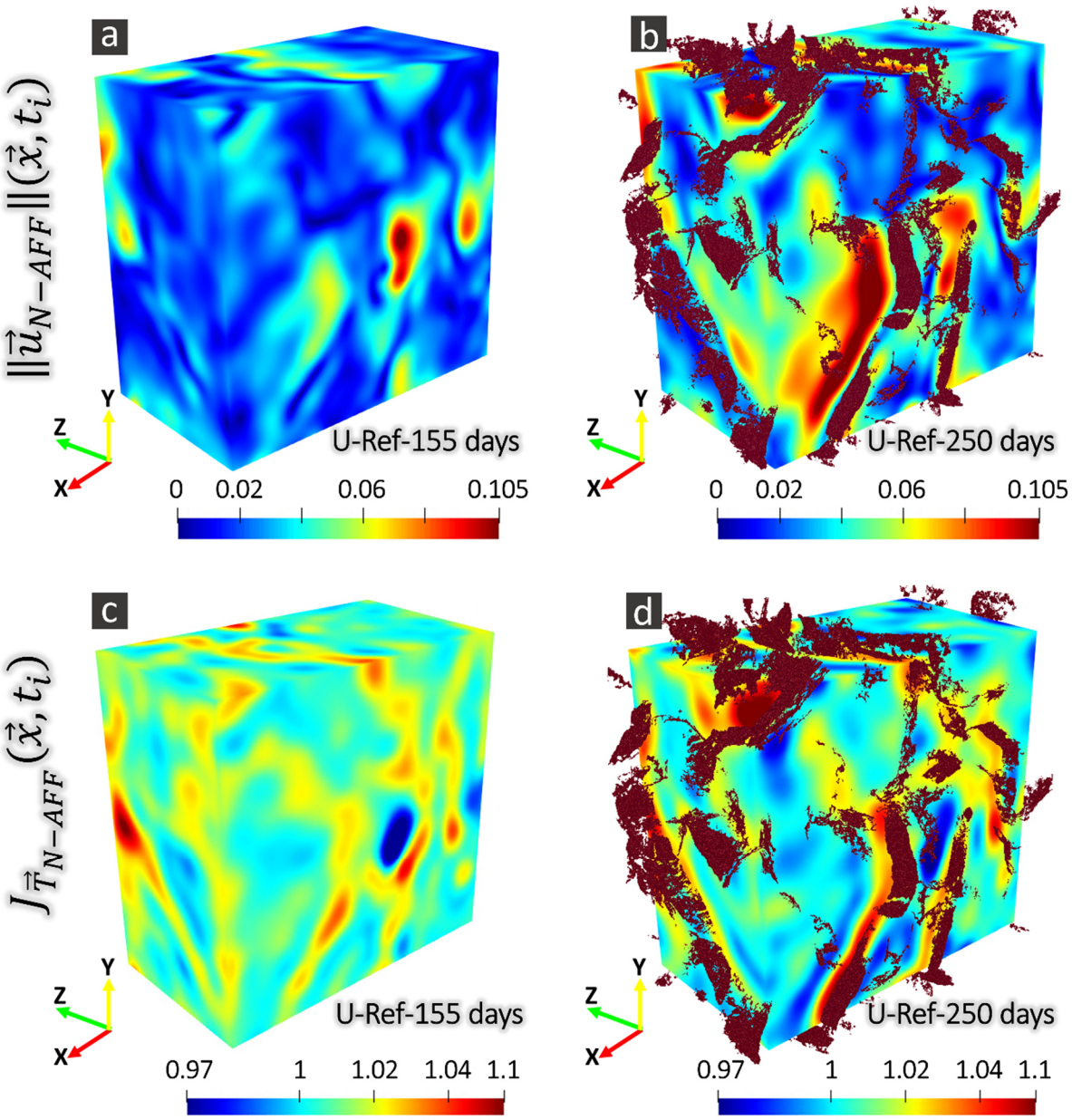

Figure S 57. Similar figure as Figure S 54 but for the U-Ref specimen. In insets (b) and (d), in addition to the visualization of the two scalar fields, the same small 3R ROI but extracted from the binary tomogram of the segmented total crack network is rendered in dark red solid color in order to show where the crack network was inside such ROI, in comparison with the spatial distribution of the two scalar fields indicating spatially heterogeneous deformations.

P-Cs and U-Cs specimens

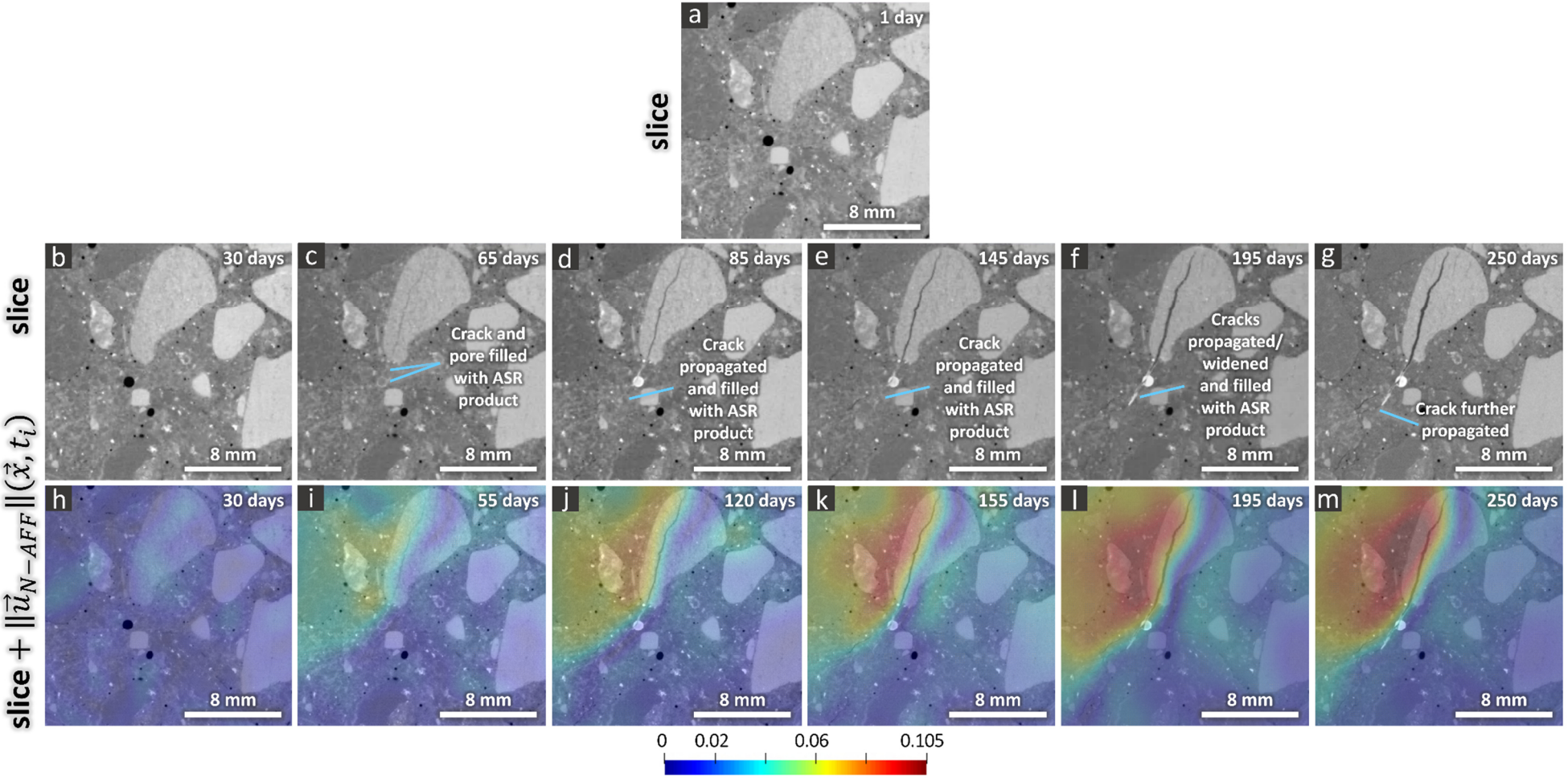

Figure S 58. Similar visualization of $\|\vec{u}_{N-AFF}\|(\vec{x}, t_i)$ as in Figure S 53 or Figure S 55 but for the P-Cs specimen at 7 different time points (1day, 30, 65, 85, 145, 195 and 250 days).

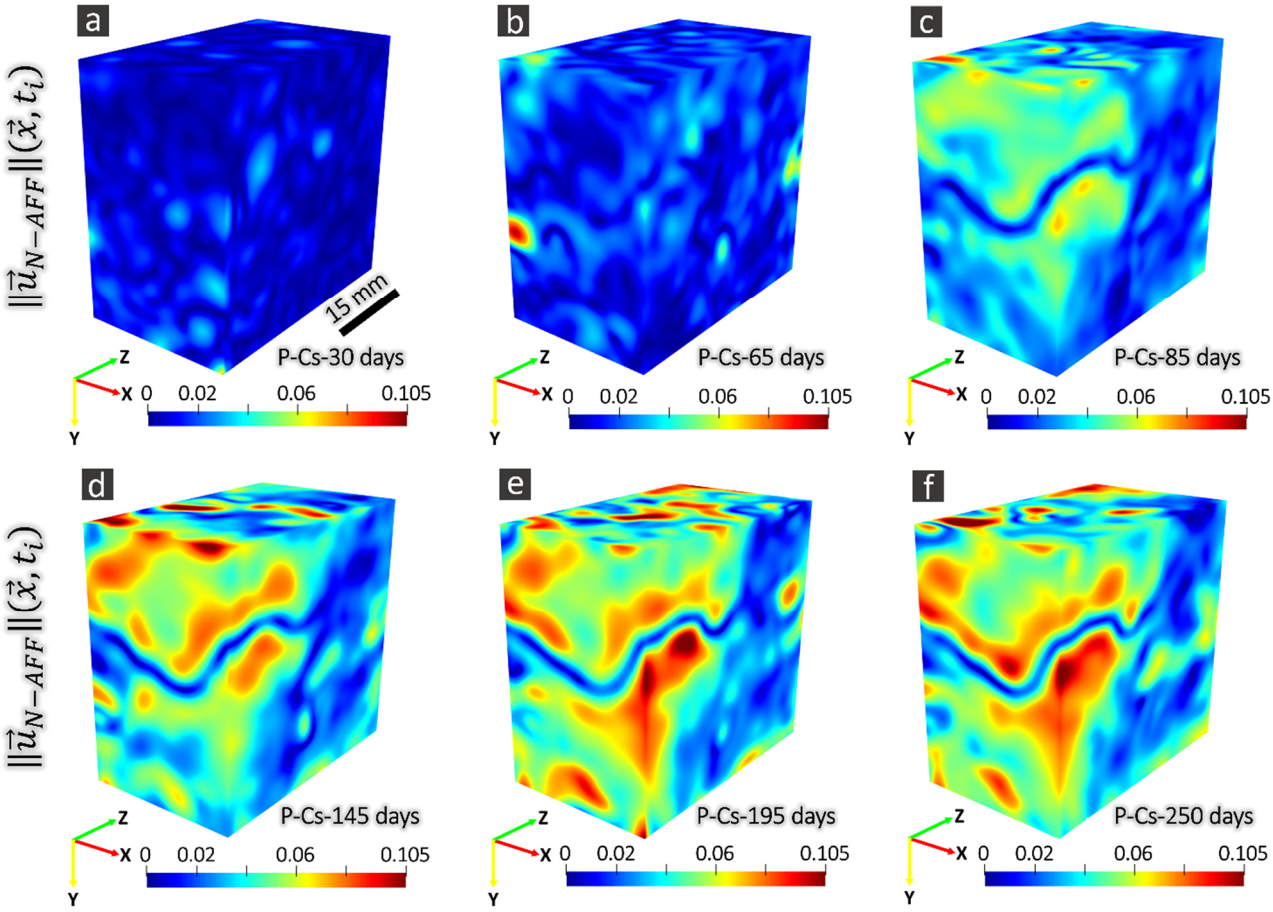

Figure S 59. Visualization of the magnitude of $\vec{u}_{N-AFF}(\vec{x},t_i)$, $\|\vec{u}_{N-AFF}\|(\vec{x},t_i)$, computed from the displacement vector field, $\vec{u}_{N-AFF}(\vec{x},t_i)$, associated with the non-affine transformation vector field, $\vec{T}_{N-AFF}(\vec{x},t_i)$, obtained from the non-affine registration and used as indicator of the spatially heterogeneous component of the overall displacement due to the ASR deformations. Case of the P-Cs specimen. The scalar field is shown on the boundary surfaces of a parallelepiped ROI smaller than the tomographed volume of the specimen and it is color-coded. The insets (a) to (f) show $\|\vec{u}_{N-AFF}\|(\vec{x},t_i)$ at 6 different time points when the specimen was tomographed, including 1 day 30, 65, 85, 145, 195 and 250 days. In all the insets the unit for the color scale bar is mm.

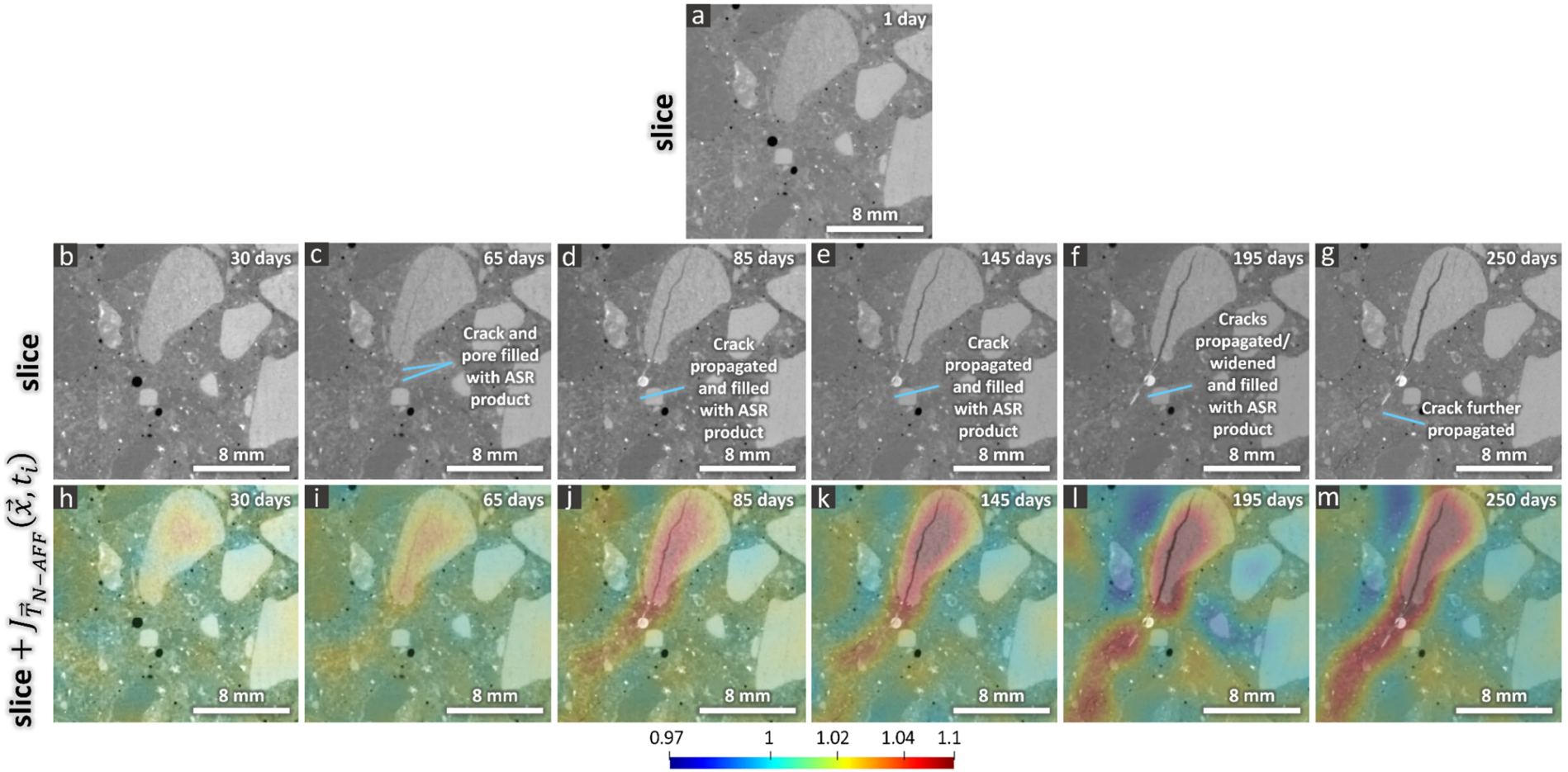

Figure S 60. Visualization of the determinant of the Jacobian matrix of $\vec{T}_{N-AFF}(\vec{x}, t_i)$, $J_{\vec{T}_{N-AFF}}(\vec{x}, t_i)$. This scalar field is used as spatial map of the factor by which the volume locally expanded or contracted. In this figure, only one 2D cross-section from the tomographed volume is shown. This figure is an extended version of Figure 11 within the article. (a) X-ray tomogram of the P-Cs specimen at the beginning of the ASR acceleration (1 day), shown only at the position of the chosen 2D cross-section ("slice"). (b) to (g): slices from the X-ray tomograms at 30, 65, 85, 145, 195 and 250 days, respectively. (h) to (m): the same slices as in (b) to (g), respectively, plus, overlapped on top of them semi-transparently and rendered according to the indicated color scale, the slice, at the same position, from $J_{\vec{T}_{N-AFF}}(\vec{x}, t_i)$, at the same corresponding time points. The color scale bar of insets (h) to (m) has no unit. $J_{\vec{T}_{N-AFF}}$ values greater than 1 represent volumetric expansion, values smaller than 1 mean volumetric contraction.

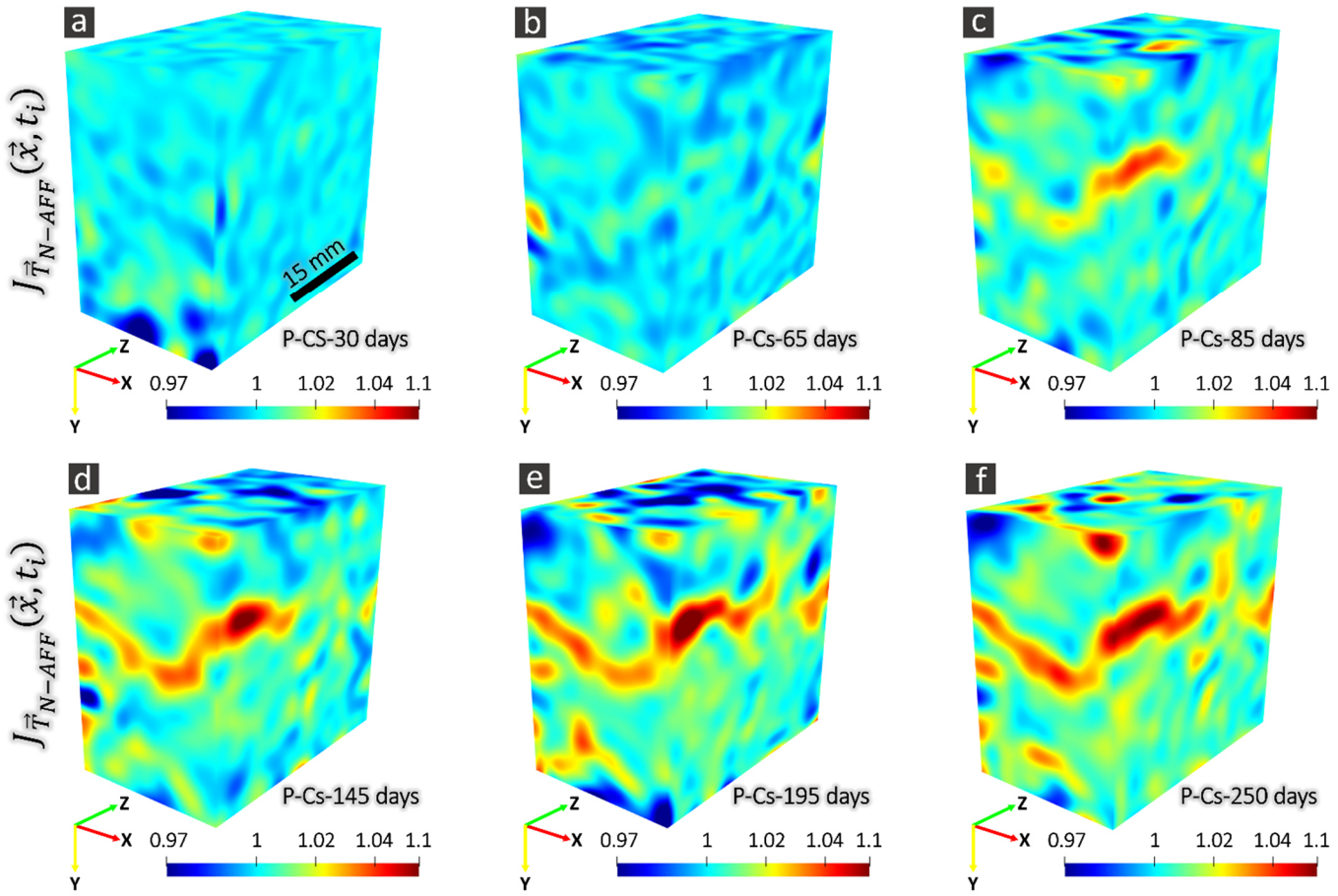

Figure S 61. 3D Visualization of the determinant of the Jacobian matrix of $\vec{T}_{N-AFF}(\vec{x}, t_i)$, $J_{\vec{T}_{N-AFF}}(\vec{x}, t_i)$, computed from the displacement vector field, $\vec{u}_{N-AFF}(\vec{x}, t_i)$, associated with the non-affine transformation vector field, $\vec{T}_{N-AFF}(\vec{x}, t_i)$, obtained from the non-affine registration and used as indicator of the spatially heterogeneous component of the overall displacement due to the ASR deformations. Case of the P-Cs specimen. The scalar field is shown on the boundary surfaces of a parallelepiped ROI smaller than the tomographed volume of the specimen and it is color-coded. (a) to (f): time points of 30, 65, 85, 145, 195 and 250 days, respectively. The scale bars of all insets have no unit. $J_{\vec{T}_{N-AFF}}$ values greater than 1 correspond to volumetric expansion, values smaller than 1 to volumetric contraction.

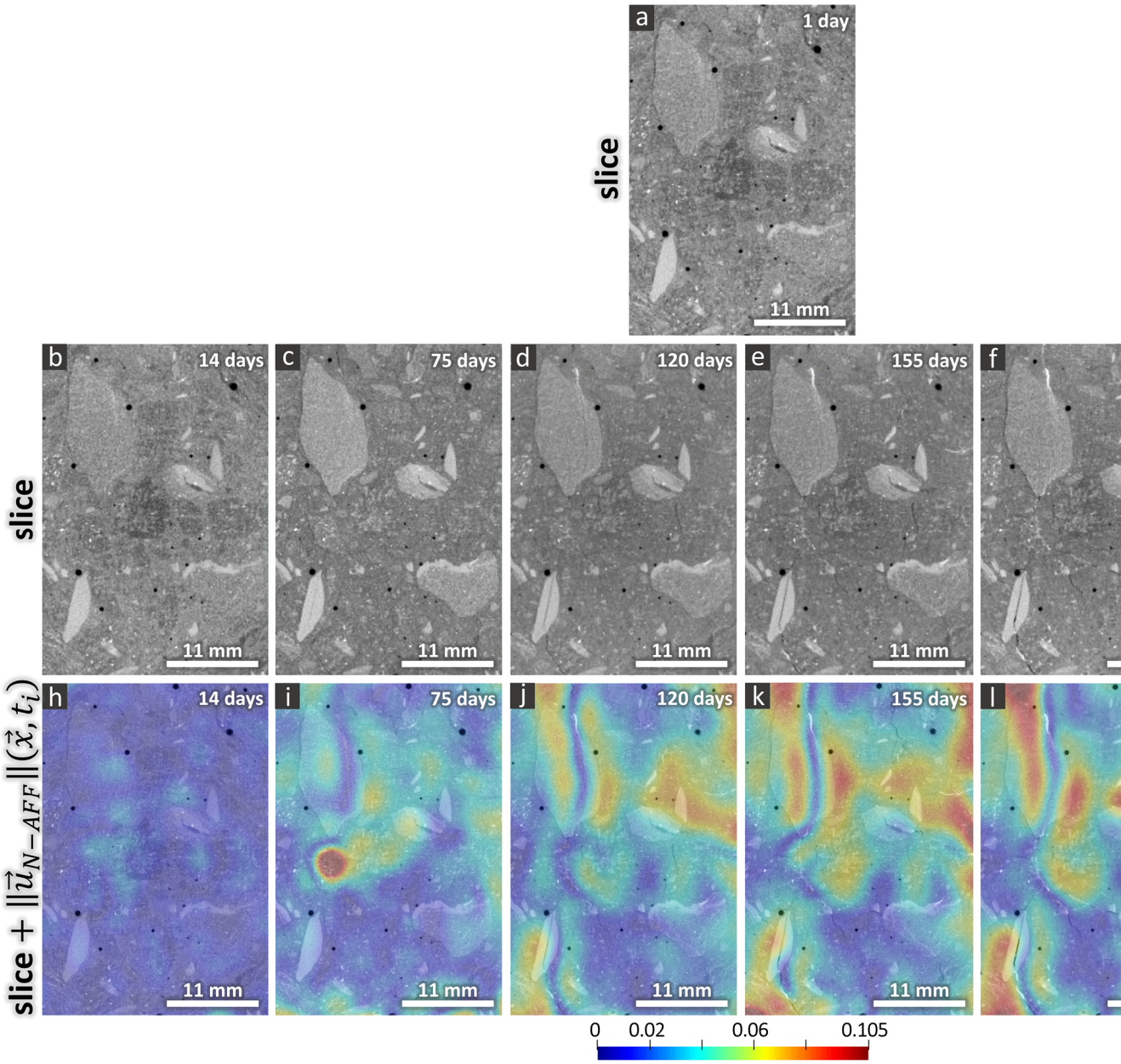

Figure S 62. Similar figure as Figure S 58 but for the U-Cs speci

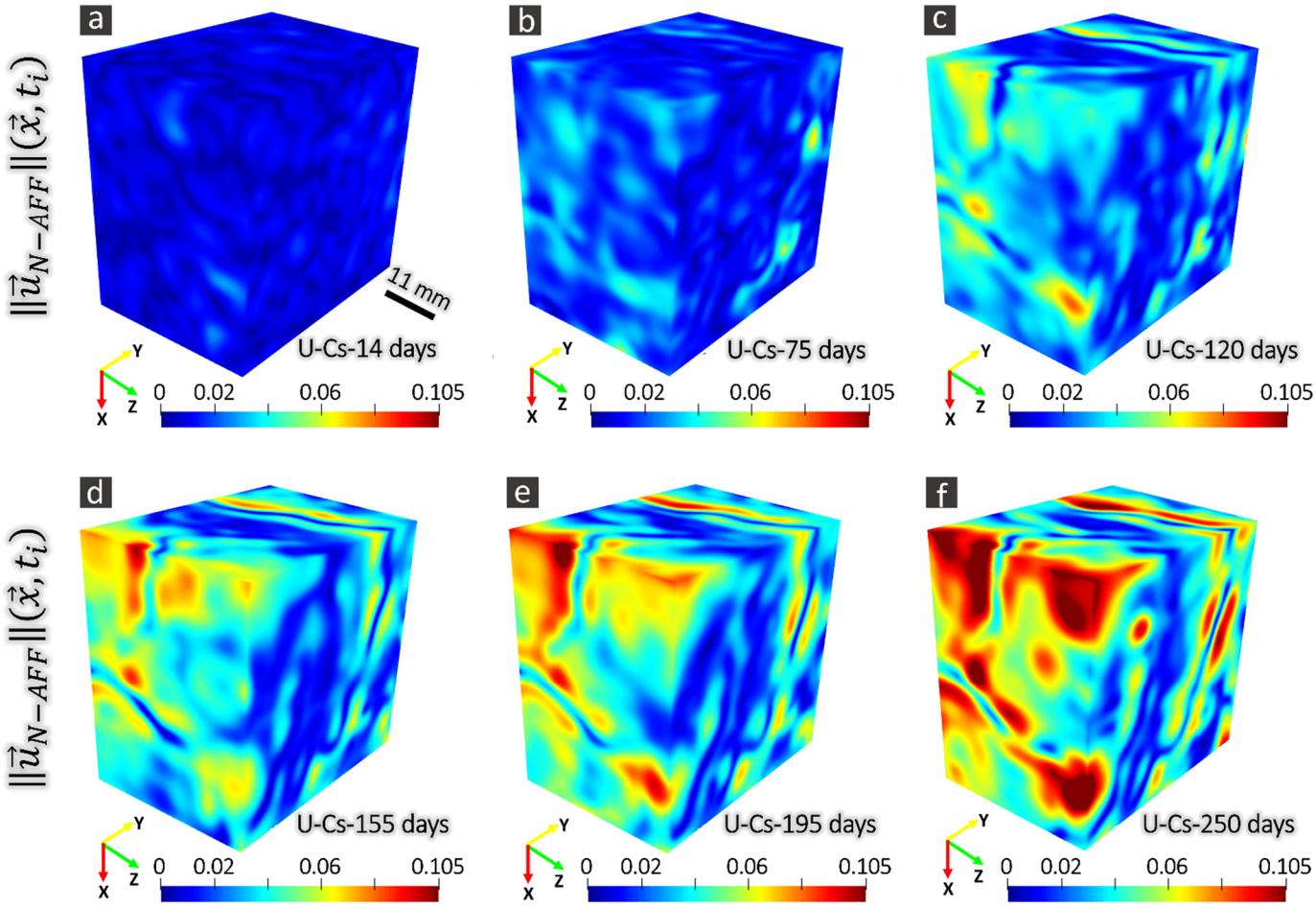

Figure S 63. Similar figure as Figure S 59 but for the U-Cs specimen.

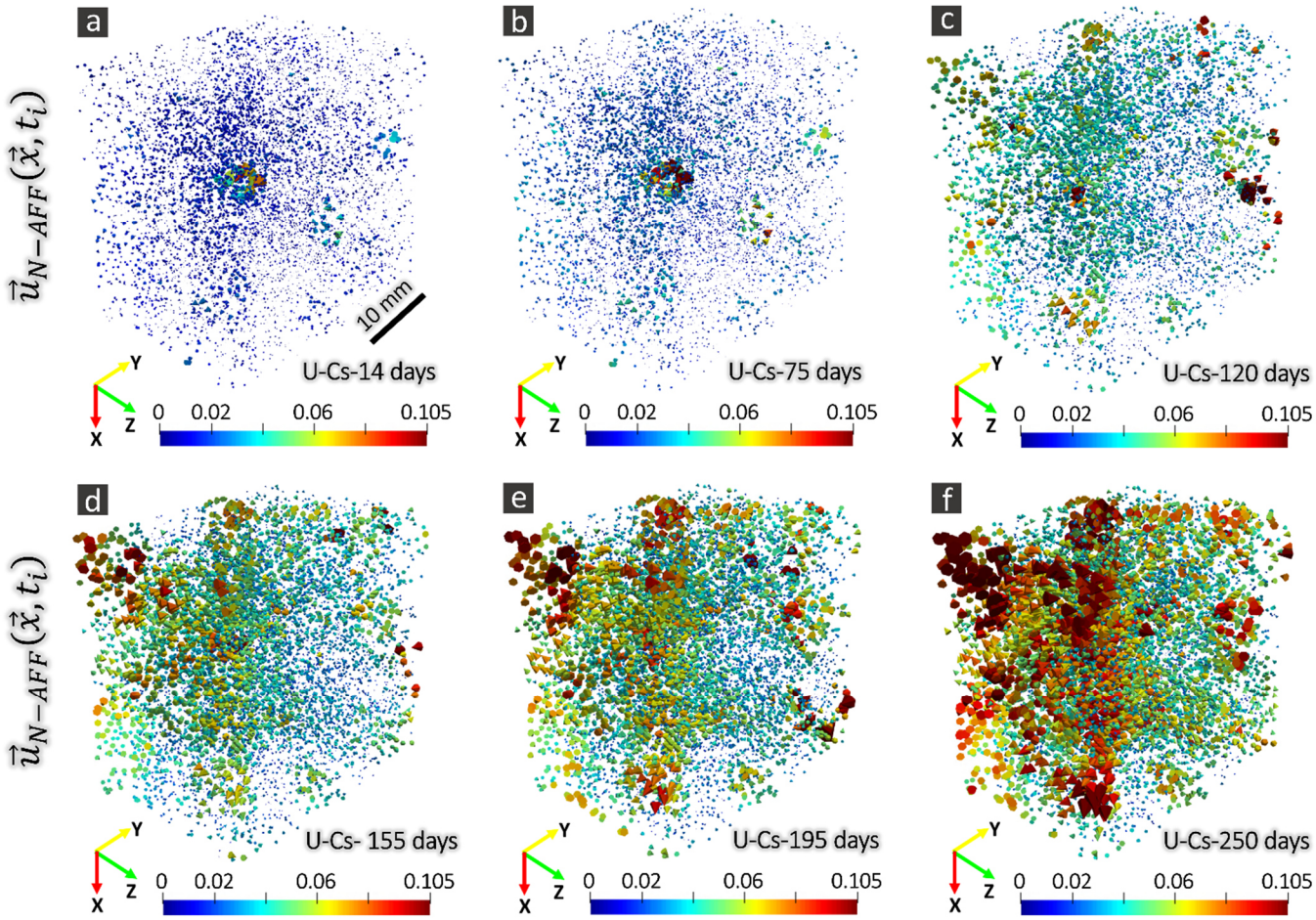

Figure S 64. Similar figure as Figure S 63 but showing this time the whole $\vec{u}_{N-AFF}(\vec{x}, t_i)$ vector field itself for the P-Cs specimen. $\vec{u}_{N-AFF}(\vec{x}, t_i)$ is represented by conic glyphs rendered at some voxel positions. The size and color of the glyphs represent the corresponding $\|\vec{u}_{N-AFF}\|(\vec{x}, t_i)$ values. In all insets, the unit for the color scale bar is mm.

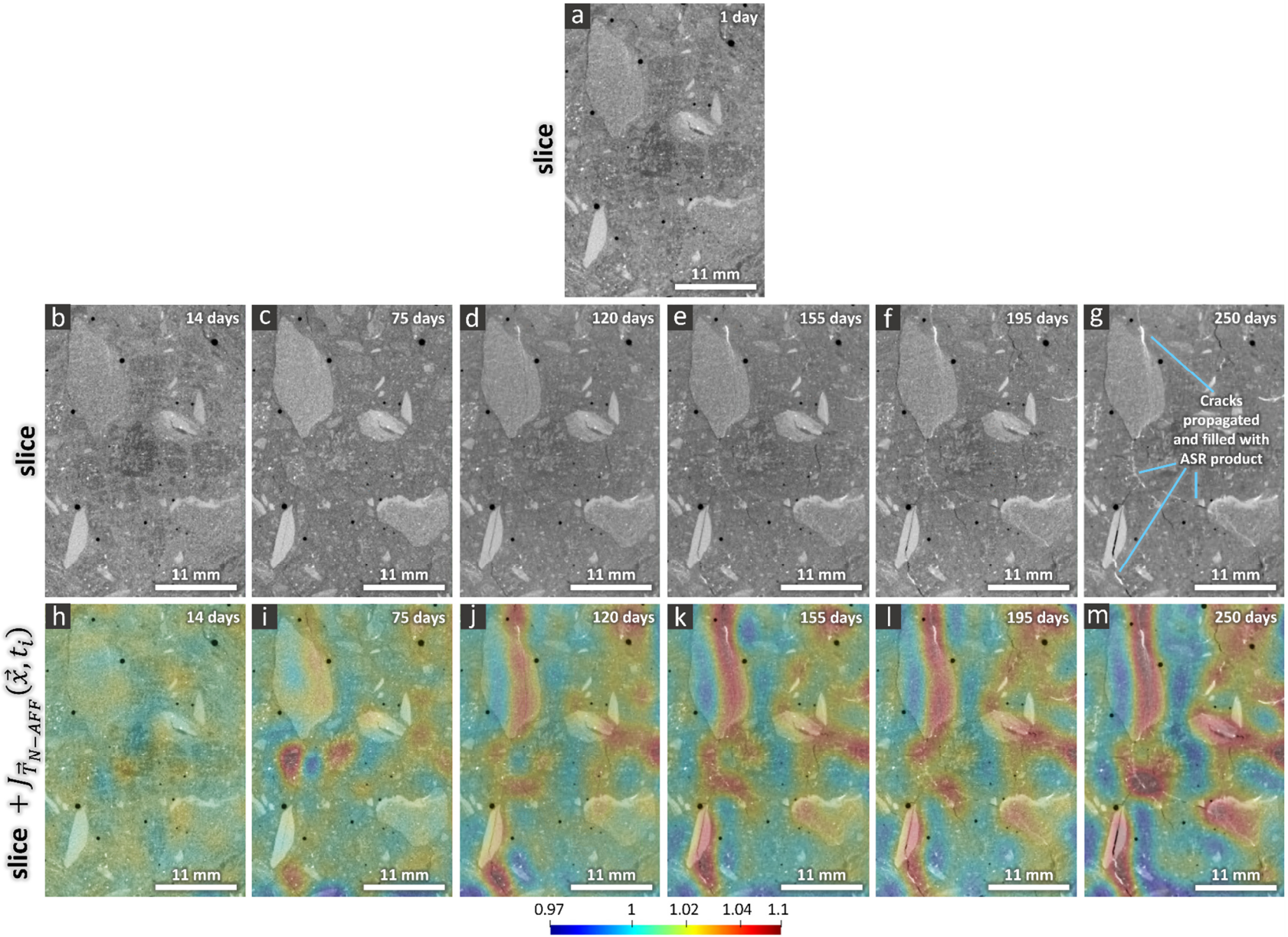

Figure S 65. Similar figure as Figure S 60 but for the U-Cs specimen.

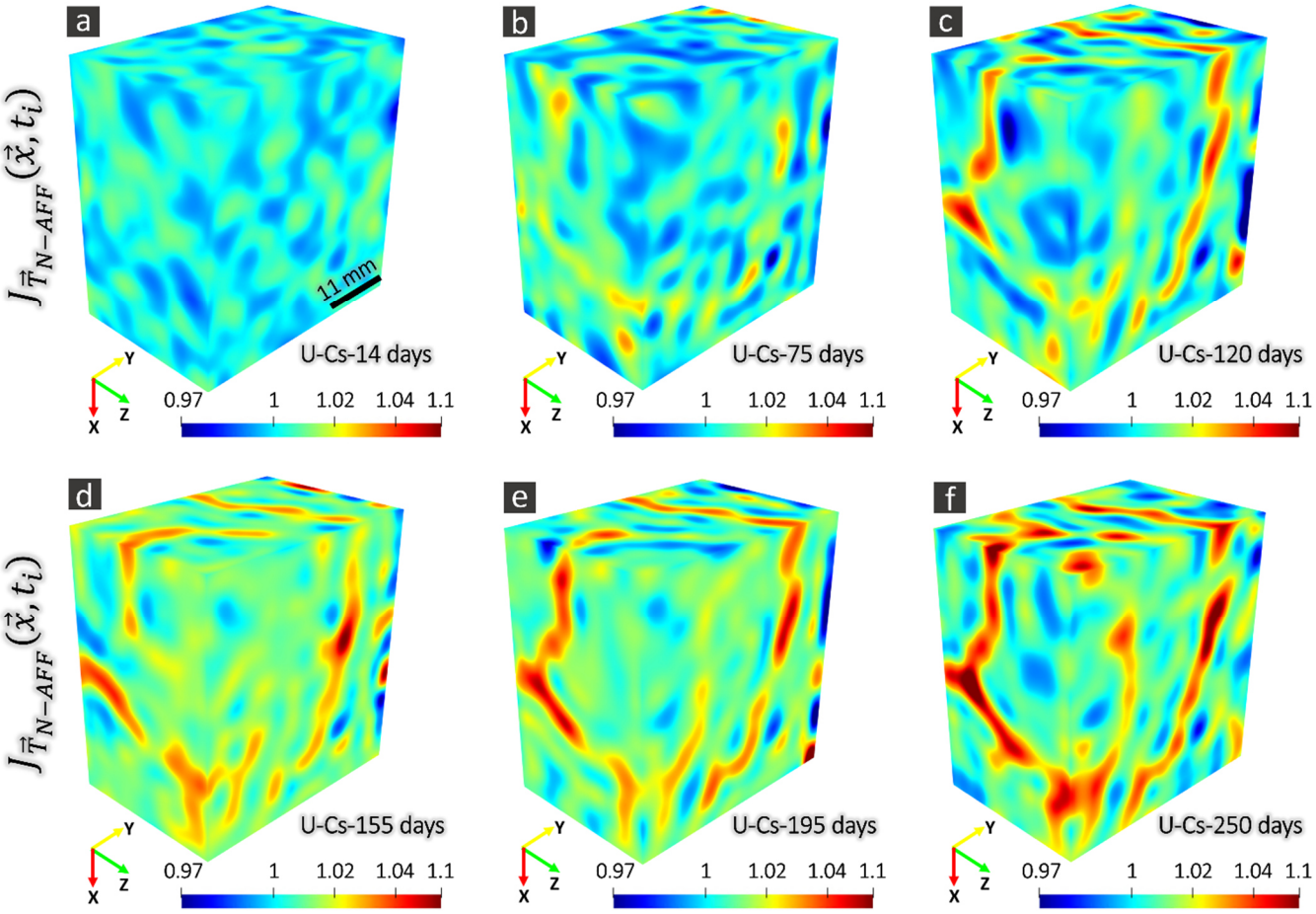

Figure S 66. Similar figure as Figure S 61 but for the U-Cs specimen.

References

[1] “DIN EN 196-2 : 2013 | METHOD OF TESTING CEMENT - PART 2: CHEMICAL ANALYSIS OF CEMENT | SAI Global.” [Online]. Available: https://infostore.saiglobal.com/en-us/Standards/DIN-EN-196-2-2013-386164_SAIG_DIN_DIN_877353/. [Accessed: 11-Nov-2020].

[2] “ISO - ISO 10694:1995 - Soil quality — Determination of organic and total carbon after dry combustion (elementary analysis).” [Online]. Available: https://www.iso.org/standard/18782.html. [Accessed: 11-Nov-2020].

[3] I. Fernandes *et al.*, “Alkali-silica reactivity of some common rock types. A global petrographic atlas,” *Q. J. Eng. Geol. Hydrogeol.*, vol. 46, no. 2, pp. 215–220, May 2013, doi: 10.1144/qjegh2012-065.

[4] D. De Paiva Gomes Neto, H. Conceição, V. A. C. Lisboa, R. S. De Paiva Santana, and L. S. Barreto, “Influence of granitic aggregates from Northeast Brazil on the alkali-aggregate reaction,” *Mater. Res.*, vol. 17, pp. 51–58, Aug. 2014, doi: 10.1590/S1516-14392014005000045.

[5] A. Leemann and B. Münch, “The addition of caesium to concrete with alkali-silica reaction: Implications on product identification and recognition of the reaction sequence,” *Cem. Concr. Res.*, vol. 120, pp. 27–35, Jun. 2019, doi: 10.1016/j.cemconres.2019.03.016.

[6] A. V. Bronnikov, “Cone-beam reconstruction by backprojection and filtering,” *J. Opt. Soc. Am. A*, vol. 17, no. 11, p. 1993, Nov. 2000, doi: 10.1364/josaa.17.001993.

[7] “SIA 2042 NOTICE | Prevention of damage from the alkali | SNV.” [Online]. Available: https://shop.snv.ch/Technische-Regel/Diverses/SIA-2042-MERKBLATT.html. [Accessed: 11-Nov-2020].

[8] D. Tschumperlé and R. Deriche, “Anisotropic Diffusion Partial Differential Equations for Multichannel Image Regularization: Framework and Applications,” *Advances in Imaging and Electron Physics*, vol. 145, no. SUPPL. pp. 149–209, 2007, doi: 10.1016/S1076-5670(06)45004-7.

[9] B. Münch, “Xlib (ImageJ / Fiji plugins),” *ImageJ*, 2019. [Online]. Available: https://imagej.net.

[10] C. A. Schneider, W. S. Rasband, and K. W. Eliceiri, “NIH Image to ImageJ: 25 years of image analysis,” *Nature Methods*, vol. 9, no. 7. Nat Methods, pp. 671–675, Jul-2012, doi: 10.1038/nmeth.2089.

[11] B. Zitová and J. Flusser, “Image registration methods: A survey,” *Image Vis. Comput.*, vol. 21, no. 11, pp. 977–1000, Oct. 2003, doi: 10.1016/S0262-8856(03)00137-9.

[12] K. Marstal, F. Berendsen, M. Staring, and S. Klein, “SimpleElastix: A user-friendly, multi-lingual library for medical image registration.”

[13] B. C. Lowekamp, D. T. Chen, L. Ibáñez, and D. Blezek, “The Design of SimpleITK,” *Front. Neuroinform.*, vol. 7, 2013, doi: 10.3389/fninf.2013.00045.

[14] A. Nan, M. Tennant, U. Rubin, and N. Ray, “DRMIME: Differentiable Mutual Information and Matrix Exponential for Multi-Resolution Image Registration,” PMLR, Sep. 2020.

[15] S. Klein, M. Staring, K. Murphy, M. A. Viergever, and J. P. W. Pluim, “Elastix: A toolbox for intensity-

based medical image registration," *IEEE Trans. Med. Imaging*, vol. 29, no. 1, pp. 196–205, Jan. 2010, doi: 10.1109/TMI.2009.2035616.

[16] R. Hagege and J. M. Francos, "Parametric estimation of affine transformations: An exact linear solution," *J. Math. Imaging Vis.*, vol. 37, no. 1, pp. 1–16, May 2010, doi: 10.1007/s10851-009-0188-4.

[17] A. Sotiras, C. Davatzikos, and N. Paragios, "Deformable medical image registration: A survey," *IEEE Trans. Med. Imaging*, vol. 32, no. 7, pp. 1153–1190, 2013, doi: 10.1109/TMI.2013.2265603.

[18] D. Rueckert, "Nonrigid registration using free-form deformations: Application to breast mr images," *IEEE Trans. Med. Imaging*, vol. 18, no. 8, pp. 712–721, 1999, doi: 10.1109/42.796284.

[19] M. Tsuchiya *et al.*, "Temporal subtraction of low-dose and relatively thick-slice CT images with large deformation diffeomorphic metric mapping and adaptive voxel matching for detection of bone metastases: A STARD-compliant article," *Med. (United States)*, vol. 99, no. 12, 2020, doi: 10.1097/MD.0000000000019538.

[20] R. Sakamoto *et al.*, "Temporal subtraction of serial CT images with large deformation diffeomorphic metric mapping in the identification of bone metastases," *Radiology*, vol. 285, no. 2, pp. 629–639, Nov. 2017, doi: 10.1148/radiol.2017161942.

[21] K. Onoue *et al.*, "CT temporal subtraction improves early detection of bone metastases compared to SPECT," *Eur. Radiol.*, vol. 29, no. 10, pp. 5673–5681, Oct. 2019, doi: 10.1007/s00330-019-06107-w.

[22] I. Cruz-Matías *et al.*, "Sphericity and roundness computation for particles using the extreme vertices model," *J. Comput. Sci.*, vol. 30, pp. 28–40, Jan. 2019, doi: 10.1016/j.jocs.2018.11.005.

[23] E. R. Dougherty and R. A. Lotufo, *Hands-on Morphological Image Processing*. SPIE, 2003.

[24] T. Perciano *et al.*, "Insight into 3D micro-CT data: Exploring segmentation algorithms through performance metrics," *J. Synchrotron Radiat.*, vol. 24, no. 5, pp. 1065–1077, Sep. 2017, doi: 10.1107/S1600577517010955.

[25] H. Jin, C. Sciammarella, S. Yoshida, and L. Lamberti, Eds., *Advancement of Optical Methods in Experimental Mechanics, Volume 3*. Cham: Springer International Publishing, 2014.

[26] F. Hild *et al.*, "ON THE USE OF 3D IMAGES AND 3D DISPLACEMENT MEASUREMENTS FOR THE ANALYSIS OF DAMAGE MECHANISMS IN CONCRETE-LIKE MATERIALS ON THE USE OF 3D IMAGES AND 3D DISPLACEMENT MEASUREMENTS FOR THE ANALYSIS OF DAMAGE MECHANISMS IN CONCRETE-LIKE MATERIALS. VIII," in *International Conference on Fracture Me-chanics of Concrete and Concrete Structures*, 2013.

[27] M. R. Teague, "IMAGE ANALYSIS VIA THE GENERAL THEORY OF MOMENTS.," *J. Opt. Soc. Am.*, vol. 70, no. 8, pp. 920–930, Aug. 1980, doi: 10.1364/JOSA.70.000920.

[28] D. N. Theodorou and U. W. Suter, "Shape of Unperturbed Linear Polymers: Polypropylene," *Macromolecules*, vol. 18, no. 6, pp. 1206–1214, 1985, doi: 10.1021/ma00148a028.

[29] S. T. Erdoğan, E. J. Garboczi, and D. W. Fowler, "Shape and size of microfine aggregates: X-ray microcomputed tomography vs. laser diffraction," *Powder Technol.*, vol. 177, no. 2, pp. 53–63, Aug.

2007, doi: 10.1016/j.powtec.2007.02.016.

[30] M. Zemp, O. Y. Gnedin, N. Y. Gnedin, and A. V. Kravtsov, “On determining the shape of matter distributions,” *Astrophys. Journal, Suppl. Ser.*, vol. 197, no. 2, p. 30, Dec. 2011, doi: 10.1088/0067-0049/197/2/30.

[31] H. Goldstein, C. P. Poole, and J. L. Safko, “The Rigid Body Equations of Motion: Classical Mechanics, 3rd ed.,” *Pearson*, 2013. .

[32] M. C. Cavalli, M. Griffa, S. Bressi, M. N. Partl, G. Tebaldi, and L. D. Poulikakos, “Multiscale imaging and characterization of the effect of mixing temperature on asphalt concrete containing recycled components,” *J. Microsc.*, vol. 264, no. 1, pp. 22–33, Oct. 2016, doi: 10.1111/jmi.12412.

[33] T. Hildebrand and P. Rüegsegger, “A new method for the model-independent assessment of thickness in three-dimensional images,” *J. Microsc.*, vol. 185, no. 1, pp. 67–75, 1997, doi: 10.1046/j.1365-2818.1997.1340694.x.

[34] M. H. Protter and B. Charles Jr, *Intermediate Calculus*. 2012.

[35] A. Leemann, “Impact of different added alkalis on concrete expansion due to ASR,” in *First Book of Proceedings of the 16th international conference on Alkali-Aggregate Reaction in Concrete, (ICAAR2022)*, 2022, no. April 2021, pp. 175–184.

[36] P. M. Adler and J.-F. Thovert, “Analysis and Generation of Random Objects,” in *Fractures and Fracture Networks*, vol. 15, Dordrecht: Springer Science+Business Media, 1999, pp. 15–66.

[37] D. C. P. Peacock, C. W. Nixon, A. Rotevatn, D. J. Sanderson, and L. F. Zuluaga, “Glossary of fault and other fracture networks,” *J. Struct. Geol.*, vol. 92, pp. 12–29, Nov. 2016, doi: 10.1016/j.jsg.2016.09.008.